IS-T-705

PROTON-PROTON INTERACTIONS AT 200 AND 300 GeV/c

Fumio Ogino

Ph. D. Thesis Submitted to Iowa State University

Ames Laboratory, ERDA
Iowa State University
Ames, Iowa 50011

January 1976

PREPARED FOR THE U.S. ENERGY RESEARCH AND DEVELOPMENT ADMINISTRATION UNDER CONTRACT NO. W-7405-eng-82

DISCLAIMER

Available from: National Technical Information Service
U. S. Department of Commerce
P.O. Box 1553
Springfield, VA 22161

Price: Microfiche $2.25

Proton-proton interactions at 200 and 300 GeV/c

by

Fumio Ogino

A Dissertation Submitted to the

Graduate Faculty in Partial Fulfillment of

The Requirements for the Degree of

DOCTOR OF PHILOSOPHY

Department: Physics

Major: Elementary Particle Physics

Approved:

In Charge of Major Work

For the Major Department

For the Graduate College

Iowa State University
Ames, Iowa

1975

TABLE OF CONTENTS

Proton-proton interactions at 200 and 300 GeV/c*

Fumio Ogino

Under the supervision of William J. Kernan Jr.
From the Department of Physics
Iowa State University

The reactions $pp \to pp\pi^+\pi^-$ and $pp \to pp\pi^+\pi^-\pi^+\pi^-$ at 200 and 300 GeV/c were investigated using the Fermilab 30-inch Hydrogen Bubble Chamber and downstream Wide-Gap Spark Chambers. This analysis is based upon approximately 9500 4-pronged and 6-pronged events. The cross sections were consistent with pomeron dominance for these reactions. The final state $pp\pi^+\pi^-$ is dominated by Single Diffractive Dissociation, whose features are quite similar to those observed at low energy. A strong signal for Double Excitation was seen in the $pp\pi^+\pi^-\pi^+\pi^-$ final state and pomeron factorization was found to be satisfied. In the $pp\pi^+\pi^-$ final state, 66 events passed the criterion of Double Pomeron Exchange defined by D. M. Chew However, these events were found to be severely contaminated by diffractive events. The two particle exclusive azimuthal correlations agreed well with the prediction of a photo-statistical model.

---

*USERDA Report IS-T-705. This work was performed under Contract W-7405-eng-82 with the Energy Research and Development Administration.

I. INTRODUCTION

In recent years, there have been numerous studies on the multiparticle production processes, which play a dominant role in high energy particle collisions. The availability of the very high energies for these studies is a consequence of the completion of two giant particle accelerators: the proton synchrotron at the Fermi National Accelerator Laboratory, U.S.A. and the Intersecting Storage Rings (ISR) at CERN, the European Organization for Nuclear Research. Experiments on multiparticle reactions at these machine energies are difficult; not only is an enormous number of particles involved, but also both the facilities and experiments are expensive. Yet, it is hoped that, with the help of advanced experimental techniques and theoretical ideas, one can now probe hitherto unstudied regions of the strong interactions: a force that is responsible for holding the nucleus together and for which the appropriate distances and times are less than 10^{-13} cm and 10^{-23} seconds.

The main topic of this dissertation is a study of the proton-proton multiparticle exclusive reactions:

$$pp \rightarrow pp\ \pi^+\pi^- \tag{1-1}$$

and

$$pp \rightarrow pp\ \pi^+\pi^-\pi^+\pi^- \tag{1-2}$$

at incident proton beam momenta of 200 and 300 GeV/c. Of course, the multiparticle reactions are closely related to the elastic scattering, which has been studied extensively for different beams from the lowest energy to the highest available energy by many authors (1,2). Thus the comparable work on pp elastic scattering at 200 and 300 GeV/c has also been included in this thesis.

The present analysis is based on data taken in an experiment performed at the Fermi National Accelerator Laboratory using the 30-inch Hydrogen Bubble Chamber and downstream Wide-Gap optical spark chambers.[1] The preliminary results were presented at an American Physical Society Meeting (3).

The bubble chamber and spark chamber have been two independent detectors in High Energy Physics research during the past two decades. The bubble chamber is excellent for measuring the interaction vertex and the variables of slow tracks (less than 5 GeV/c) at fairly large angles. However, this detector is a poor instrument for the measurement of high momentum forward tracks. The spark chambers can detect these forward tracks, but are insensitive to the interaction vertex. In this experiment, these two detectors were

---

[1]Collaboration by Argonne National Laboratory, Fermi National Accelerator Laboratory, Iowa State University, Michigan State University and University of Maryland.

combined to improve the experimental resolution for multi-particle processes. Other aspects of the present experiment are reported elsewhere (4,5).

Reactions (1-1) and (1-2) have been thoroughly studied up to 28.5 GeV/c. There are only two reports for reaction (1-1) above 28.5 GeV/c; a bare bubble chamber experiment by a French-USSR collaboration at 69 GeV/c (6) and a bare bubble chamber experiment by the Argonne National Laboratory group at 200 GeV/c (7). Our analyses of reaction (1-1) at 300 GeV/c and of reaction (1-2) at both 200 and 300 GeV/c are the first data on these reactions in this high energy region.

There are many ways to present the data. The rapidity (the definition is given on page 108), for example, is thought to be one of the important kinematic variables, and the study of the details of the reaction as a function of this variable is a major tool in understanding these processes. The higher the energy of the incident proton beam, the larger is the rapidity difference available between the target fragmentation region and the beam fragmentation region. Thus, it becomes easy to separate the two regions and to study the properties of pomeron exchange, which is believed to be responsible for diffractive effects. However, because of limited statistics, neither earlier report, either at 69 GeV/c or at 200 GeV/c, has been conclusive about the details of production mechanisms for reaction (1-1).

There are three distinct ways that the available data from the present experiment can be treated. These are:

1. As a bare bubble chamber experiment.

2. As a bare bubble chamber experiment, but using the downstream information to give a better estimate of the background.

3. For the highest precision in each event, use only the "hooked-up" events between the bubble chamber and spark chamber.

Due to the spark chamber trigger efficiency (about 40%) and due to the low percentage of four constraint events[2] in the entire data sample, our present statistics are somewhat insufficient if method 3 alone is used for the analysis of the exclusive reactions (1-1) and (1-2). Therefore, methods 1 and 2 have been used throughout this analysis in an attempt to provide the maximum information in the most useful fashion. Chapters II through IV of this dissertation describe the details of the experiment; in particular, attention is paid to the effect of improved resolution on the analysis of the exclusive channels.

In chapter V, the experimental results are presented. The proton-proton elastic scattering at 200 and 300 GeV/c has been carefully studied to establish a self-consistent method

---

[2] '4C' for the phrase 'four-constraint' is frequently used in this dissertation.

to obtain the cross sections of the multiparticle exclusive channels. Then the characteristic features of reactions (1-1) and (1-2) are presented. The idea of pomeron exchange is examined from four aspects:

a. The energy dependence of the cross sections.

b. The study of Single Diffractive Dissociation

c. The search for Double Excitation: $pp \rightarrow N^{*}N^{*}$ and the test of pomeron factorization.

d. The search for double pomeron exchange processes.

The exclusive two particle azimuthal correlations are also discussed in chapter V. Chapter VI summarizes these investigations.

II. EXPERIMENTAL TECHNIQUES

This analysis is a study of the proton-proton exclusive reactions at 200 and 300 GeV/c using the 30-inch Hydrogen Bubble Chamber (BC)[3] and downstream wide-gap spark chambers[3] (SC) at the Fermi National Accelerator Laboratory. In this chapter, the experimental details; in particular, beam, Hybrid System and Film Measuring Systems are described.

A. Beam

The primary proton beam is first extracted from the 2-km diameter main-ring of the Fermi National Accelerator Laboratory (Fermilab). It is transported to the target area, which is located about 1 km downstream from the extraction area. The intensity of the primary proton beam at extraction is approximately 10^{13} protons/pulse. Secondary protons, produced in interactions with targets in the primary proton beam line, are further transported through Hadron Beam Line N-3 for another 1.5 km to the 30-inch Hydrogen Bubble Chamber in the neutrino area. As the secondary protons pass through the slits, magnets, collimators and monitoring counters; the beam momentum is selected and the beam intensity is also reduced. During the course of the present experiment, multiple beam spills up to four pulses per one

---

[3]The abbreviations 'BC' and 'SC' are used throughout this dissertation.

accelerator machine cycle were made; the spills were separated in time by approximately 250 msec. Some of the important components in the N-3 beam line are:

a. Fast Flux limiting Beam Kicker, located approximately halfway between the hadron target and the 30-inch HBC.

b. A Cerenkov counter, downstream of the kicker.

The kicker minimizes the fluctuation of the beam tracks and adjusts the center of the intensity distribution of the beam at the desired value, for example, 7 protons/pulse. The Cerenkov counter provides information on the particle type. This is useful for beam purity studies; however it is not essential for the present proton experiment. The beam is monitored by several counters: the wire proportional chambers, scintillation paddle counters and the finger counters for the wide-gap chambers as well. These counters are useful in monitoring and controlling the distributions of the beam particles in the horizontal and vertical planes at the BC window. They are also used to veto taking a picture for a bad beam spill. For this experiment, the lower and upper bounds of beam tracks were set at 2 and 13 respectively. For a beam spill outside this range, the BC did not take a picture. It should be noted that these counters are not reliable for absolute counting of beam tracks.

B. Hybrid System

The unique feature of the hybrid system has already been briefly described in chapter I. The details of the system are reported elsewhere (8). We shall mention here only the essential features that are required for the discussion of this dissertation. Figure 2.1 shows a part of the wide-gap spark chamber system; each gap of the dual SC is 20 cm; the active area is 75 (horizontal) x 100 (vertical) cm; each of the four chambers has a set of mirrors for stereo views. The distance from the center of the BC to the most upstream chamber is about 4 m and to the 4th chamber it is about 7 m. The spark chambers are pressurized by gas (Ne-He mixture) and the entire spark chamber system is enclosed in an air-pressurized room. This enclosure is necessary both to provide the dark background for photography and also as an isolation room because of the safety problems with hydrogen leaks from BC. As shown in Figure 2.2, the trigger system consists of beam deflection counters, $\frac{dE}{dX}$ counters and associated fast logic circuits, which are gated to count for 4 msec during the beam spill. The SC are triggered when the electronic logic indicates either or both of the following cases:

a. Multiparticle production defined by upstream beam deflection counters and $\frac{dE}{dX}$ counters behind the BC.

b. Beam deflection trigger: a single particle is

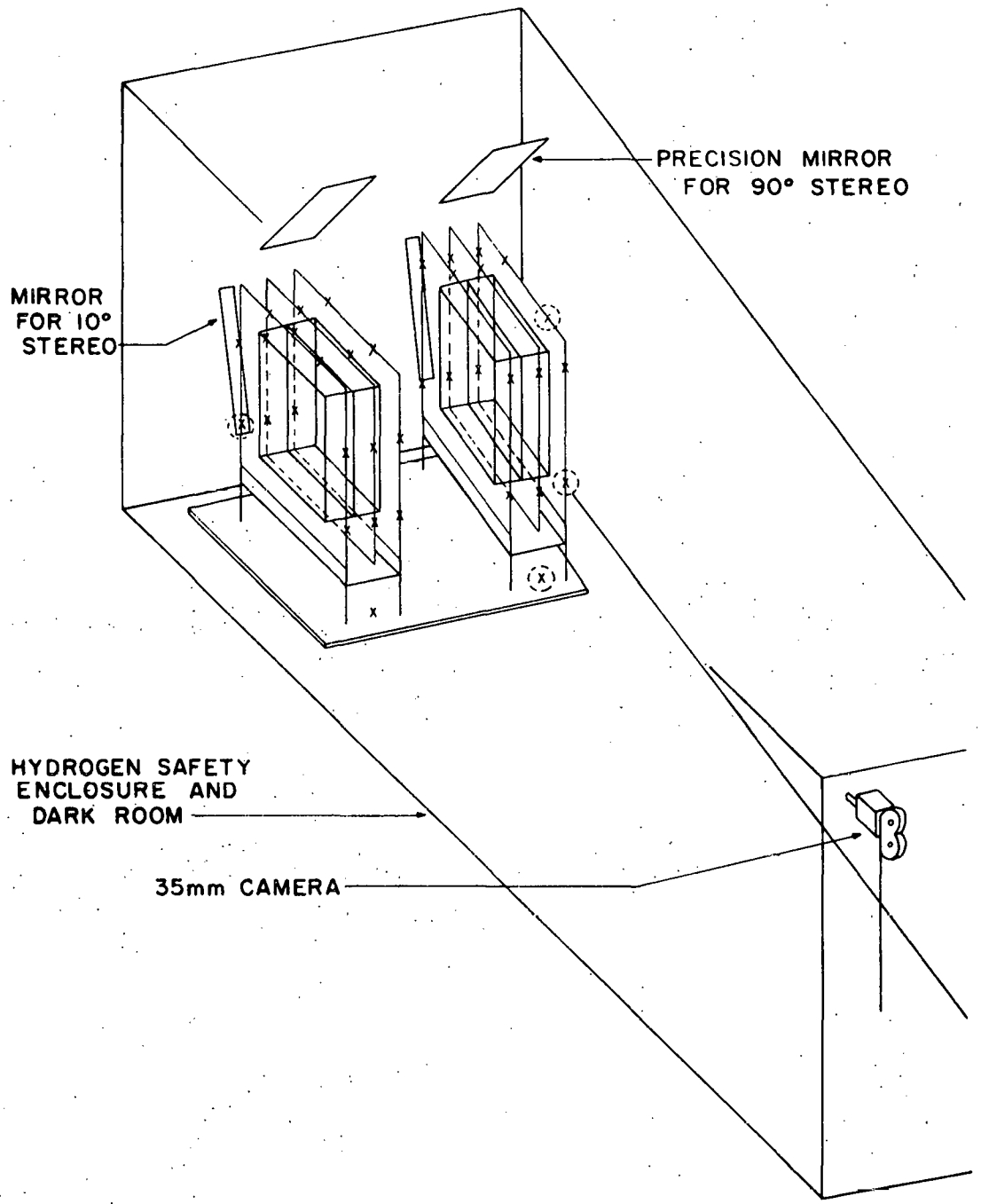

Figure 2.1. Wide-gap optical spark chamber (one of two such chambers). Beam enters from the left.

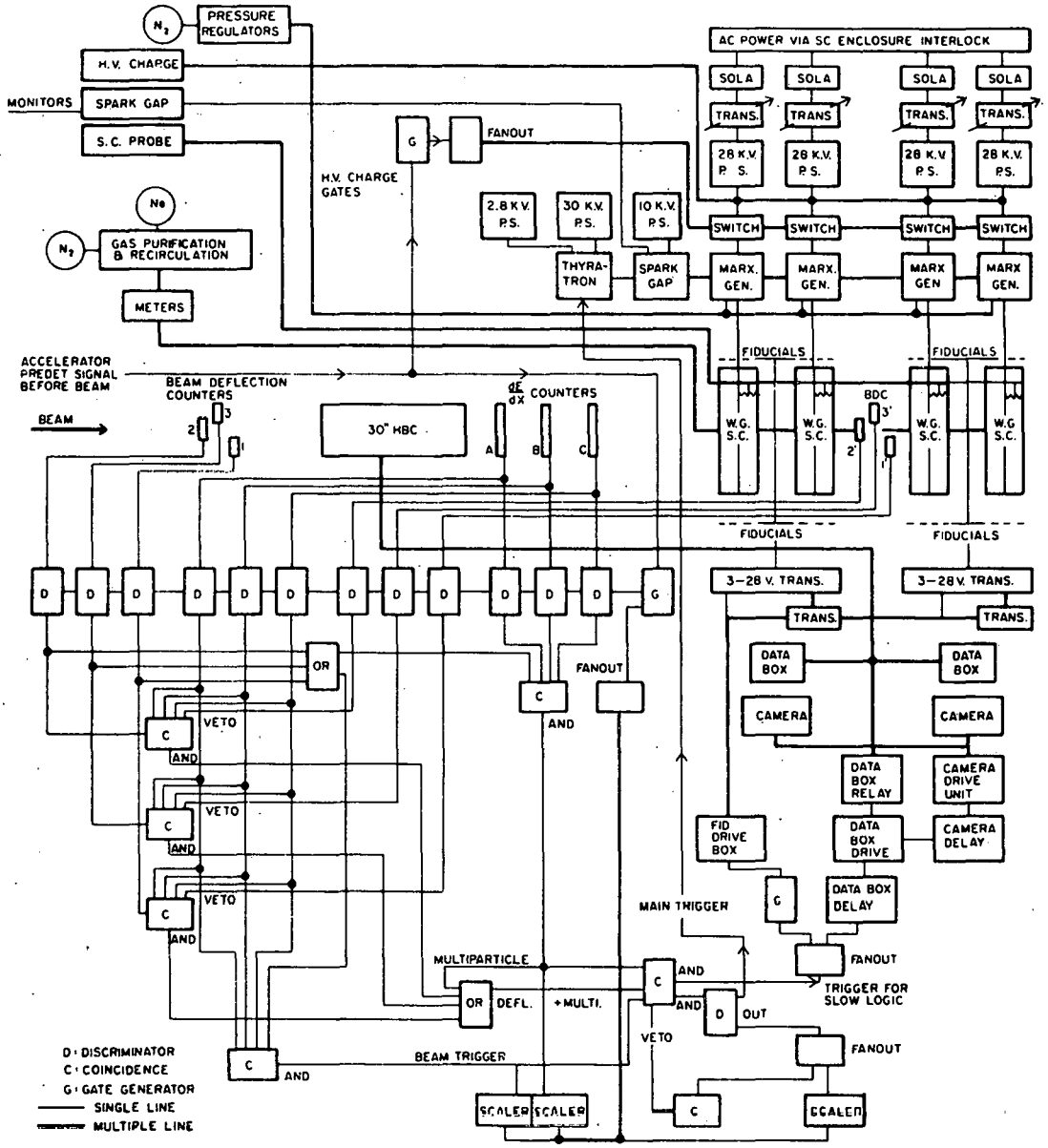

Figure 2.2. Block diagram of Experiment 2B hybrid system.

detected by the $\frac{dE}{dX}$ counters, but missed by the downstream B.D. counter which is aligned with the upstream B.D. counter that detected the beam particle.

As shown in Figure 2.2, the main trigger to the THYRATRON fires the spark gap, which subsequently triggers the 10-stage Marx generators. The Marx generators were already charged up in preparation for the beam. Each Marx generator supplies a high voltage pulse of 280 kV with a width of 60 nanoseconds to the central plate of the SC. Then sparks are generated along the ion trails of trajectories of particles which traversed the SC. The tracks and the images from mirrors are photographed by two 35-mm cameras: one camera for the upstream and another for the downstream pair of dual wide-gap chambers. Each camera has two lenses: one for the direct and the 10 degree mirror view and another lens which views the 90 degree mirror. Thus three different views for the tracks associated with the same event as seen in two spark chamber modules are recorded on the same picture frame. The 2 SC pictures and 3 BC pictures constitute the complete set of pictures for one event. The quality of tracks is controlled primarily by the termination resistors on the SC and by the power supply voltage for the Marx generators. While the main trigger pulse fires the spark chamber, the delayed trigger pulse turns on the fiducial lights for the SC frames and then the data boxes are lighted to record

additional indicative information on film. The cameras are then advanced by one frame, which takes about 100 msec. The entire process is completed within 250 msec and the system is ready for the next beam spill.

Another important feature of the system (not shown in Fig. 2.2) is the capability to record data for two triggers in one beam spill. Spark chambers 1, 3 and 4 are fired on the 1st trigger. Then SC #2 is triggered for the second event in the BC.

C. Scanning of Bubble Chamber Film

As was anticipated, the scanning of the BC film was rather difficult. This difficulty is associated with the large number of tracks produced in a narrow forward cone in interactions at these high energies. The typical BC picture is shown in Figure 2.3. The scanners were instructed to search for all types of interactions on the film and record the following information for each event:

a. Digitized scan codes which indicate the type of event as well as the estimate of measurement difficulty for the event.

b. The number of beam tracks entering the chamber between the proper fiducials for every 10th frame. Special attention is requested for overlapping events.

c. For each event that is measurable or worth trying, an approximate vertex location, the number of neutral particle decays and comments about the association of such decays with the primary vertex, neutron stars, the number of Dalitz pairs and comments about track identification at the primary vertex, for example, every slow proton is flagged. All frames were scanned twice: the scanning efficiency for finding the event was better than 95%. Tables 2.1 and 2.2 show the topological cross sections based on the results from our scan. The cross sections are, however, normalized to the total cross sections as determined in previous reports from bare BC experiments by the ANL group at 200 GeV/c and by the CALTECH group at 300 GeV/c.

D. Scanning of Spark Chamber Film

A typical spark chamber picture is shown in Figure 2.4. The scanners were requested to record the following data for a SC frame:

a. Trigger Code: As explained in section B, the system can trigger chamber #1, #3, and #4 for the first event in the BC and then trigger chamber #2 for a second event during one beam spill. This is referred to as an "alternating trigger". If there are two events on one frame, they are recorded separately on the scan sheet with the same frame # and different trigger code. Sometimes the

Figure 2.3. A 6-pronged proton-proton interaction at 300 GeV/c, as seen in bubble chamber.

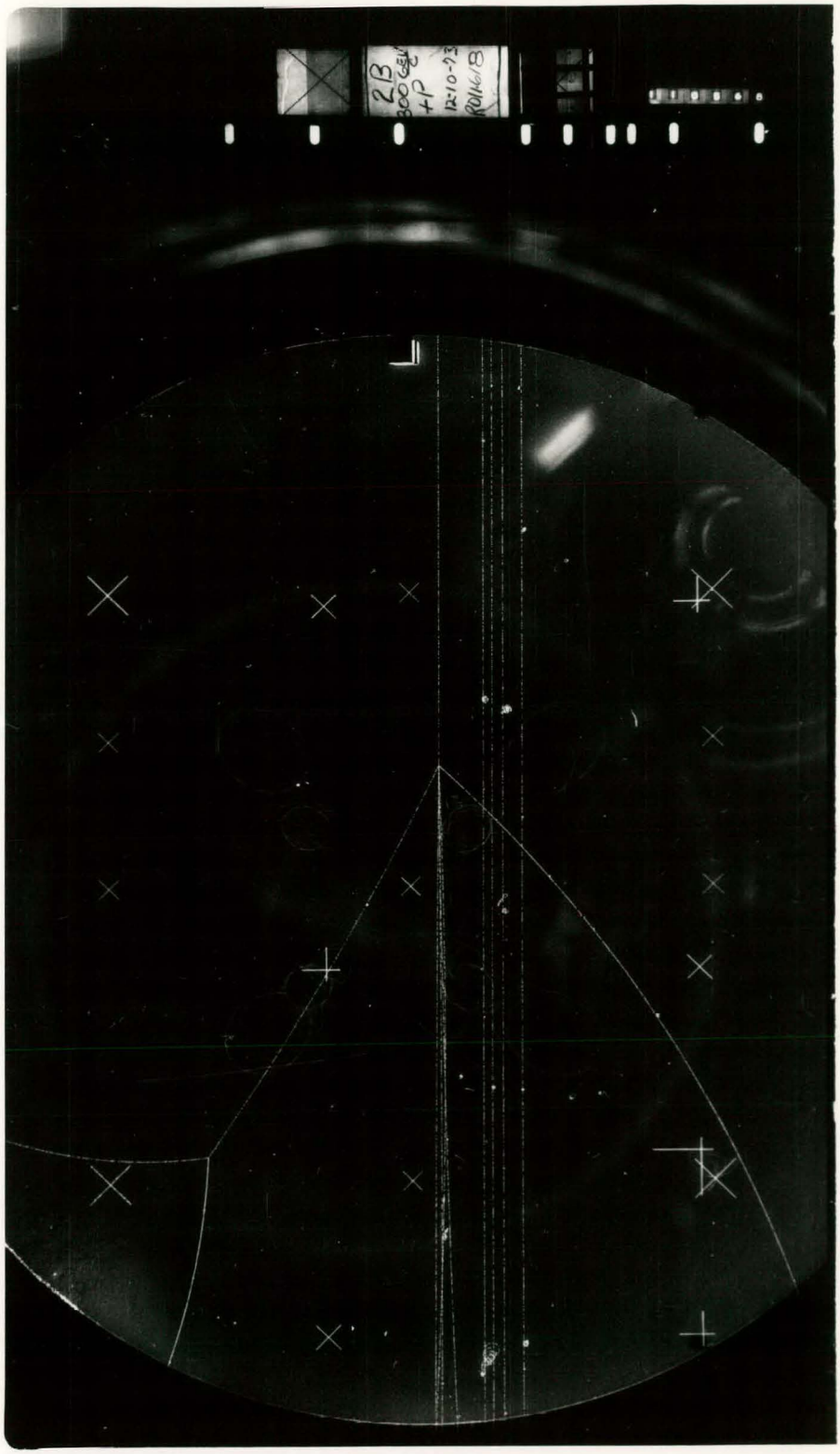

Figure 2.4. The spark chamber photograph which is associated with the 6-pronged event in the BC which was shown in Figure 2.3. The spark chamber tracks from three different views are recorded on the same frame; from the right direct views and 10 degree views in SC #1 and SC #2, and indirect views of SC #1 and SC #2. The SC frame number is always larger than the corresponding BC frame number by one in the present experiment.

THIS PAGE
WAS INTENTIONALLY
LEFT BLANK

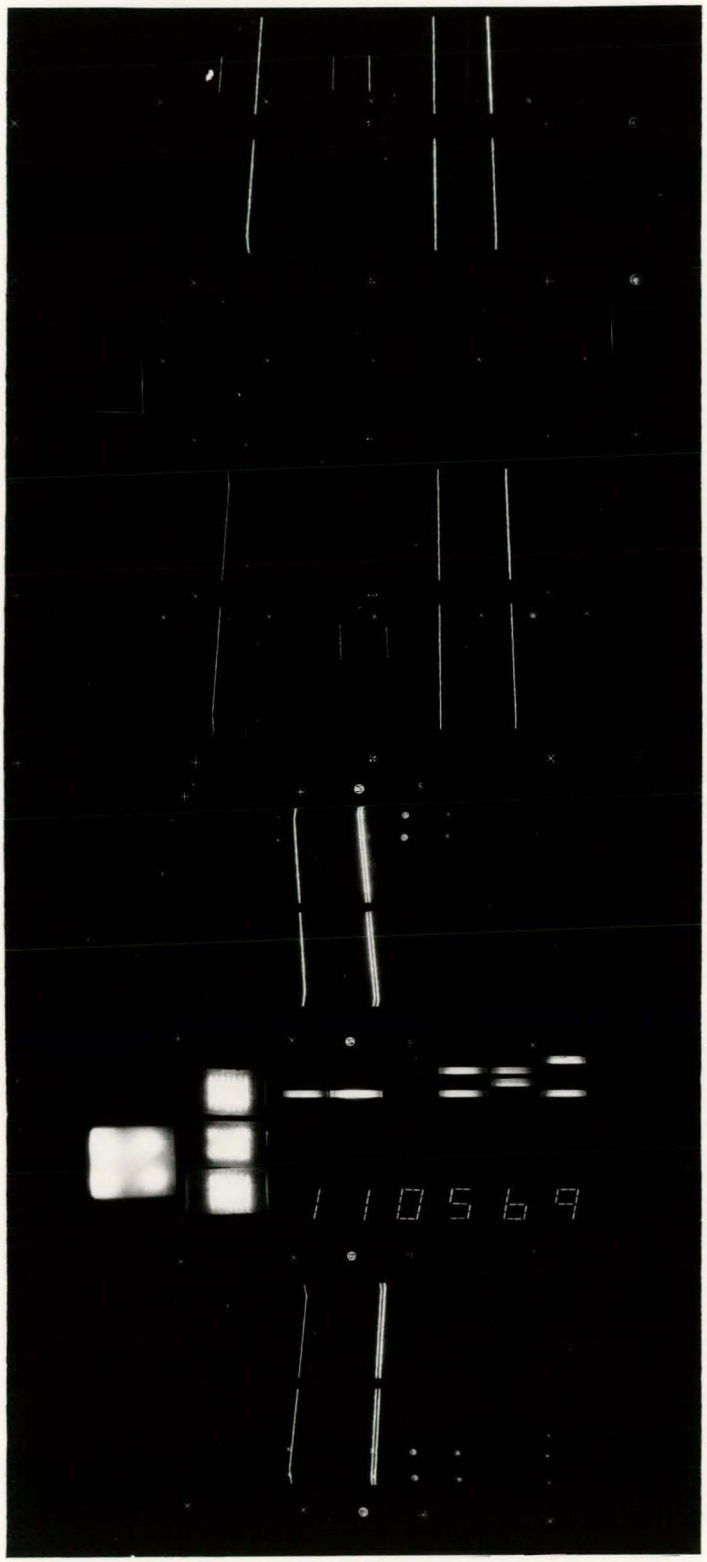
110569

trigger system is changed so that all 4 chambers are fired on the same event in the bubble chamber, which is called a "nonalternating trigger".

b. Tracks: Each of the 4 chambers has 2 gaps. The number of tracks is counted in each gap. The maximum number of tracks seen in either the direct view or the indirect view is the number of tracks in the chamber.

c. Gamma Showers and Hadron Showers: SC #4 is used to detect the number of showers produced in a lead plate inserted between chamber #3 and chamber #4. All frames are scanned twice, but no attempt was made to estimate the scanning efficiency. Where the tagging information from the wire-chamber and trigger counters is available, only those tagged events are measured.

E. Measuring and Data Sorting

The pictures from the present experiment are different from previous experiments at Iowa State in that many tracks are involved in BC pictures and also there are 10 views which need to be measured for SC pictures. Thus it is vitally necessary to maximize measuring efficiency. At Iowa State, the measurements have been done by PDP 11/50 (previously EMR 6050) controlled semi-automatic measuring machines; the details of which are described in Reference 9. The modification of the system for the present experiment is described in this section.

In order to overcome the difficulty in measuring this film, larger lenses were installed on the measuring machines. Accordingly, a calibration was done for each measuring machine. One of the machines was chosen as a reference and all the fiducial measurements for the determination of optics constants were done on this machine. The BC has 22 fiducials on the glass windows. Both upstream and downstream SC have at least 34 visible fiducials in the direct view and 12 visible fiducials in the indirect view. Using an average of 18 measurements for each fiducial and the survey data on the fiducial positions, the optics constants for the BC and SC were determined by the standard program CAMADJUST. The spark chamber point scatter (FRMS) in space are about 100 μm in direct views and about 400 μm in 90-degree views. These optics constants were also used by the on-line programs to check the quality of track measurement. In the actual measurement of events, 4 fiducials are measured in each view of the BC pictures. Among 10 views in SC film, six of them are optically unique, since ten degree views and the direct view are photographed on the same picture frame. Four fiducials are also measured in each of six views.

The ISU version of FIDO,[4] which is a fiducial transformation program, then redetermined the magnification factor for each event. As a result, all the measured data are normalized to the reference measuring machine.

If the on-line program finds that the fiducial measurement is poor, the measurer is asked to remeasure the fiducials. As soon as the fiducial measurement succeeds, the vertex and track measurements follow. In the case of BC film, the on-line geometry program, HGEOM, reconstructs the track immediately after the measurement. The measurer is requested to redo the measurement if the track RMS on the film plane is larger than 15 μm. The request is displayed on the viewing

---

[4] ISU version of FIDO was written by H. B. Crawley and it has been used widely by Experiment-2B collaborators. The main idea is introduced below. The measured fiducial positions X and Y are transformed according to

$$X' = AX + BY + C, \qquad Y' = -BX + AY + D \tag{2-1}$$

where the magnification is included in the parameters A, B, C and D. We want to minimize the chi-square, which is defined as

$$\chi^2 = \sum_i (X'_i - X_i^R)^2 + (Y'_i - Y_i^R)^2 \tag{2-2}$$

where X_i^R and Y_i^R are the locations of the reference fiducials. Differentiating equations (2-2) by the 4 parameters in (2-1), we have 4 equations

$$\frac{\partial \chi^2}{\partial A} = 0, \quad \frac{\partial \chi^2}{\partial B} = 0, \quad \frac{\partial \chi^2}{\partial C} = 0, \quad \frac{\partial \chi^2}{\partial D} = 0.$$

Solving these equations simultaneously, we obtain 4 transformation parameters for each event.

screen of a display terminal. For a SC film, only a straight line fit is performed, since these detectors are not in a magnetic field. It is found that HGEOM reconstruction is consistent with the results of the off-line reconstruction program TVGP. In fact, the vertex information from HGEOM was used in conjunction with the tagging information of the wire-proportional chamber and with the trigger counters to select useful SC pictures.

The magnetic field used in the on-line program was checked by two methods:

a. TVGP reconstruction of beam tracks which traversed the entire chamber.

b. The reconstruction of Vee events, particularly K° meson candidates both by TVGP and HGEOM.

It was found that the beam momentum distribution has a peak at 300 GeV/c with a broad width in the higher momentum data. Although the statistics of events are very limited, it was also seen that the Missing Mass distribution for K° meson candidates has a peak at the correct value (497.7 MeV).

Since both BC and SC film measurements proceed simultaneously on different measuring machines under computer control, the data tape contains the variable length BC track records as well as variable length SC records in an arbitrary order. In addition, the BC tracks, either positive or negatime, are arranged randomly within a record, which HGEOM can

read, but TVGP cannot accept. TVGP requires the negative tracks first. However, the sagitta of many tracks is so small at this high energy that it is difficult to be certain of the sign of the curvature. For example, a beam proton of 300 GeV/c in the magnetic field of 25 kG is deflected by approximately 1.60 mrad. vertically while it travels through 63.5 cm (effective BC length). In terms of vertical displacement, this corresponds to only 1 mm! Considering the fact that the BC position resolution is approximately 100 μm and that the tracks are not always as long as a beam track, one can easily imagine that large momentum measurement errors are associated with the analysis of the bare bubble chamber. The polarity of each track is determined, at Iowa State, according to the following procedure. For each track, 3 measured points A, B and C are chosen in each of 3 views to define the vector product $\vec{X} \times \vec{Y}$, where the two vectors are those which connect the points A and B, and B and C respectively. Obviously, the direction of the vector product depends on the sign of the charge. The determination of the sign of the charge first requires that all such vectors in the three different views be in the same direction. However, the solution that was obtained this way sometimes does not satisfy charge conservation for the event as a whole, due to wrong curvature determination in some views. If this happens, the constraints are reduced from 3 views to 2 views to get the

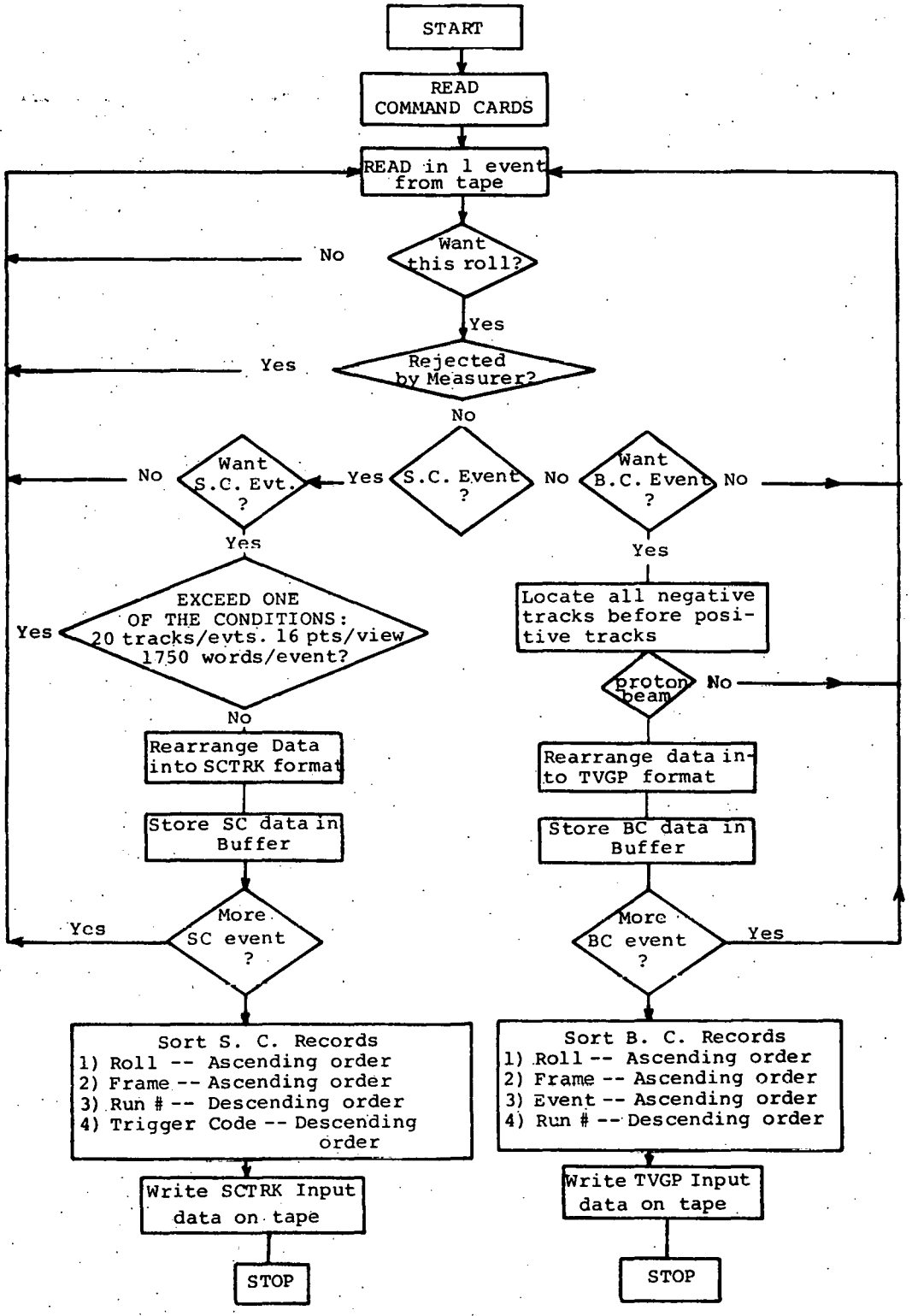

Figure 2.5. Data preparation flow chart.

best possible solution. For later HOOKUP processing, it is also important to have BC and SC frame numbers in a specific order. All the above mentioned procedures for data preparation are summarized in Figure 2.5.

Table 2.1. Partial cross sections 200 GeV pp.
Estimates by W. J. Kernan (all σ in mb).

Top	Exp-2B	PRD 9, 2689(74) ANL(2)	PRL 29, 515(72) ANL(1)
2 pr.	10.00 ± 0.44	9.77 ± 0.40	10.3 ± 0.9
4	6.04 ± 0.30	5.91 ± 0.28	5.55 ± 0.28
6	6.60 ± 0.31	6.89 ± 0.32	6.94 ± 0.31
8	5.78 ± 0.28	5.73 ± 0.28	5.78 ± 0.28
10	4.67 ± 0.25	4.56 ± 0.24	4.41 ± 0.25
12	3.07 ± 0.18	3.23 ± 0.18	3.43 ± 0.22
14	1.65 ± 0.13	1.58 ± 0.11	1.70 ± 0.16
16	0.75 ± 0.11	0.85 ± 0.08	0.87 ± 0.11
18	0.35 ± 0.05	0.34 ± 0.04	0.30 ± 0.07
20	0.11 ± 0.03	0.12 ± 0.03	0.17 ± 0.05
22	0.05 ± 0.02	0.05 ± 0.02	0.05 ± 0.03
24	0.01 ± 0.01	0.012 ± 0.008	-
26	0.01 ± 0.01	0.004 ± 0.004	-
		Total 39.0 ± 1.0	Total 39.5 ± 1.1
		(Used to normalize 2B.)	

Table 2.2. Partial cross sections 300 GeV pp.
Estimates by W. J. Kernan (all σ in mb).

Top	Exp-2B	PRD 10, 2080(1974) Cal Tech et al.
2 pr.	9.91 ± 0.15	10.49 ± 0.27
4	5.43 ± 0.06	5.08 ± 0.19
6	5.72 ± 0.05	5.84 ± 0.20
8	6.06 ± 0.06	5.86 ± 0.20
10	5.39 ± 0.08	5.09 ± 0.19
12	3.43 ± 0.06	3.67 ± 0.17
14	2.41 ± 0.06	2.54 ± 0.15
16	1.20 ± 0.02	1.13 ± 0.12
18	0.67 ± 0.02	0.66 ± 0.07
20	0.26 ± 0.02	0.26 ± 0.05
22	0.12 ± 0.02	0.18 ± 0.04
24	0.04 ± 0.02	0.043 ± 0.026
26	0.0001 ± 0.0001	0.035 ± 0.020
28	0.0001 ± 0.0001	-
		Total 40.68 ± 0.55
		(Used to normalize 2B data.)

III. GEOMETRIC RECONSTRUCTION AND HOOKUP

A detailed study of the background in the exclusive channels using the high-quality HOOKUP data is one of the unique aspects of the present experiment. In addition, it is useful to present the results of our studies in making the HOOKUP program itself work and the results of studies related to the resulting resolution, both for our own records and also as an aid to other groups working on the same or similar programs. Thus, the details of BC and SC track reconstruction and HOOKUP methods used at Iowa State are presented in this chapter.

A. Bubble Chamber Track Reconstruction

For BC track reconstruction, HGEOM had been used at Iowa State; however TVGP[5] (Three View Geometry Program) was adopted as an off-line BC track reconstruction program for the present experiment. Depending on the data taking period, the constants used with TVGP are different. In Table 3.1, two of the primary sets of constants: (a) BC magnetic field constants and (b) optics constants, are summarized.

---

[5] TVGP adopted for IBM 360/70 at Iowa State is a modified version of MSU TVGP for CDC 3600. The prime reference to TVGP is still UCLRL Programming Note, p-117 written by F. T. Solmitz, A. D. Johnson and T. B. Day, 1965 (10).

Table 3.1. TVGP constants.

B.C. Magnet Constants

Rolls	AMPS	SHUNT (mV)	Kilogauss
Not used at ISU	18	45	29.8
500 - 800	16	40	26.9
> 800	14.7	36.75	25.0

Optics Constants

Set	Roll[a]	Roll Group	Data Taking Period
1	505	500 - 599	Before Nov. 1973
2	603	600 - 800	11/8/73 - 12/10/73
3	812	801 - 1019	3/17/74 - 4/17/74
4	1025	> 1024	After 4/17/74

[a]Roll that was used to determine the constants for Roll Groups indicated.

The setting error used in TVGP is 5 μm which is consistent with the RMS distribution of the residuals from measured tracks. No floor was used for the measurement error of tracks.

B. Spark Chamber Track Reconstruction

First of all, the idea of SC track reconstruction by the program SCTRK[6] is briefly described. The tracks in the SC are photographed through two lenses: one for the direct and for the 10 degree view and another lens for the indirect view. Since there is no magnetic field inside the SC enclosure, SC tracks are always straight lines. The

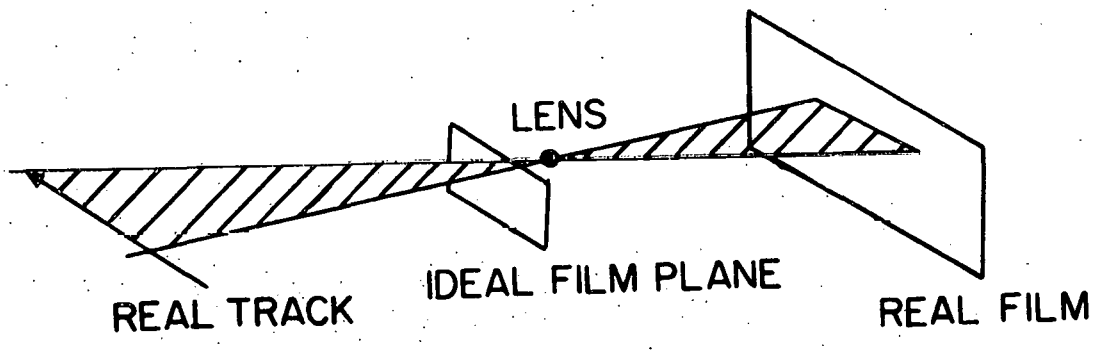

Figure 3.1. SC track reconstruction.

[6]The program SCTRK was written by B. Y. Oh at Michigan State University (1973).

straight line on the film and the lens form a plane (Figure 3.1). Since there are two lenses, two planes can be constructed. The intersection of these two planes is the track location in real space. Incidentally, the ideal film plane, which is a virtual reference plane shown in Figure 3.1 is used in actual track reconstruction. The measured points are projected onto this plane. There are usually more than one SC track seen in each of the SC views. Thus one needs to find the right pair of tracks in the direct and the indirect views. The next step is to calculate the position of the track image on the 10 degree mirror (Figure 2.1) using the information from the direct and indirect views. This prediction is compared with the actual 10 degree view tracks in order to resolve ambiguities among the solutions. It is therefore, important to determine the location of the 10 degree mirror precisely. This determination was done using measured beam tracks.

A schematic drawing of the four chambers and the coordinate system is shown in Figure 3.2.

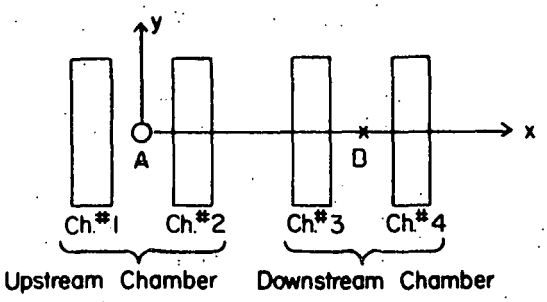

Figure 3.2. SC coordinate systems.

Track reconstruction in the SC begins by using an individual SC coordinate system. The results of reconstruction in each spark chamber are then transformed to the overall SC coordinate system according to the formula,

$$X' = X + AIJ\ (1,ITRIO)$$

$$Y' = Y + AIJ\ (2,ITRIO)$$

$$Z' = Z + AIJ\ (3,ITRIO)$$

$$\phi' = \phi + AIJ\ (4,ITRIO)$$

$$\theta' = \theta + AIJ\ (5,ITRIO) \qquad (3\text{-}1)$$

where AIJ(5,4) are module transformation parameters and ITRIO is an index indicating one of the four spark chambers.

The program SCTRK is written such that the initial results of reconstruction are given at two fixed X positions: At A for Chamber #1 and Chamber #2, and at B for Chamber #3 and Chamber #4 in Figure 3.2. Then the reconstructed positions are transformed to the overall spark chamber coordinate system: this is chosen to be the same as the Chamber #1 coordinate system whose origin is at A. Therefore AIJ parameters for Chamber #1 are all zero and AIJ (1,2) is always zero too. When more than two spark chambers are used for one event, the average of the transformed values is calculated and then the FRMS for track matching on the film plane is computed. The two chambers

in the upstream module (or in the downstream module) are not quite optically independent of each other. This is becuase the tracks in the direct view and in the 10° view for both Chamber #1 and Chamber #2 are recorded on the same film plane. This means, in terms of transformation parameters, that nonzero values for those parameters related to y and the azimuthal angle in a module transformation should not be allowed. To be more specific the transformation Chamber #2 → Chamber #1 should be:

$$
\begin{aligned}
X' &= X \\
Y' &= Y \\
Z' &= Z + AIJ\ (3,2) \\
\phi' &= \phi \\
\theta' &= \theta + AIJ\ (5,2).
\end{aligned}
\tag{3-2}
$$

On the other hand, the upstream two chambers are optically independent of the downstream two chambers. Therefore we are free to use all five AIJ parameters in a transformation from Chamber #3 coordinate system to the spark chamber coordinate system.

Using the beam tracks from Rolls 820 and 821 and assuming that there are no correlations among parameters, the AIJ parameters were determined (Table 3.2). Only the events in which all spark chambers successfully fired were used. This restriction makes it easy to find the AIJ

parameters. The expectation is that the distributions of reconstructed positions and angles from different spark chamber combinations are transformed, with appropriate AIJ parameters, to the similar distributions as those calculated from the reconstruction using only chamber #1. Table 3.2 shows the ISU parameters that result from these studies in matching up tracks. Table 3.3 shows the result of the beam track reconstruction using different spark chamber combinations. It is also possible to let the program determine the relative location of the spark chambers using the optics constants, instead of using the AIJ parameters. Such an attempt was made, but no significant improvement was observed. In order to present the performance of ISU SCTRK, the track RMS distribution for Roll 603 is shown in Figure 3.3.

Table 3.2. AIJ parameters.

	ISU Value				
Ch. #	X (cm)	Y (cm)	Z (cm)	ϕ (rad.)	θ (rad.)
1	0.0	0.0	0.0	0.0	0.0
2	0.0	0.0	0.40	0.000	-0.0195
3	229.6	0.0	-13.5	0.0008	0.0020
4	Not determined				

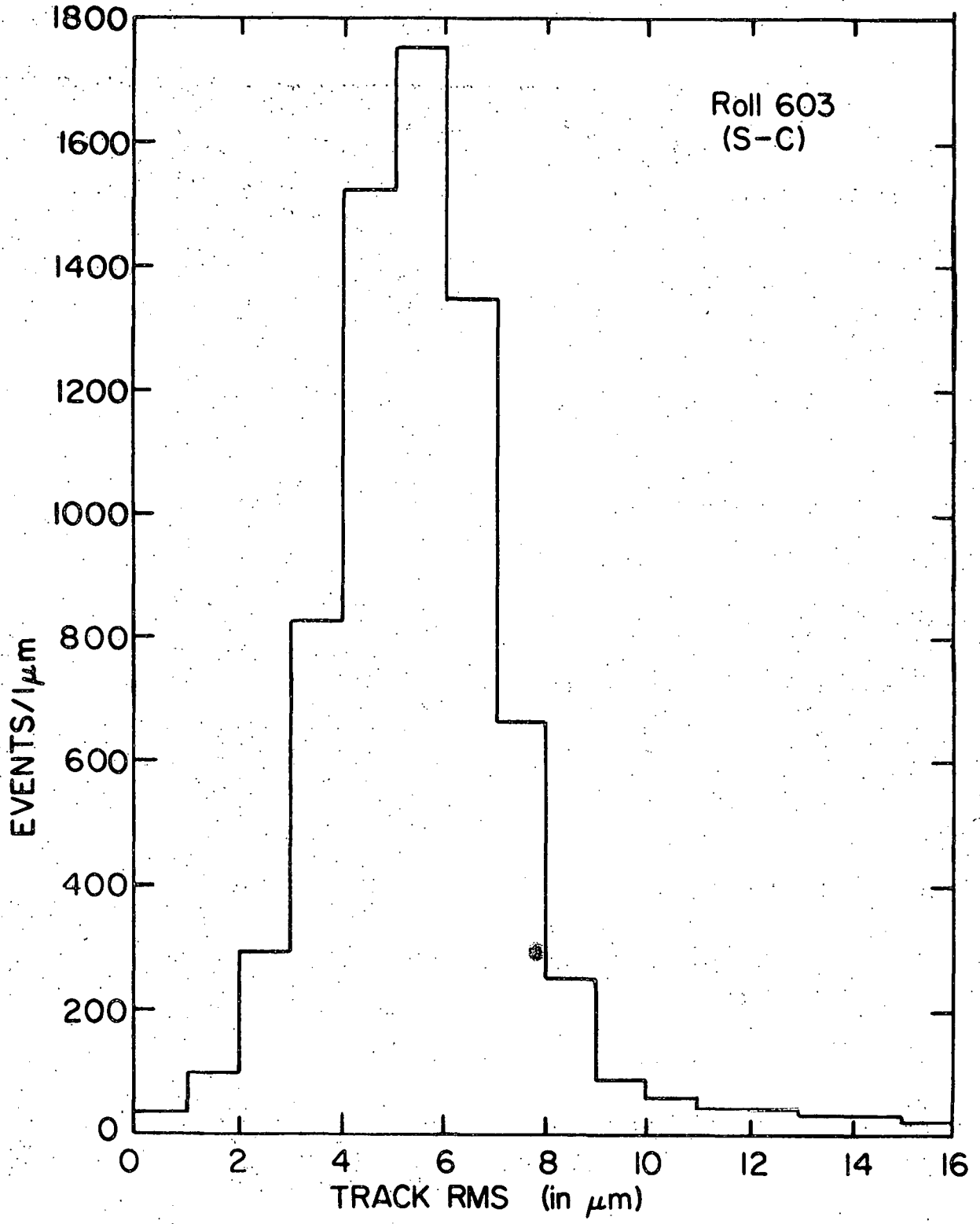

Figure 3.3. RMS errors of SC tracks on the film plane.

Table 3.3. Beam track reconstruction using different chambers.

Chamber Used	Z (cm)	TH (rad.)	Y (cm)	PH (rad.)	FRMS (μ)
1	-98.3	0.0023	17.5	0.0125	-
1-2	-98.3	0.0038	17.5	0.0121	7
1-3	-98.3	0.0023	17.5	0.0125	6

The point to be emphasized here is that this data is dominated by tracks matched up in chambers 1 and 3 and the peak of the distribution corresponds to an RMS value between 5 and 6 μm on the film.

C. Performance of HOOKUP[7]

Figure 3.4 shows the primary coordinate systems that are used in track matching. The direction of the z axis is chosen to point in the same direction as the camera in the TVGP or SCTRK coordinate system; both the TVGP and the HOOKUP coordinate systems share the origin at the center of the BC back glass window; however, they have different directions for the axes. The HOOKUP program reads TVGP and SCTRK records and then does the following two transformations.

[7] HOOKUP for the present experiment is a modified version of SLAC HOOKUP written by D. Negra and J. T. Carroll (11). Major modifications were made at Iowa State, Michigan State and University of Notre Dame.

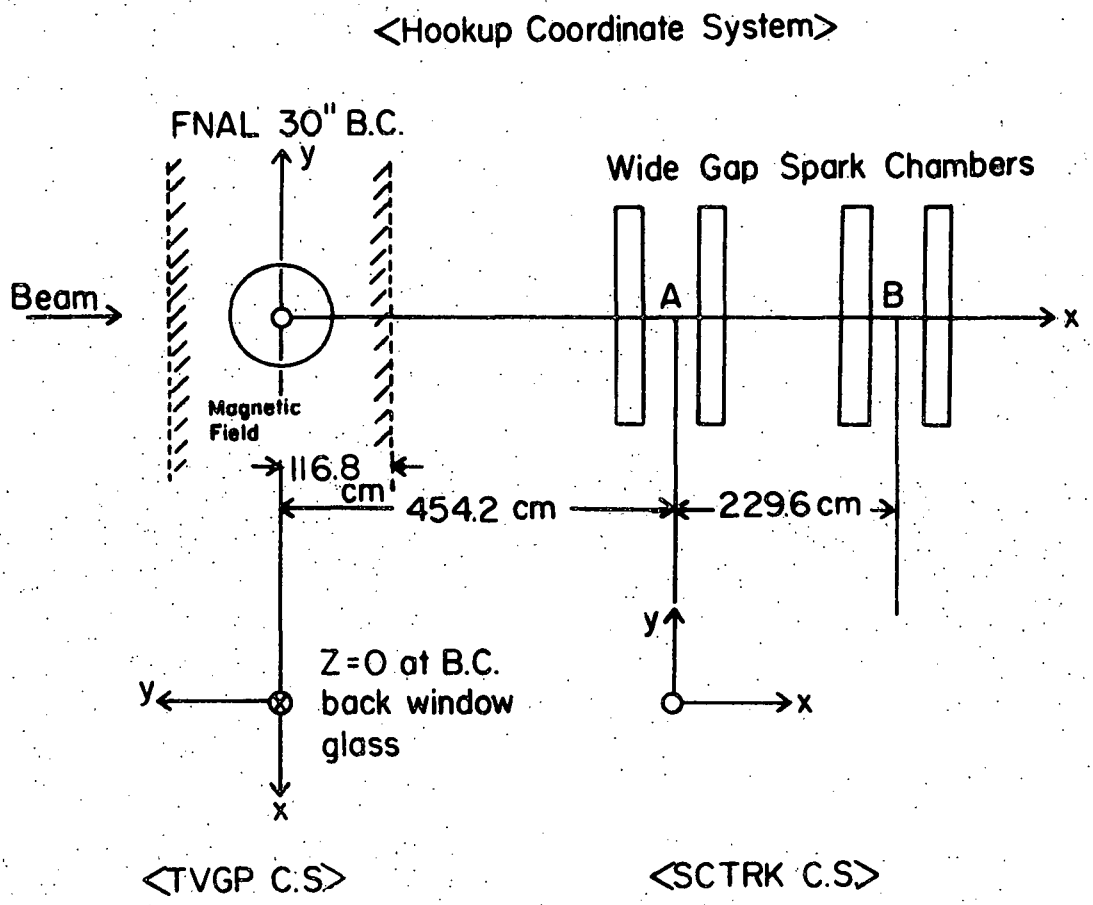

Figure 3.4. Coordinate systems for track reconstruction and HOOKUP.

(1) Transformation of TVGP coordinates to HOOKUP coordinate system.

$$\begin{pmatrix} X \\ Y \\ Z \\ \phi \\ \theta \end{pmatrix}_{\substack{\text{BC Tracks} \\ \text{in HOOKUP} \\ \text{coordinate system}}} = - \begin{pmatrix} Y \\ X \\ Z \\ \phi \\ \theta \end{pmatrix}_{\substack{\text{BC Tracks} \\ \text{in TVGP C.S.}}} + \begin{pmatrix} 0 \\ 0 \\ 0 \\ 3/2\pi \\ 0 \end{pmatrix} \qquad (3\text{-}3)$$

The necessary sign change (12) in the error matrix is also performed.

(2) Transformation of SCTRK coordinates to HOOKUP coordinate system.

$$\begin{pmatrix} X \\ Y \\ Z \\ \phi \\ \theta \end{pmatrix}_{\substack{\text{SC Tracks} \\ \text{in HOOKUP C.S.}}} = \begin{pmatrix} X \\ Y \\ Z \\ \phi \\ \theta \end{pmatrix}_{\substack{\text{SC Tracks} \\ \text{in SCTRK C.S.}}} + \begin{pmatrix} 454.2 \\ AA\ (2) \\ AA\ (3) \\ AA\ (4) \\ AA\ (5) \end{pmatrix} \qquad (3\text{-}4)$$

The transformed BC track position is compared with the transformed SC track position at a fixed X position: (X = 454.2 plane in the HOOKUP coordinate system; see

Figure 3.4). Three steps are needed to find the values of the physical variables for each hooked-up track. The details are described in Reference 11. We shall summarize here the basic ideas.

1. First Step: After transformation (3-3), the vector for the BC track at the exit point is defined as

$$V = \begin{pmatrix} Z \\ \theta \\ y \\ \phi \\ P \end{pmatrix}$$ along with an associated error matrix σ = (5 x 5) errors.

The program then follows this track through the BC Bending Magnet area and the following drift or free space. The position is then calculated in the plane at X = 454.2 cm. By first order beam transport theory, the extended position is given by

$$V^b = R \text{ (drift) } x \text{ } R \text{ (bending) } V$$

$$\text{where } V^b = \begin{pmatrix} Z^b \\ \theta^b \\ Y^b \\ \phi^b \end{pmatrix} \qquad (3\text{-}5)$$

where R is the beam transport matrix. This matrix R uses

the quantities β (the deflection angle), ℓ and s that are shown in Figure 3.5.

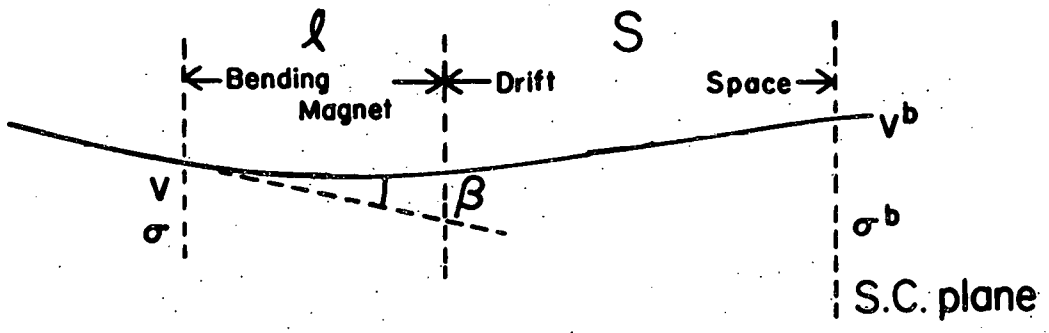

Figure 3.5. The deflection in the BC fringe field.

The values of ℓ and s in Experiment 2B are:

Bending Length (ℓ) = 116.84 - X of the BC end point.

Drift Length (s) = 337.36 cm.

The error for V^b: σ^b is given by

$$\sigma^b = R\sigma R^T \cdots \text{(4 x 4) errors} \cdots \tag{3-6}$$

2. Second Step: After the transformation (3-4), the SC track position at fixed X = 454.2 cm is written as

$$V^s = \begin{pmatrix} Z^s \\ \theta^s \\ Y^s \\ \phi^s \end{pmatrix} \tag{3-7}$$

with the associated error matrix

$$\sigma^s = (4 \times 4). \tag{3-8}$$

Using the transformed BC and SC track positions and the associated errors (equations 3-5,6,7,8), the best HOOKUP candidate(s) are found by taking the lowest value of χ^2, defined as:

$$\chi^2 = (V^b - V^s)^T \, (\sigma_b + \sigma_s)^{-1} \, (V^b - V^s) \tag{3-9}$$

3. Third Step: If any HOOKUP candidate(s) are found, the quantities $\alpha \equiv (\phi, \lambda, \kappa) = (\phi, \tan\theta, (p\cos\theta)^{-1})$ at the BC vertex are calculated. The BC measurement variables and errors at the vertex are defined as

$$\alpha_m \equiv \begin{pmatrix} \phi_m \\ \lambda_m \\ \kappa_m \end{pmatrix} = \begin{pmatrix} \phi_m \\ \tan\theta_m \\ (p_m \cos\theta_m)^{-1} \end{pmatrix}$$

with σ_m being the associated 3 x 3 error matrix.

The program calculates the set of parameters α, which fit both the BC measurement and the SC measurement, this is an α which minimizes

$$\chi^2 = (V^s - V^b(\alpha))^T (\sigma_s + \sigma_c)^{-1} (V^s - V^b(\alpha))$$

$$+ (\alpha_m - \alpha)^T \sigma_m^{-1} (\alpha_m - \alpha) \tag{3-10}$$

where σ_c is the Coulomb scattering error for the medium between BC and SC. This χ^2 means that there are two independent measurements of α. The details of the fitting program are described in Reference 11. Here only the methods used to determine AA parameters defined by Eq. 3-4 are discussed.

Using the beam track pictures taken simultaneously by BC and SC, the AA parameters are determined; the BC - SC HOOKUP based on these parameters are then required to satisfy the following four conditions:

a. The distribution of χ^2 defined by (3-9) should have a peak at 2 for 4 degrees of freedom; also the χ^2 defined by (3-10) has 4 degrees of freedom (= 7-3) and its peak should be at $\chi^2 \simeq 2$.

b. The peak of the distribution of $(V^b - V^s)$ should be at 0.0.

c. The momentum distribution should have a peak at 300 GeV/c for the present experiment.

d. The "pulls" for matching have the mean values at about 0 and a standard deviation $\sigma \simeq 1$. The pulls are defined as

$$\text{Pull } (\alpha) = \frac{\alpha_{fit} - \alpha_{meas.}}{[(\Delta\alpha_{meas.})^2 - (\Delta\alpha_{fit})^2]^{\frac{1}{2}}}$$

Using 300 GeV/c beam tracks (Roll 821), AA parameters were determined, which are shown in Table 3.4.

Table 3.4. AA-Parameters

Parameter in HOOKUP Program	AA(1) X (cm)	AA(2) Y (cm)	AA(3) Z	AA(4) θ (radians)	AA(5) ϕ (radians)
	454.2	-26.27	80.17	-0.0049	-0.0015

The intrinsic errors of SC tracks that were used in HOOKUP are summarized in Table 3.5.

Table 3.5. SC Errors

Number of Modules Used	dZ (cm)	dθ (mrad.)	dY (cm)	dϕ (mrad.)
1	0.50	3.0	0.10	2.0
2	0.25	1.5	0.10	0.5

One now needs to examine whether the four conditions mentioned earlier are satisfied. First, the HOOKUP beam momentum distribution shown in Figure 3.6 is centered at 300 GeV/c. The Full Width at the Half Maximum (FWHM) is 70 GeV/c, which corresponds to 10% error. This is a dramatic improvement in the accuracy of the measurement.

Figure 3.7 shows the χ^2 (defined by 3-10) for HOOKUP beam track, which is centered at 2. Figure 3.8a through 8d show the distributions $(V^b - V^s)$ for each of the possible variables. For each variable the Half Width at the Half Maximum of the distribution is given in Table 3.6.

Table 3.6. HWHM of BC (Extended)-SC.

Roll	Y (cm)	Z (cm)	θ (mrad.)	ϕ (mrad.)
821 (300 GeV/c Beam)	0.10	0.55	2.5	0.55

In the next seven figures, Figure 3.9a to 9g, the "pulls" for the variables associated with the track matching are shown. The "pull" widths for 300 GeV/c HOOKUP beam are summarized in Table 3.7. In general, the performance of HOOKUP is satisfactory for the beam track, except for the narrow widths seen in the "pulls" for the curvature and the azimuthal angle at the BC vertex. This may reflect the fact that the full length of the beam was measured in the BC for each of these HOOKUP beam tracks. As a means of investigating this problem, the "pull" widths for HOOKUP tracks from subsamples of 2, 4 and 6 prong events are also shown in Table 3.7. For the HOOKUP of these events, the AA parameters determined from 300 GeV/c beam track data

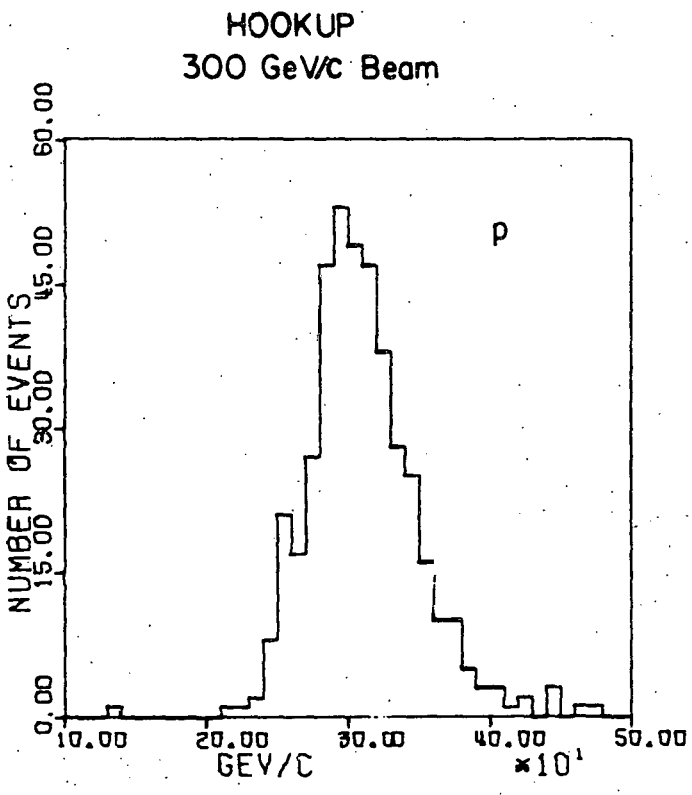

Figure 3.6. Momentum distribution of HOOKUP beam tracks.

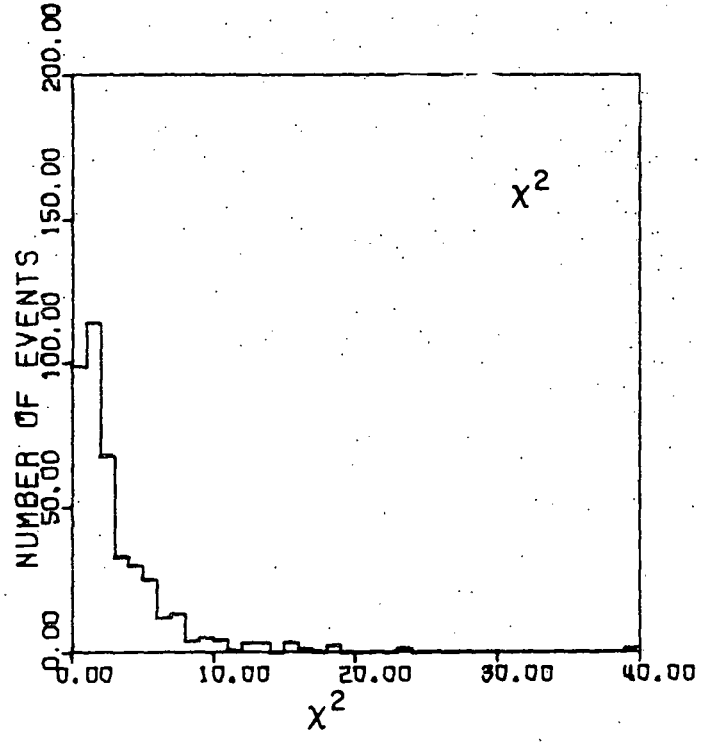

Figure 3.7. HOOKUP χ^2 distribution of beam tracks.

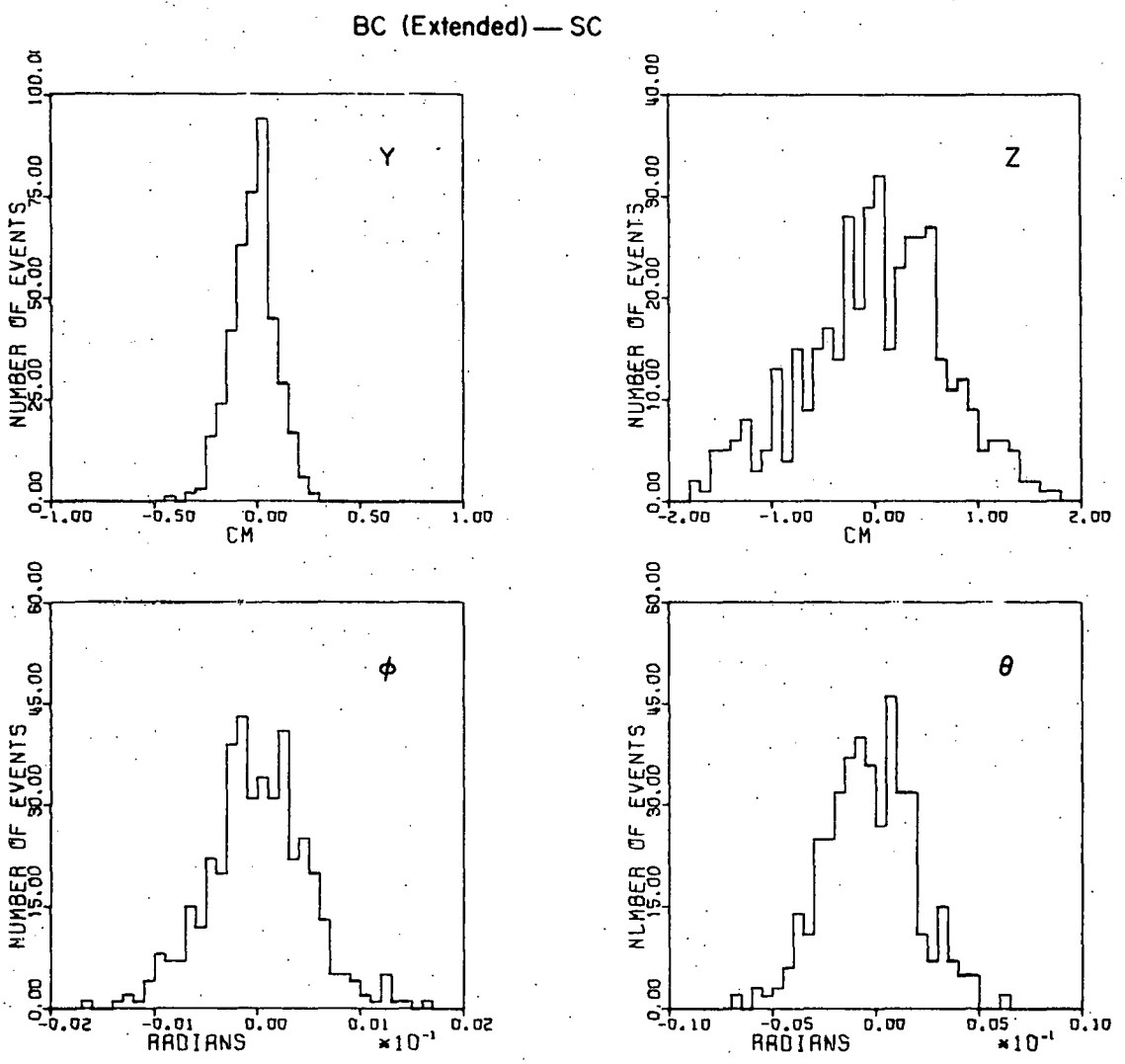

Figure 3.8. The difference $V^b - V^s$ at the SC plane.

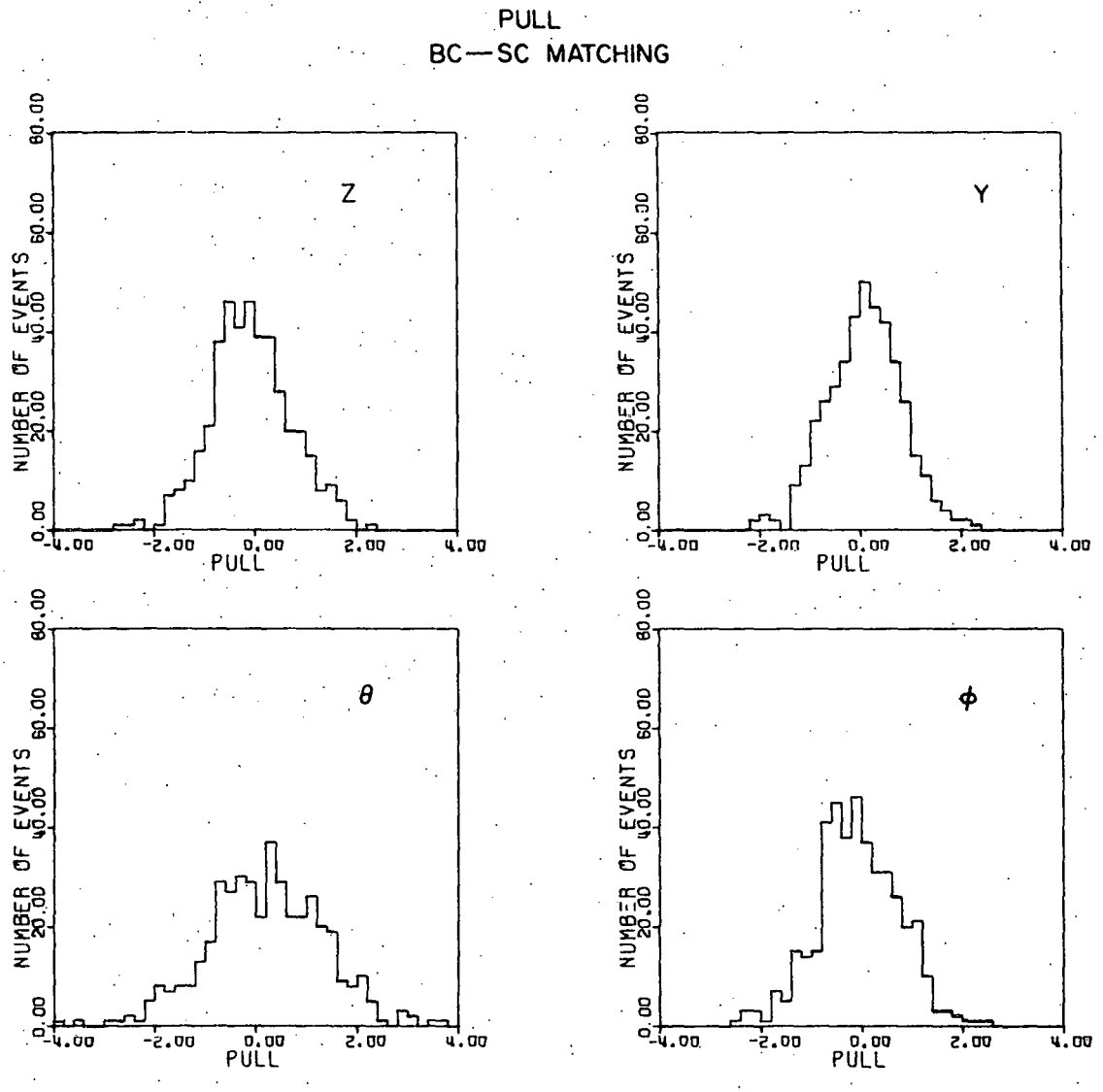

Figure 3.9. The pull distribution of HOOKUP.

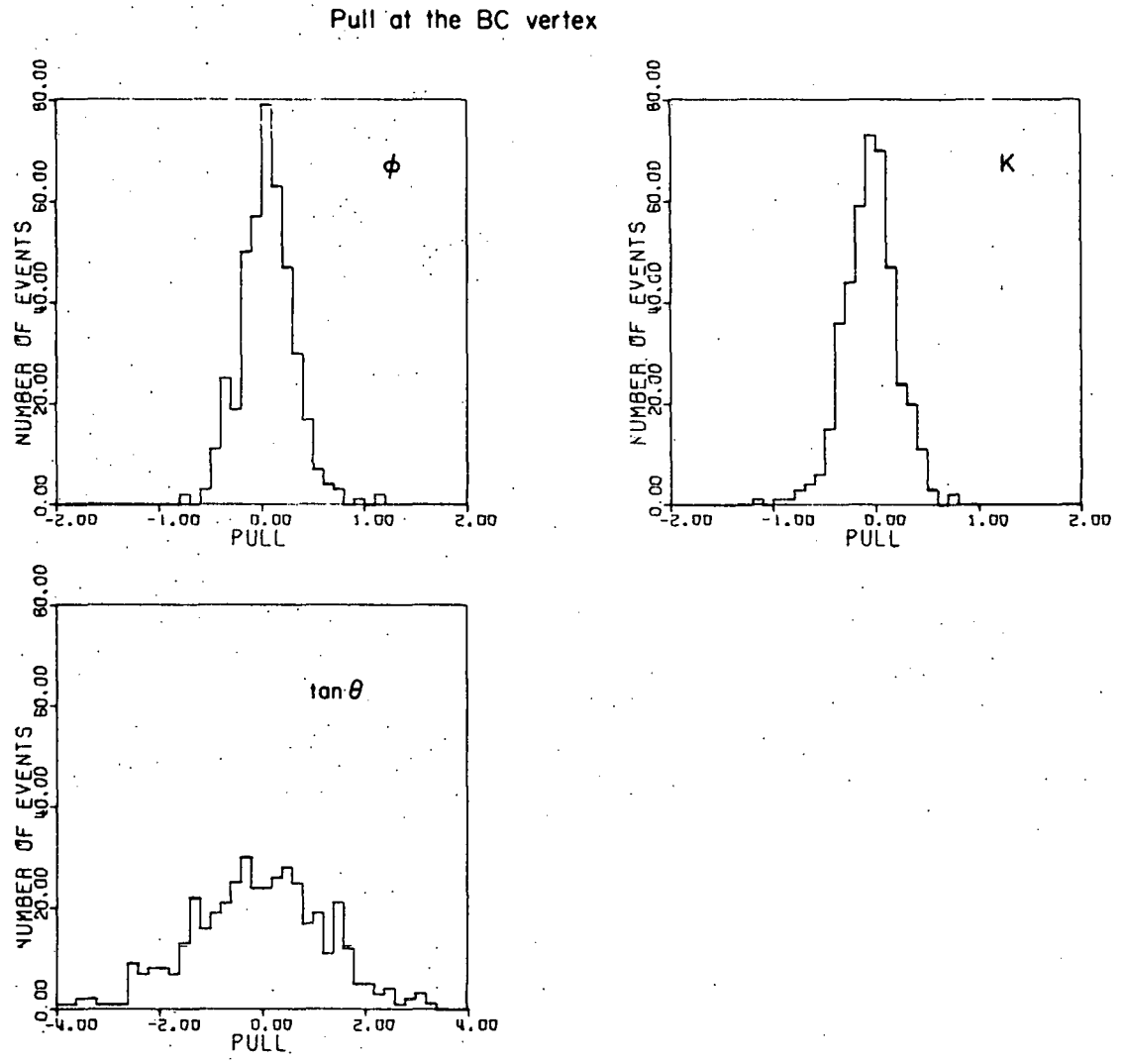

Figure 3.9. (Continued).

were used. In order to avoid contribution from false BC - SC matching, only events whose SC track number does not exceed the BC prong number were used for the HOOKUP of 2, 4 and 6 prongs. The cut on χ^2 of HOOKUP tracks, which will be shown in chapter IV was 25.

Table 3.7. Pull Widths.

Event Type	Number of HOOKUP Tracks	$\sigma_{Z_{sc}}$	$\sigma_{\theta_{sc}}$	$\sigma_{Y_{sc}}$	$\sigma_{\phi_{sc}}$	σ_{AZ}	ϕ_{SLP}	σ_K
300 GeV/c Beam	444	0.68	1.02	0.76	0.68	0.21	1.27	0.21
2, 4 and 6 prongs	507	0.93	0.76	0.93	0.85	0.68	1.44	0.59

The "pull" widths for HOOKUP 2,4 and 6 pronged events are somewhat narrow, but are consistent with one, so that no attempt was made to introduce a scale factor in the error matrix for TVGP track variables. The centers of the pull distributions for HOOKUP 2, 4 and 6 pronged events are slightly offset from zero; however they are within one standard deviation of zero. Under the restriction that only clean SC events are used, the HOOKUP performance is again satisfactory for real events.

Since the beam deflection in the magnetic field occurs vertically, the fitted momentum distribution is sensitive to the variation of the vertical component (Y) of the AA parameters. Thus extreme care must be exercised when the AA parameters are changed or adjusted. The detailed studies of HOOKUP also indicate that the BC single pulse operation yields better HOOKUP than multiple pulse operation and that the use of 2 SC modules achieves better HOOKUP results than using only one module.

IV. KINEMATIC FITTING AND THE BACKGROUND ANALYSIS

The bare BC events alone constitute the complete Data Set and they are first analyzed independent of the SC data. Each bare BC event is geometrically reconstructed by TVGP and then the kinematic fit is performed by SQUAW.[8] The program ARROW[9] is used to select out good 4-constraint events and then the Data Summary Tape (DST) for exclusive events is generated as well as a DST for semi-inclusive events, that is, all events in particular topologies independent of the results of kinematic fitting. The HOOKUP data is processed in a similar fashion. Section one of this chapter describes the bare BC data analysis and section two discusses the background in 4-constrained (4C) events by comparing bare BC 4C and HOOKUP 4C events. The bare BC data presented here is based on 16139 events of 2, 4 and 6 pronged samples taken during the initial experiment 2B running with the 30-inch Hydrogen BC and Wide-Gap Spark Chambers. The HOOKUP data are a compilation of data processed by Iowa State University and Michigan State University.

---

[8]SQUAW adopted for IBM 360/70 at Iowa State is a modified version of ANL SQUAW for IBM 360/75. We wish to thank the ANL group for providing us with this version of SQUAW (13).

[9]The ARROW program used at ISU is a modified version of the MSU version of ARROW (14). ISU version of ARROW displays the HOOKUP information together with TVGP and SQUAW results.

A. Analysis of Bare Bubble Chamber Data

The kinematic 4C fits are attempted for 2, 4 and 6 pronged events for the following hypotheses:

$$p + p \rightarrow p + p$$

$$p + p \rightarrow p + p + \pi^+ + \pi^-$$

$$p + p \rightarrow p + p + \pi^+ + \pi^- + \pi^+ + \pi^-$$

In SQUAW Fitting, the averaged angle and momentum are used for the beam track. The typical values for the "beam averaged variables" in the HOOKUP coordinate system (Figure 3.4) are shown in Table 4.1. The azimuthal angle of the beam at the interaction vertex is calculated from the azimuthal angle at the BC entrance, the beam length and the magnetic field.

Table 4.1. Beam Average.

	200 GeV/c	300 GeV/c
Beam Momentum Error	± 4 GeV/c	± 5 GeV/c
Azimuthal angles at the BC entrance	5.2 mrad.	4.3 mrad.
Dip Angle	1.0 mrad.	0.5 mrad.

Initially all the 4C events with SQUAW χ^2 less than 150 are accepted. The disposition of events used in this anal-

ysis is presented in Table 4.2 for 300 GeV/c pp and in Table 4.3 for 200 GeV/c pp data. The events are rejected if they have an unacceptable fiducial measurement or an unmeasurable track or are not in the fiducial volume.

The fiducial volume restrictions imposed on the BC at the scanning stage are different at ISU and at the collaborating institutions. The fiducial volume used at ISU is 42 cm long in the beam direction (-21 cm $< x <$ 21 cm in Figure 3.4). MSU uses the same downstream cut at 21 cm; however their upstream edge is located about 8 cm further upstream than the ISU limit. The distribution of vertex X positions for 4 pronged 4C and 6 pronged 4C events with $\chi^2 \leq 30$ is shown in Figure 4.1. The well-measured events that were used for the analysis of the 4C channels comprise about 78% of the total measured events; namely 16139 events out of 20704 events. This reduction of events is mainly due to the measuring difficulties which subsequently cause TVGP failures.

Before making any further χ^2 cut on 4C events, the following selection criteria are applied to the SQUAW-ARROW output.

a. The Ionization Check: If the track with the slow proton flag has TVGP momentum less than 1.4 GeV/c, the proton interpretation is automatically accepted.

b. Cut on Feynman X Variable of Track: If has been reported (7) that the symmetric track distribution in the

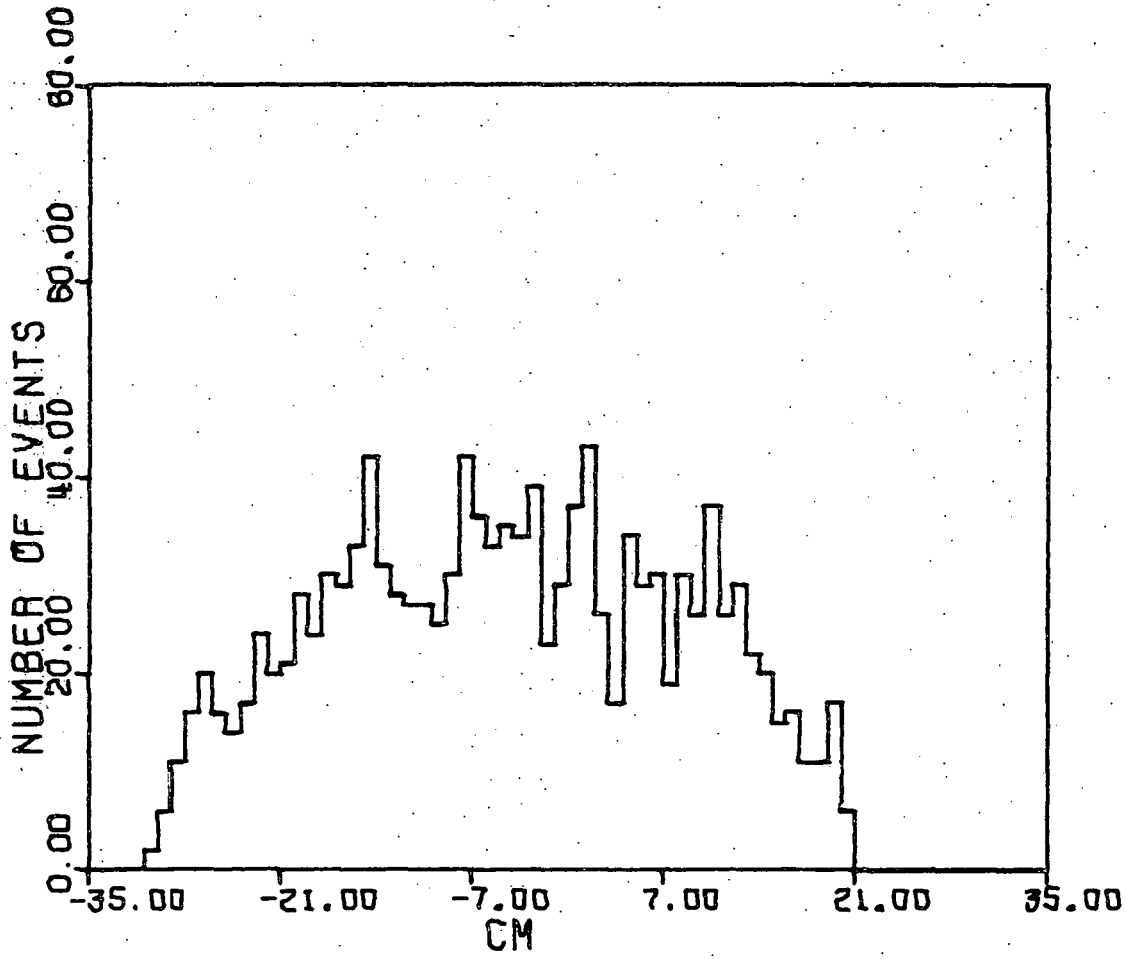

Figure 4.1. The position of the vertex along the incident beam direction; $pp \rightarrow pp\,\pi^+\pi^-$ and $pp \rightarrow pp\,\pi^+\pi^-\pi^+\pi^-$ at 200 and 300 GeV/c with $\chi^2 < 30$.

Table 4.2. pp data at 300 GeV/c.

300 GeV pp	2-Prongs			4-Prongs			6-Prongs		
	MSU FNAL	ISU	SUM	MSU FNAL	ISU	SUM	MSU FNAL	ISU	SUM
Number Measured	1969	1491	3460	1779	883	2662	2109	894	3003
PANAL Fails or Rejects	47	144	191	148	109	257	217	140	357
Buffer Overflow	0	0	0	0	0	0	0	0	0
Bad Track	51	6	57	36	6	42	35	9	44
K-Pong Failure	21	45	66	33	25	58	65	34	99
2-Pointer	157	3	160	52	1	53	41	1	42
FRMS too Large	153	0	153	209	0	209	317	0	317
Well-measured Events	1558	1293	2851	1311	742	2053	1441	710	2151
4C' $\chi^2 < 150$	1125	952	2077	393	309	702	319	298	617

Table 4.3. pp data at 200 GeV/c.

200 GeV/c pp	2-Prongs			4-Prongs			6-Prongs		
	MSU ANL FNAL	ISU	SUM	MSU ANL FNAL	ISU	SUM	MSU ANL FNAL	ISU	SUM
Number Measured	4188	552	4740	2958	403	3361	3091	387	3478
PANAL Fails or Rejects	170	40	210	199	47	246	281	45	326
Buffer Overflow	0	0	0	0	0	0	17	0	17
Bad Track	113	2	115	83	6	89	72	1	73
K-Pong Failure	115	9	124	69	5	74	85	8	93
2-Pointer	184	3	187	56	0	56	53	1	54
FRMS too Large	263	0	263	244	0	244	324	0	324
Well-measured Events	3343	498	3841	2307	345	2652	2259	332	2591
4C' $\chi^2 < 150$	2321	365	2686	676	130	806	532	124	656

CM frame, which is required in pp interactions, is satisfied for the $pp \rightarrow pp\pi^+\pi^-$ channel if the pions are selected to be in the region of Feynman X between -0.6 and 0.6. The same cut is adopted in the present experiment for both 4-pronged 4C and 6-pronged 4C events. If the 4C fit does not have pions in this range, the event is completely discarded even if the χ^2 is low.

Figures 4.2a - 2f show the χ^2 distribution for the SQUAW fits after selections (a) and (b) are performed. In these distributions, the experimental features are beautifully displayed: the χ^2 distribution for the elastic events and 4-pronged 4C events are normal; the distributions of 6-pronged 4C events indicate a serious background problem. As the first step in understanding the problem, a chi-square cut of 30 is applied to all the data. The track distributions in the Center of Mass (CM) frame with this χ^2 cut are shown in Figure 4.3. It is, in fact, remarkable that with a χ^2 cut of 30, all channels have symmetric track distributions in the Feynman X variable. Without this χ^2 cut, the track distributions in X are poor, particularly for 6 pronged 4C events. Another interesting feature found in the previous experiment at 200 GeV/c (7) is a particular configuration of particles in the forward and backward hemisphere of the CM frame. Of the events in the $pp \rightarrow pp\pi^+\pi^-$ channel at 200 GeV/c, 87% had three particles in one hemisphere and one

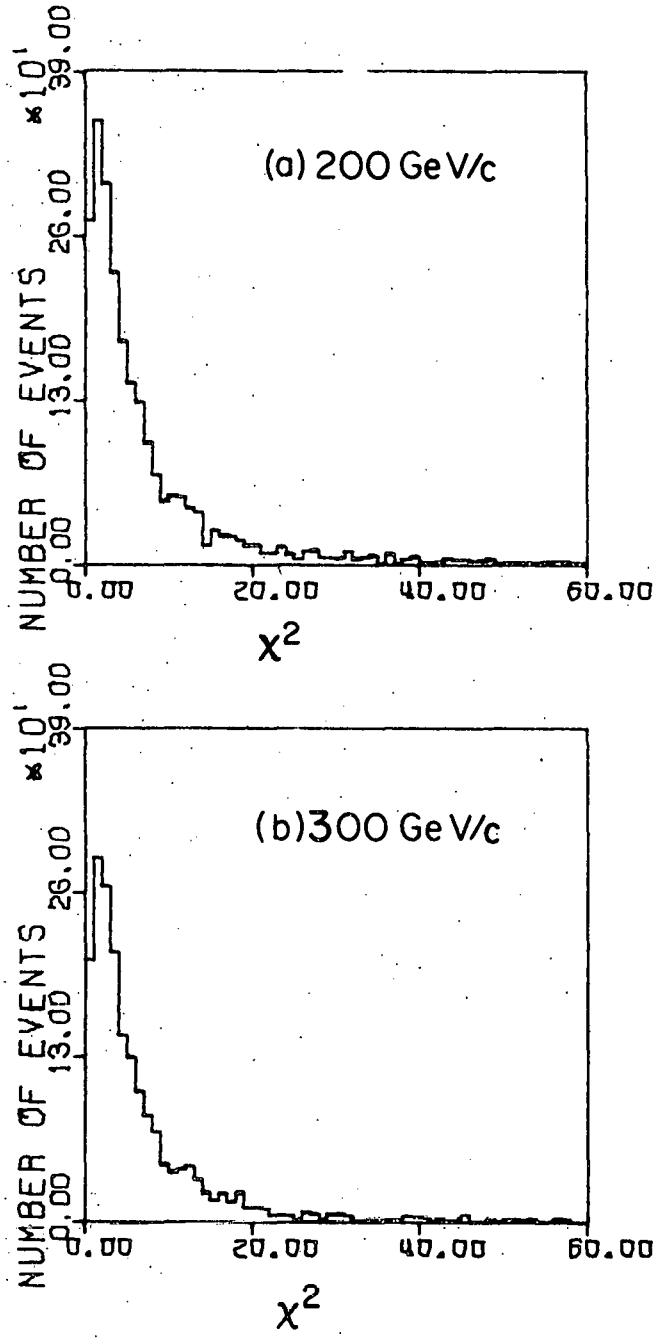

Figure 4.2. χ^2 distribution of SQUAW fitting; bare BC data only.

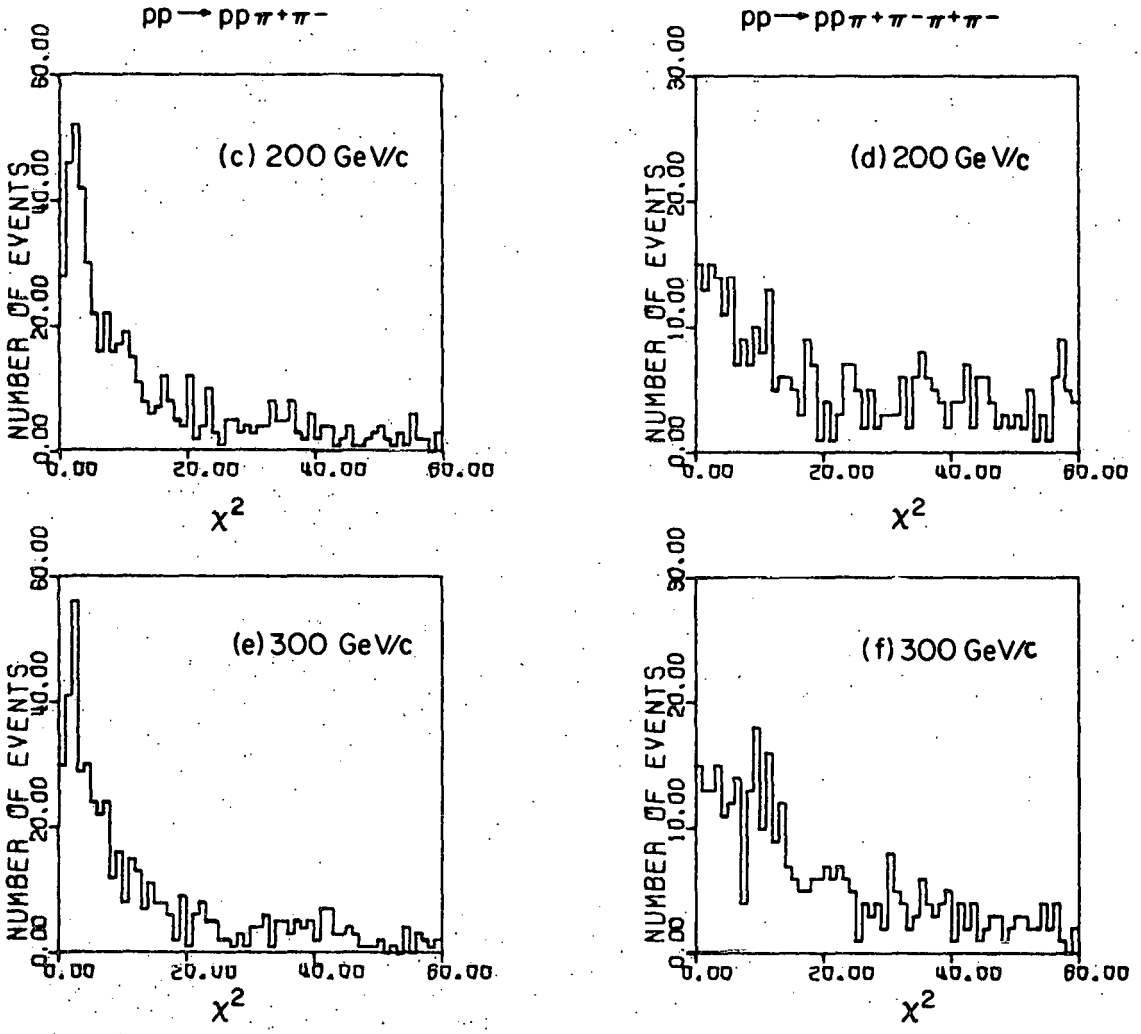

Figure 4.2. (Continued).

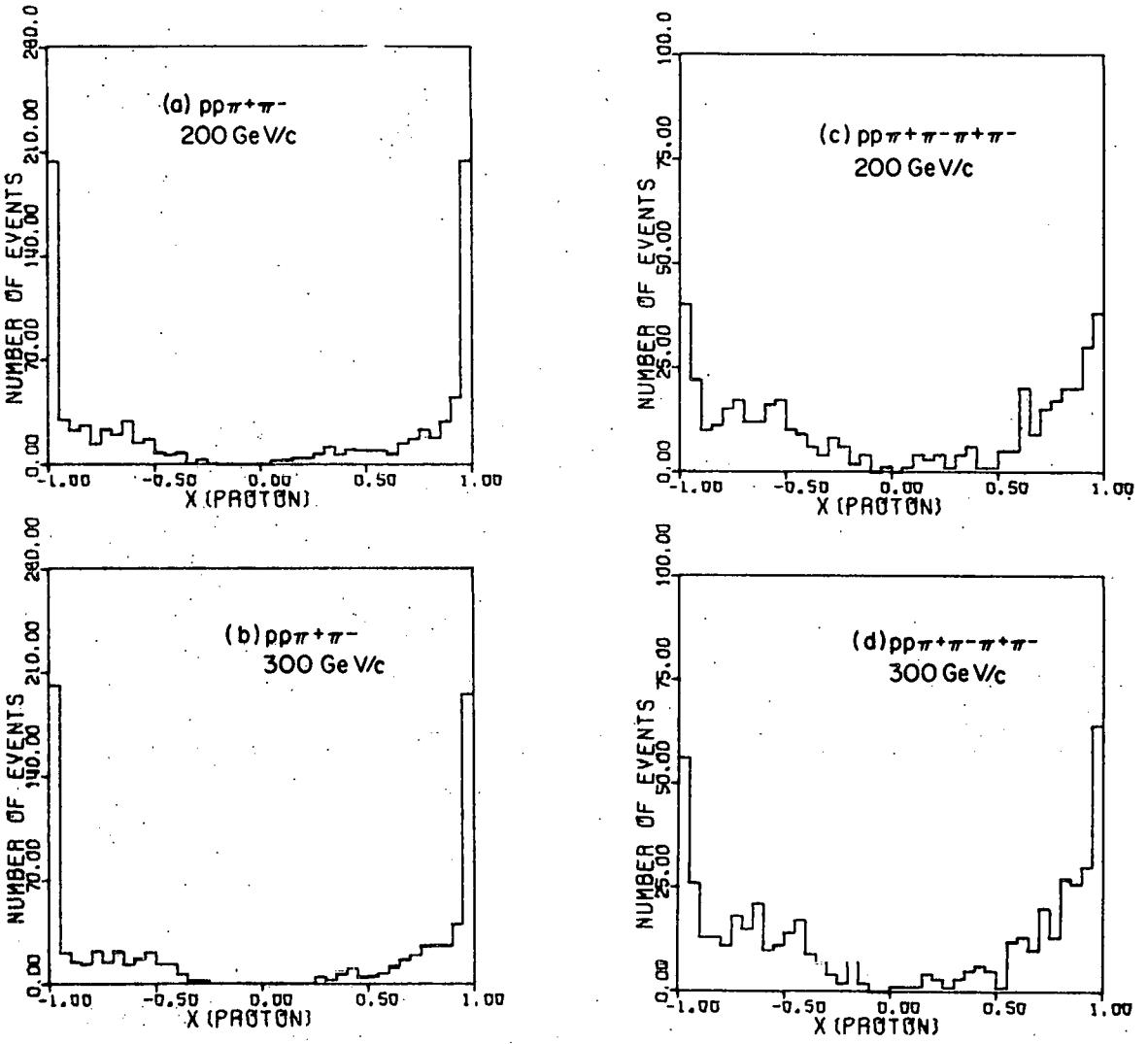

Figure 4.3. The distribution of the Feynman x variable; bare BC data only.

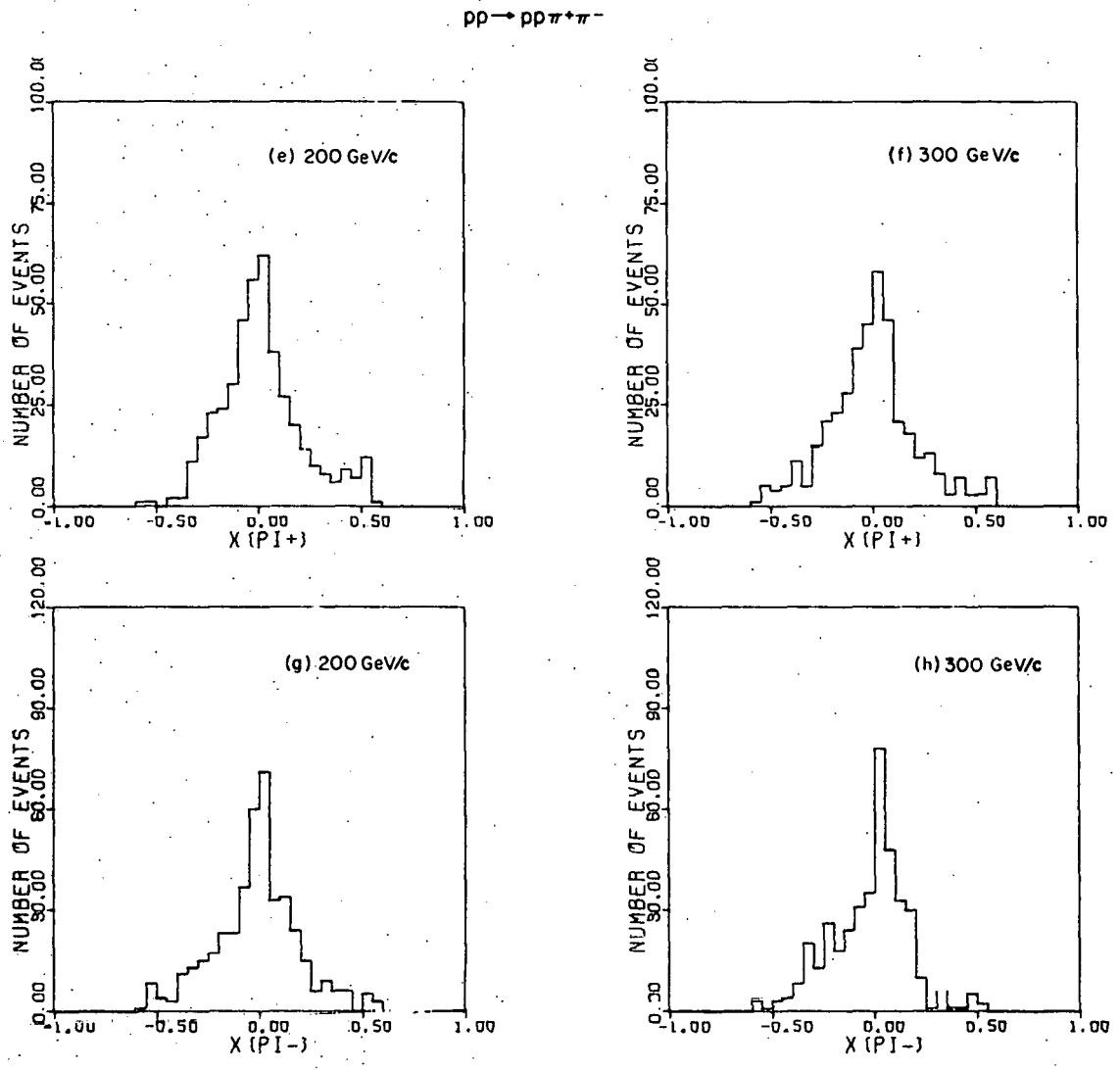

Figure 4.3. (Continued).

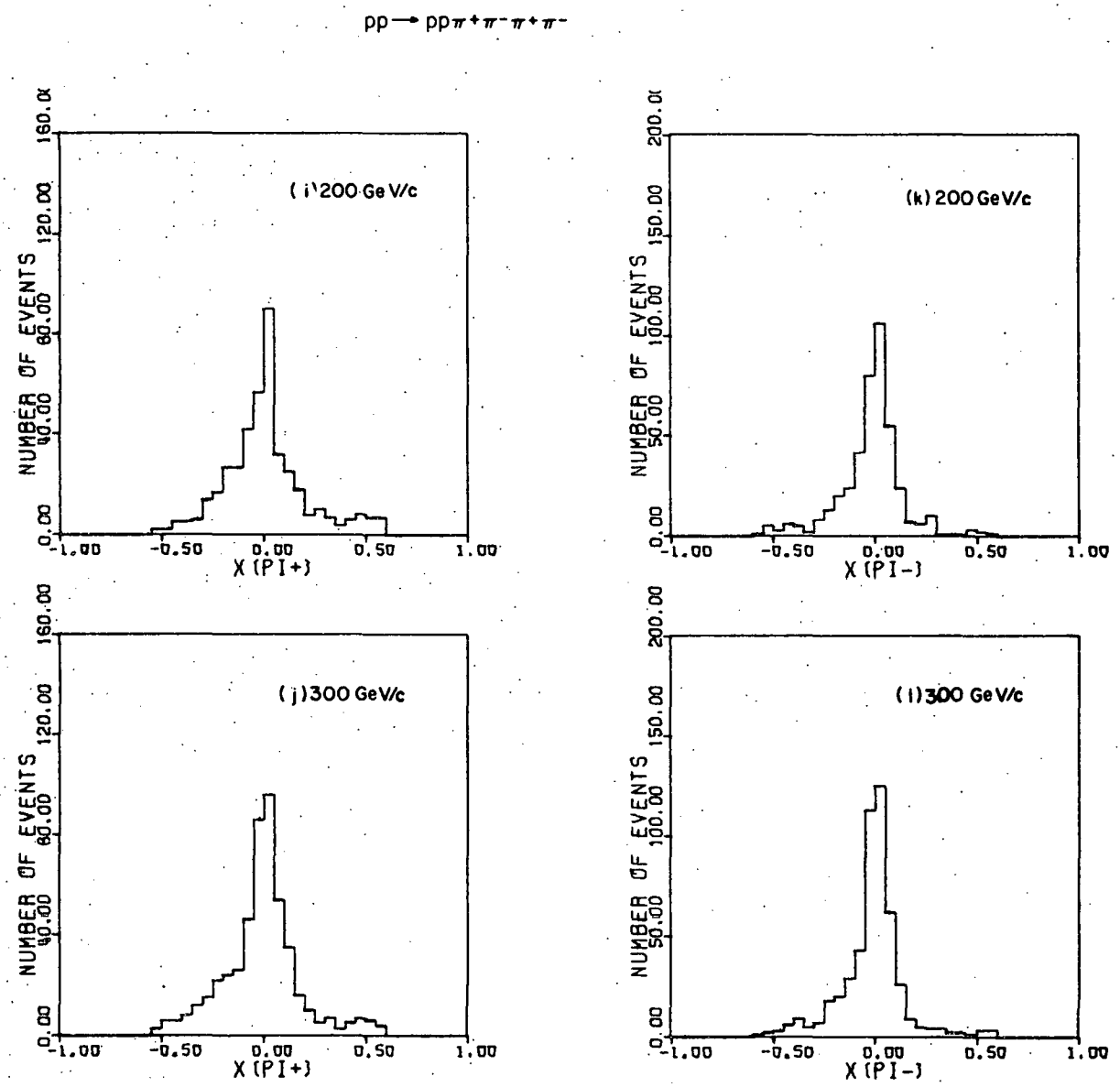

Figure 4.3. (Continued)

particle in the other hemisphere. The rest of the events had two particles in each hemisphere. Since the ratio between three forward particles and three backward particles was one, Derrick et al. (7), concluded that there were no losses in the kinematic fitting process. A similar test is made in the present experiment for 4 pronged 4C and 6 pronged 4C events with the χ^2 cut of 30 at each of the two energies. The location of a track in the CM frame is identified by the CM rapidity variable for the track. The results are shown in Tables 4.4a and 4.4b.

Table 4.4a. CM track distributions in $pp \to pp\pi^+\pi^-$.

p GeV/c	3(F) : 1(B)	2(F) : 2(B)	1(F) : 3(B)
200	188	52	187
300	169	50	182

Table 4.4b. CM track distributions in $pp \to pp\pi^+\pi^-\pi^+\pi^-$.

p GeV/c	1(F) : 5(B)	2(F) : 4(B)	3(F) : 3(B)	4(F) : 2(B)	5(F) : 1(B)
200	34	43	58	41	37
300	50	48	66	39	48

Table 4.4c shows the charge distribution in the forward (or backward) hemisphere for the 6 pronged 4C events with a χ^2 cut of 30 and a 3 to 3 division of the particles between the forward and backward hemispheres: this result is used in Chamber 5 in the study of double diffraction.

Table 4.4c. Charge distribution[a] in the forward hemisphere.

p GeV/c	1+ : 2-[b]	2+ : 1-	3+ : 0-
200	4	52	2
300	6	55	5

[a] 6 pronged 4C events with 3 to 3 division of particles only.

[b] The notation indicates that 3 particles in the forward hemisphere consist of 1 positive and 2 negative charges.

The results shown in Table 4.4a and 4.4b are consistent with the results observed by Derrick et al. (7). As far as these data are concerned, there appears to be no loss of events in the kinematic fitting process. However, it is not possible to rule out all background problems simply with a chi-square cut alone. Because of a large measurement error for the fast-forward-going track, SQUAW can adjust the momen-

tum value by a large amount without large increases in χ^2. In the next several figures, this point is clearly demonstrated. The missing mass square distributions for 4-pronged 4C and 6-pronged 4C events with a χ^2 cut of 30 are shown in Figures 4.4: 4a and 4b for 200 GeV/c data and 4c and 4d for 300 GeV/c data. In Figures 4.5a and 4.5b, the momentum imbalances for the channel $pp \rightarrow pp\pi^+\pi^-$ are shown (with χ^2 cut of 30) in the scatter plots with the projection on each axis at 200 and 300 GeV/c. Even after the chi-square cut of 30 is applied, one sees many events with large missing mass square and a large momentum imbalance. It is evident in these figures that the resolution gets worse as the multiplicity and the beam momentum increase. As the CM track distributions (Figure 4.3) clearly show, the two protons in each channel are often the most energetic particles in the CM frame. This means that the beam associated proton in the laboratory frame is often the fastest track. The BC measurement error for this proton is large and this in turn causes the difficulty. Thus it is interesting to study the distributions of the missing mass square with respect to the group of particles but excluding the fast-forward proton. This has been named the XMSQ distribution. With the fast proton eliminated, the background problem can be studied more efficiently. Figures 4.6a through 4.6d show the XMSQ distributions for the two exclusive channels at 200 and

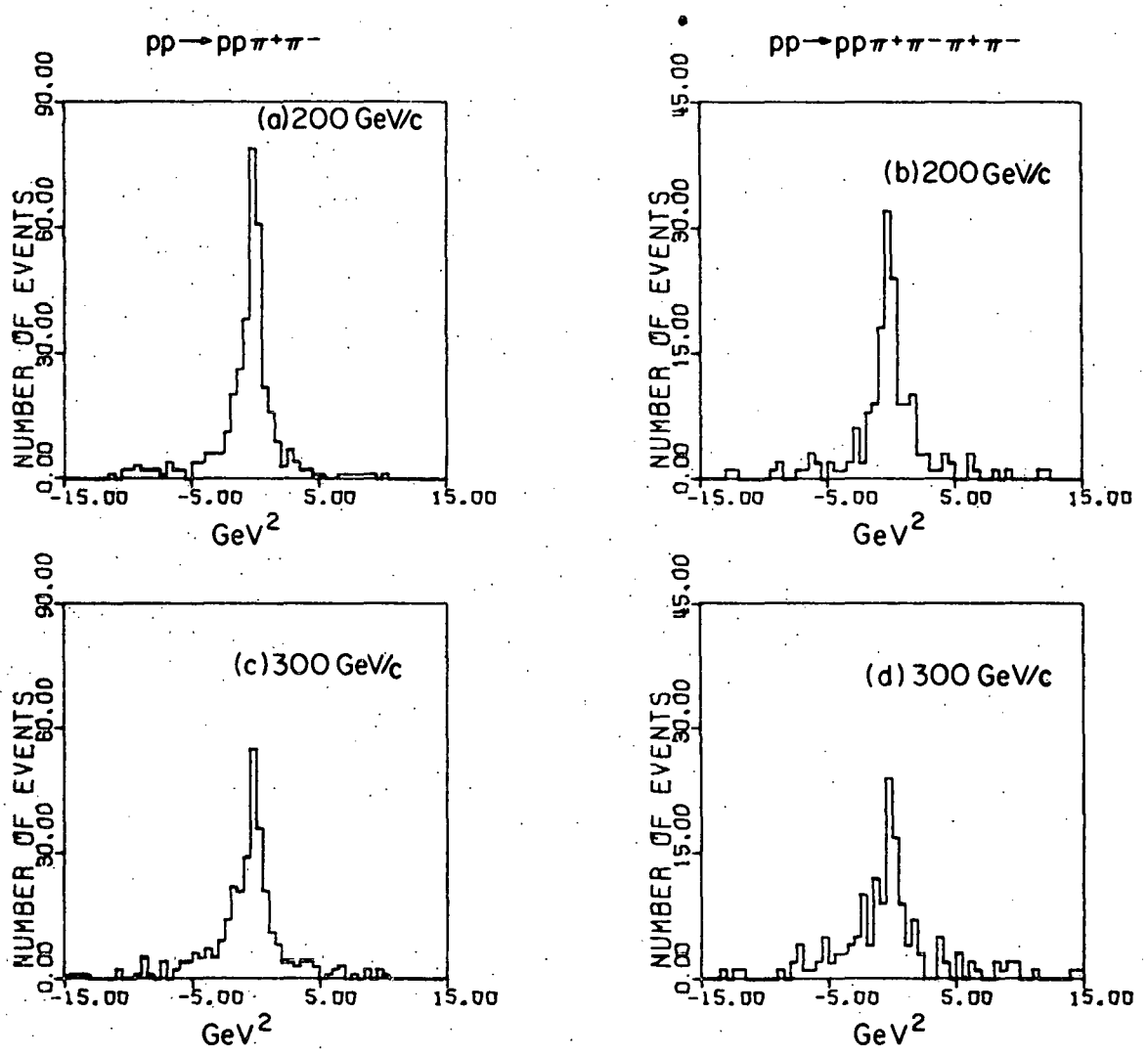

Figure 4.4. Missing-mass squared (MM^2) distribution for $pp\,\pi^+\pi^-$ and $pp\,\pi^+\pi^-\pi^+\pi^-$ final states at 200 and 300 GeV/c; bare BC data only.

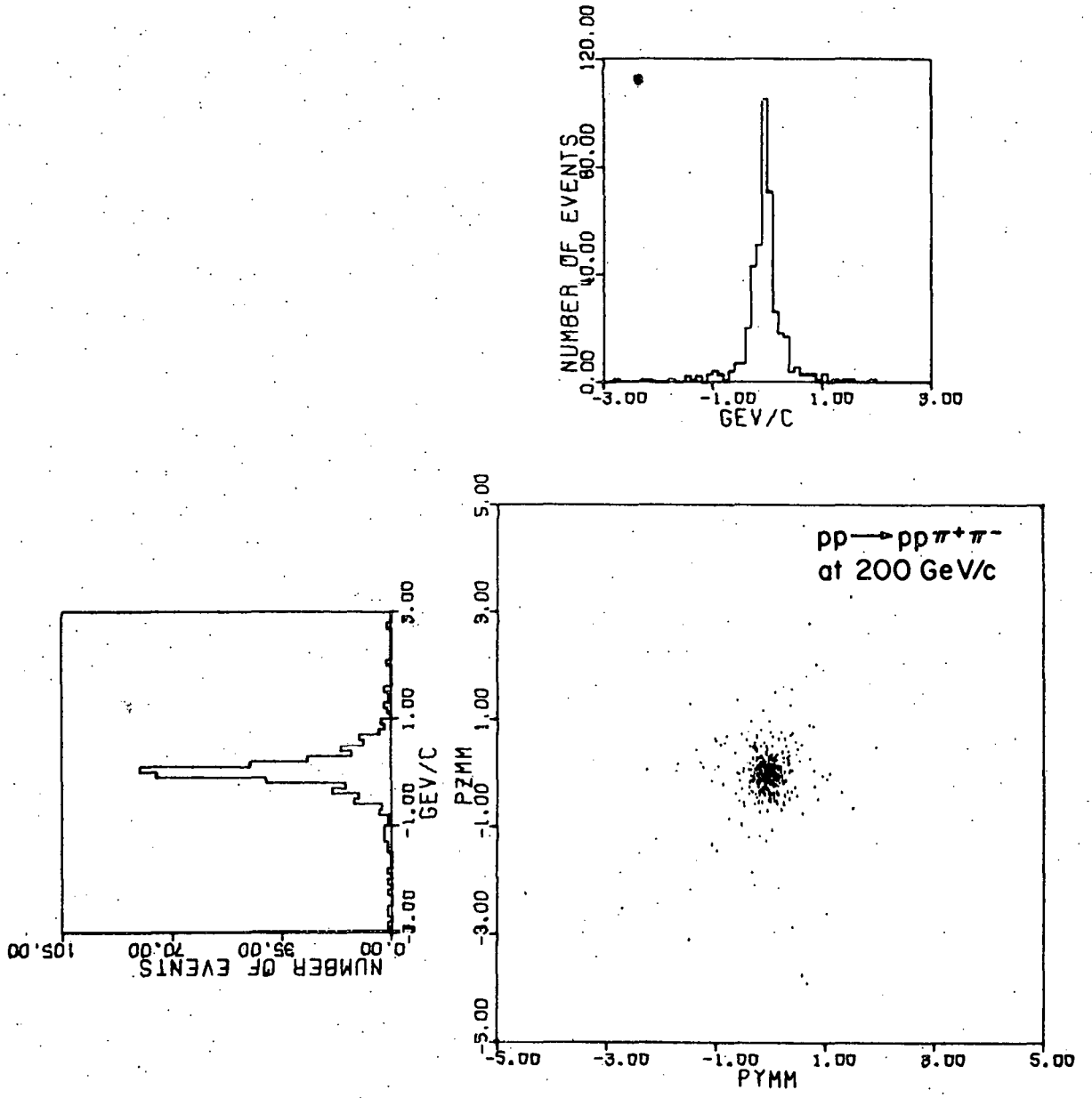

Figure 4.5. Scatter plot of the missing momenta in the plane perpendicular to the beam direction; bare BC data only.

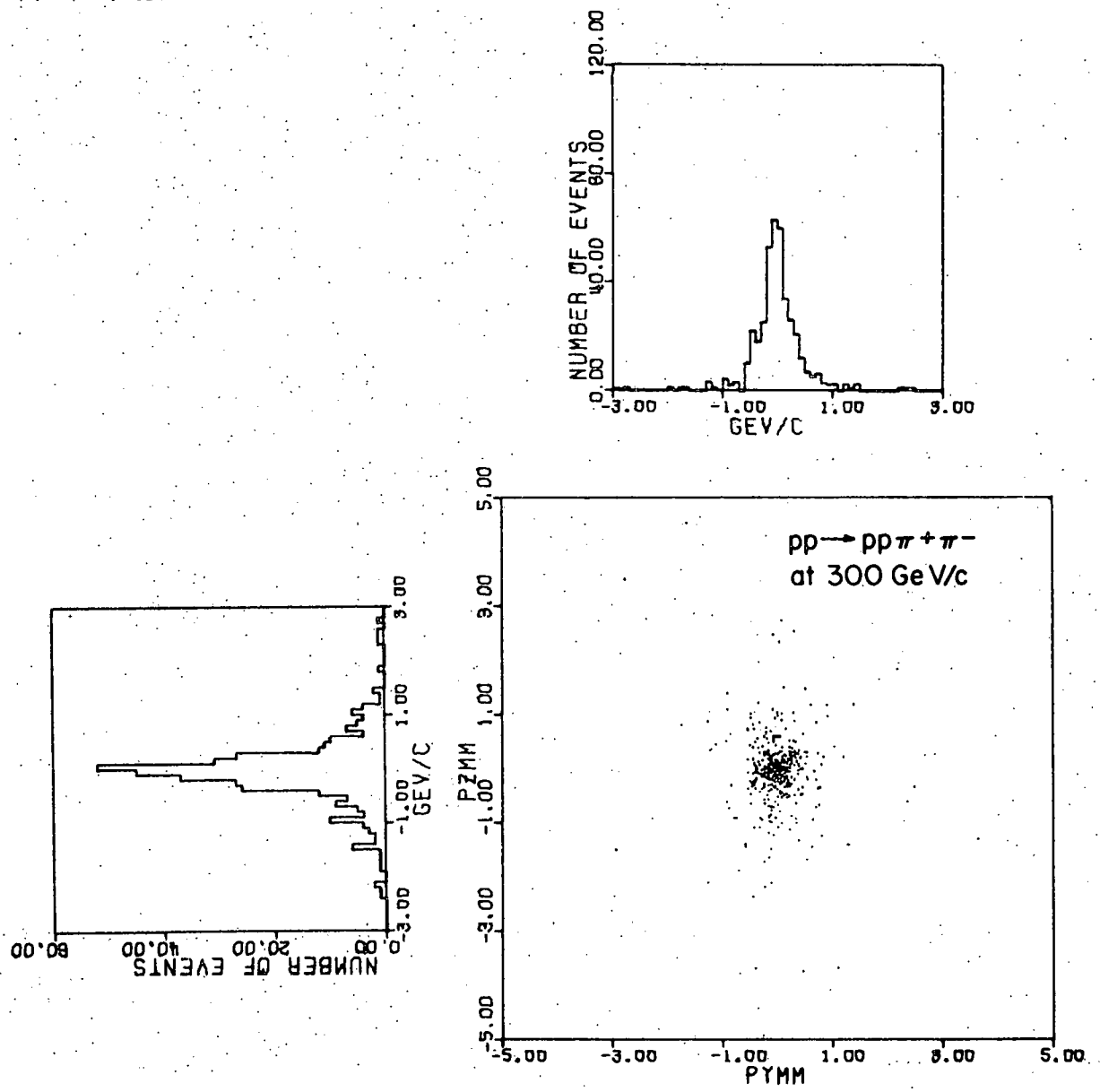

Figure 4.5. (Continued)

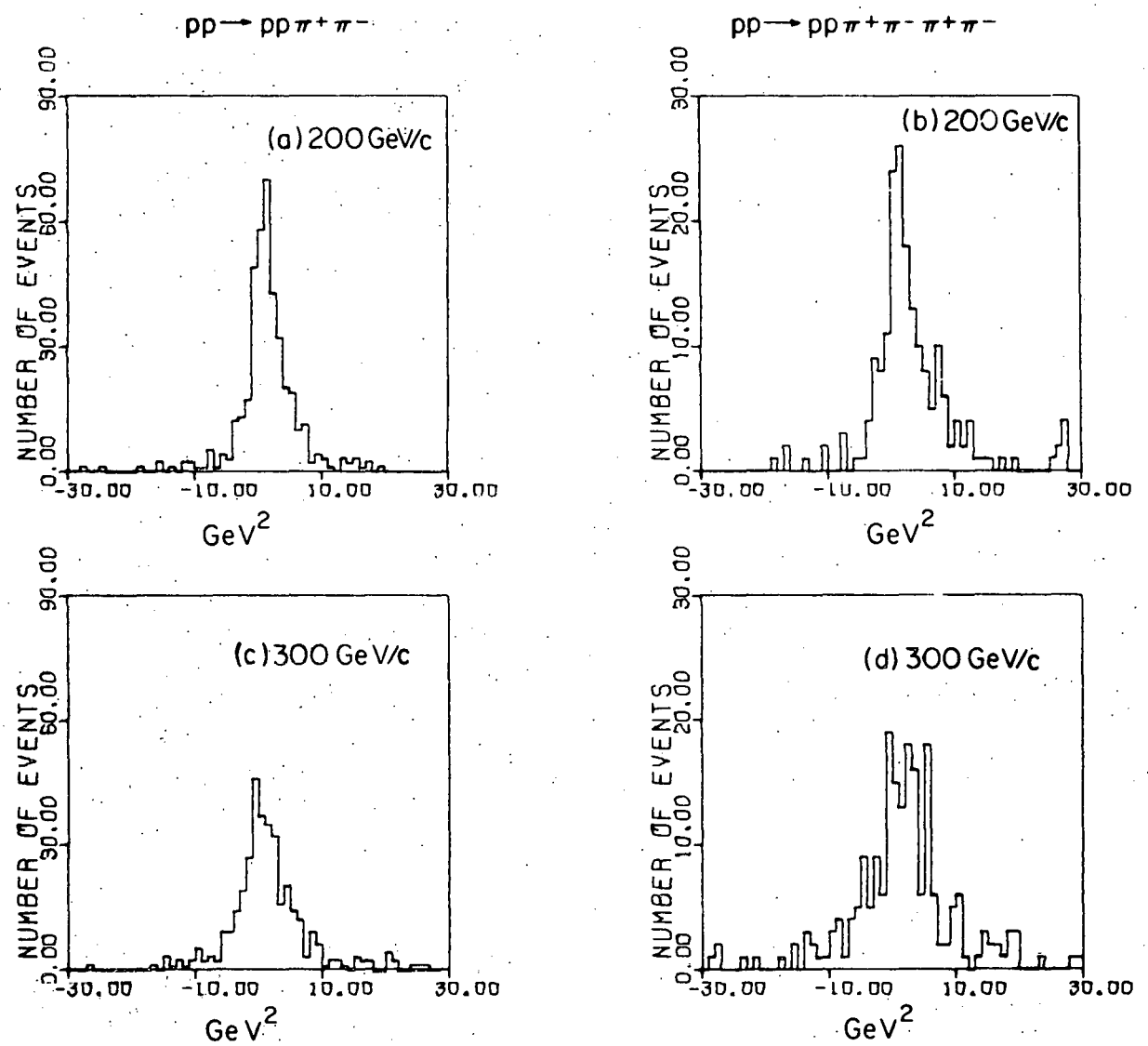

Figure 4.6. The XMSQ distributions for the final states $pp\,\pi^+\pi^-$ and $pp\,\pi^+\pi^-\pi^+\pi^-$ at 200 and 300 GeV/c; bare BC data only.

300 GeV/c with the chi-square cut of 30. Most of the distributions are centered at the proton mass square as expected. Again the width of the distributions increase as the multiplicity and the energy increase. The width of the XMSQ distributions also depends strongly on the division of particles in the CM frame.

The events located in the tails of the XMSQ distributions in Figure 4.6 are most likely inelastic events. Thus one tentatively adopts the following cut on 4-pronged 4C and 6-pronged 4C events:

$$-3.0 \text{ GeV}^2 < \text{XMSQ} < 5.0 \text{ GeV}^2 \qquad (4\text{-}1)$$

The estimated contamination of inelastic events is shown in Table 4.5 for all the available data.

Table 4.5. The contamination estimated by XMSQ cut.

p GeV/c	n	# of Events	4C $\chi^2 < 30$ (A)	4C with XMSQ Cut	Estimated Inelastic Events in (A)
200	4	2652	427	302	29%
200	6	2591	213	119	44%
300	4	2053	401	232	42%
300	6	2151	251	102	59%

So far the problems in kinematic fitting with bare BC events at these high energies have been pointed out, and a rough estimate of the contamination from inelastic events has been made. However, another aspect of the background, namely, the loss of real 4C events has not yet been discussed. As the multiplicity increases, it is expected that the background becomes larger, but at the same time there may be increased losses associated with the difficulties in doing the kinematic fits for high momentum tracks with large errors. In the next section, both the contamination and the losses in the bare BC 4C data are studied using HOOKUP data.

B. Background Studies using HOOKUP DATA

In the previous section, an extensive study was made of the background for bare BC 4C data. Yet, the reliability of the estimate must still be examined. Obviously, the fundamental solution of the problem is to improve the accuracy of the track measurement and to minimize the uncertainty in the kinematic fitting. Using the high quality HOOKUP data from the present experiment (the momentum resolution of the Experiment 2B Hybrid System is approximately $\frac{\Delta p}{p} = 0.04\ p\%$), two unique methods are employed to study the background of bare 4C events. They are: (1) study of the kinematic distributions of HOOKUP 4C events and (2) comparison of the bare BC 4C and HOOKUP 4C data on an event-by-event basis.

1. Bubble chamber and spark chamber track matching by HOOKUP

The details of the HOOKUP program, the parameters and error assignments have already been described in chapter III. If a BC event has one or more tracks whose TVGP momentum are greater than 15 GeV/c and if the tracks in the corresponding SC frame are equal to or smaller than the BC prong number, a HOOKUP attempt is made. If the TVGP momentum value for the track is greater than the beam momentum or the momentum is negative, the momentum value is replaced by the beam momentum and the necessary azimuthal angle correction is made. Then HOOKUP is attempted. If there are 2 SC records for 1 or 2 BC events (alternating trigger), all possible combinations are tried and the best combination is used in later analysis. When the χ^2 of the direct matching (defined by equation 3-9 of chapter III) between the BC track and the SC track is less than 250, the HOOKUP fit is initiated. If the final HOOKUP χ^2 (defined by equation 3-10 of chapter III) is less than 25 and the momentum resolution $\Delta p/p$ is less than 0.50, the track is accepted as a good HOOKUP track. In that case the HOOKUP record is substituted for the TVGP record for that track. In addition, all HOOKUP information (106 words per HOOKUP track) is stored in BLOCK 5 of the TVGP output FORMAT. Thus the HOOKUP output record looks exactly like the TVGP output record. Therefore the kinematic fitting program SQUAW can be used with the HOOKUP data without any difficulty (APPENDIX A).

The SQUAW fit for HOOKUP events was performed under the same conditions that were used for the bare BC data analysis. The χ^2 distributions of all HOOKUP SQUAW events at the 2 energies are shown in Figures 4.7a, 4.7b, and 4.7c. Although the statistics of data are very limited, the peak of the distributions appear to be located in the normal position. The disposition of HOOKUP 4C events is given in Table 4.6.

Table 4.6. HOOKUP 4C events at 200-300 GeV/c.

n	$\chi^2 < 100$	$\chi^2 < 30$
2	239	208
4	120	70
6	105	55

The CM track distributions of HOOKUP 4C events at 200 and 300 GeV/c are shown in Figures 4.8a through 4.8f. The track distributions for HOOKUP 4 prong 4C events are not symmetric, but there are more tracks in the forward hemisphere. This indicates that the beam diffractive events are more frequently recorded by the Hybrid System than the target diffractive events. Of 70 4-pronged 4C events with χ^2 less than 30, 18 events have 1 forward to 3 backward division, 9 events have 2 to 2 division and 43 events (61%) have 3 forward to 1 back-

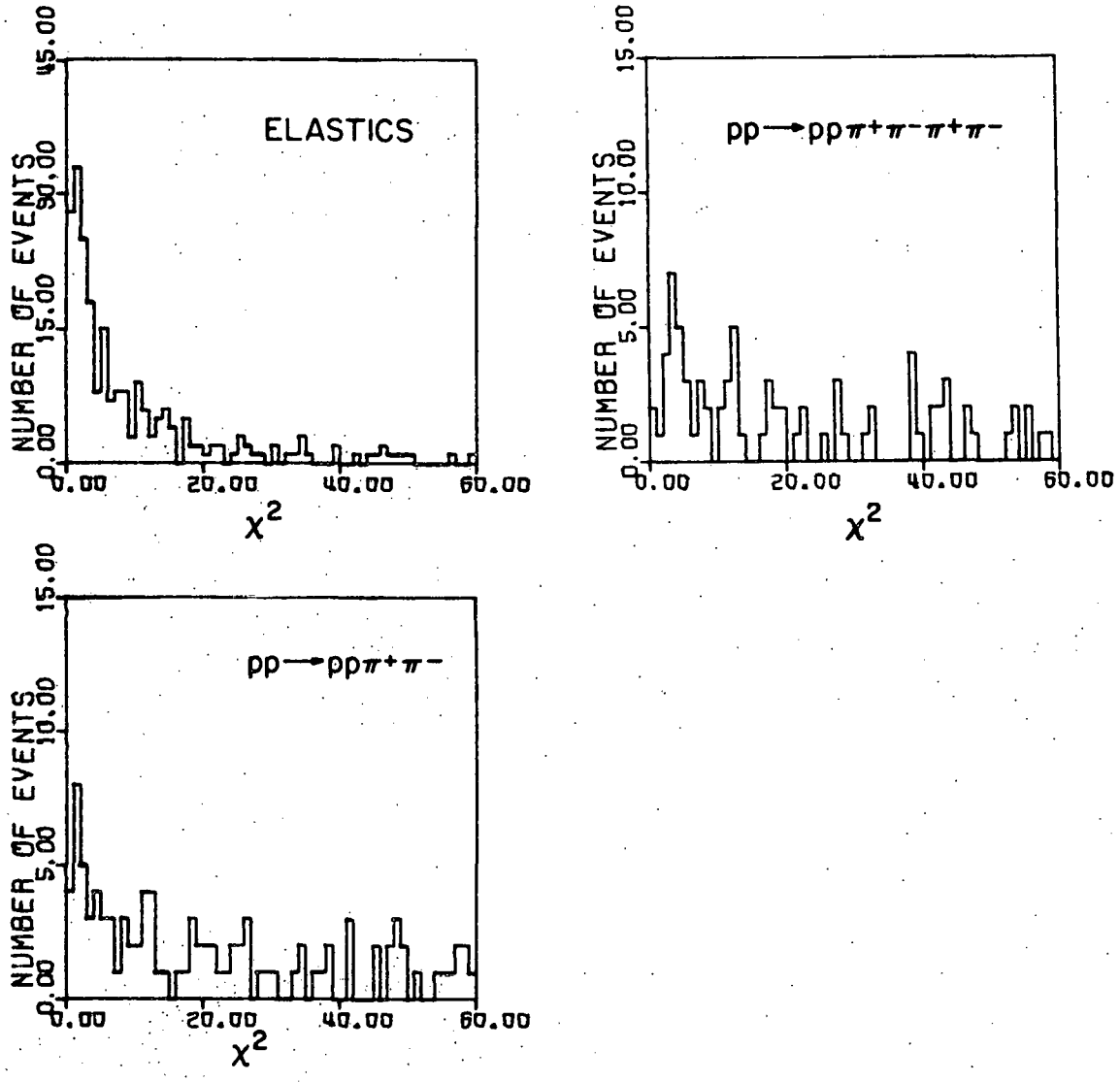

Figure 4.7. χ^2 distribution of SQUAW fitting; HOOKUP data at 200 and 300 GeV/c.

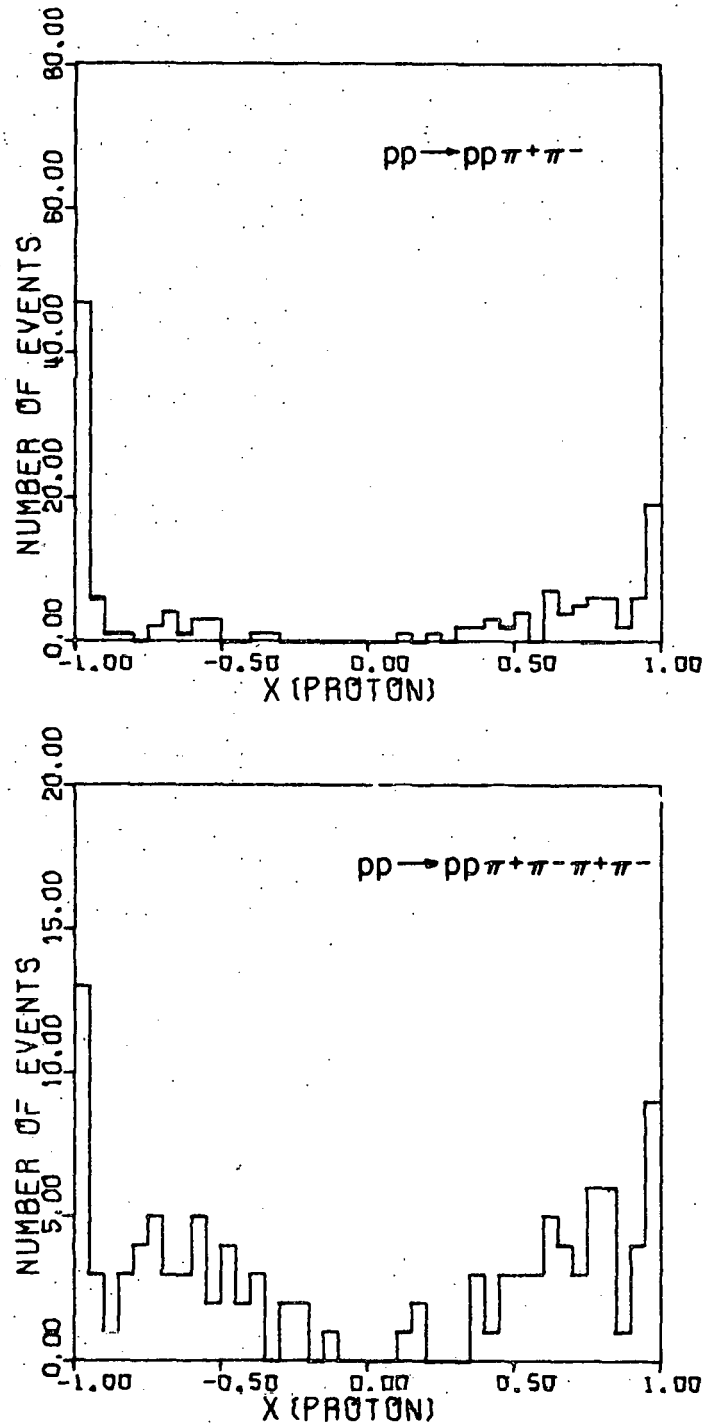

Figure 4.8. The distribution of the Feynman x variable; HOOKUP data only.

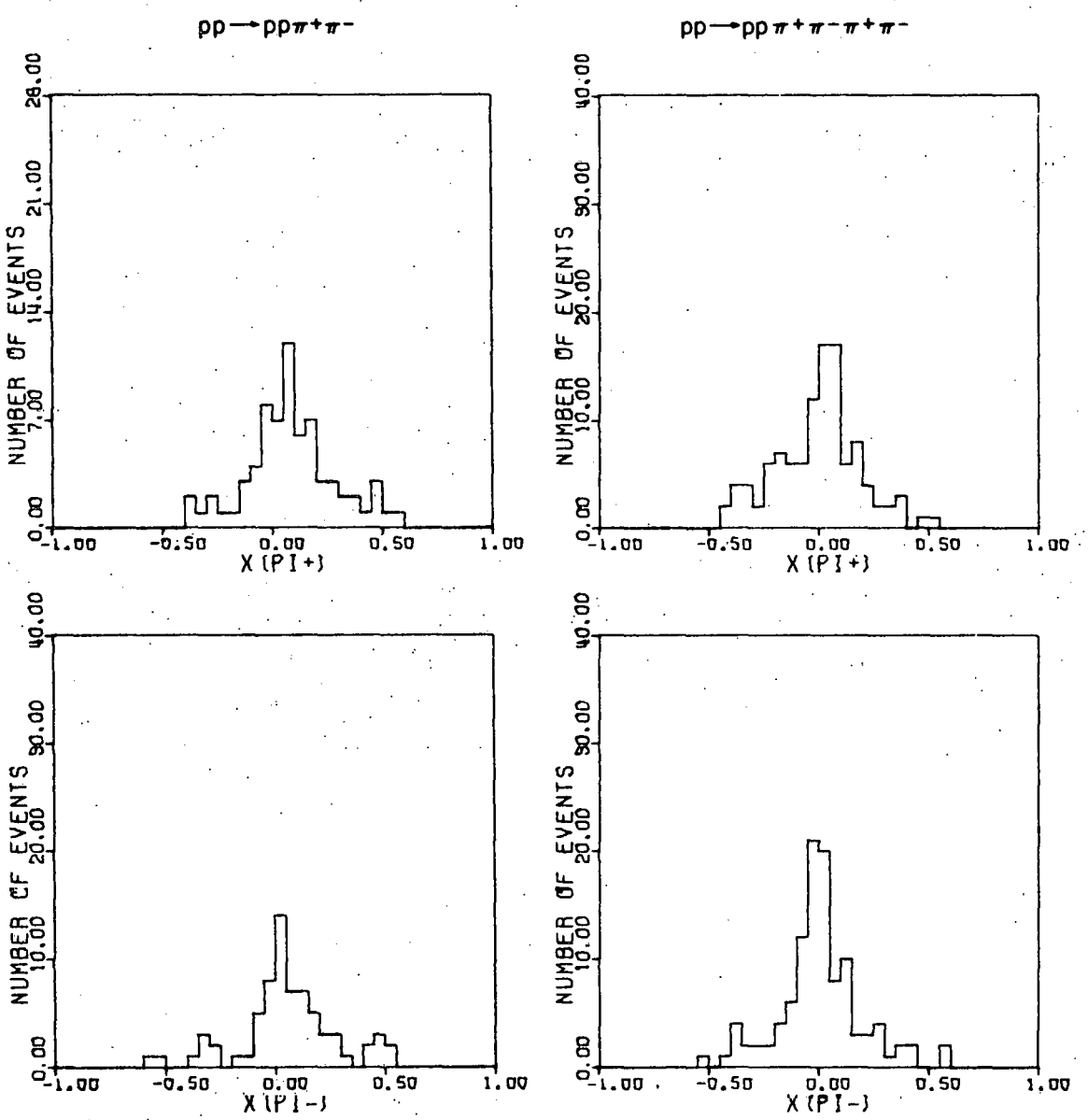

Figure 4.8. (Continued)

ward division. Another interesting feature is seen in the HOOKUP 6 pronged 4C events. Of 55 6-pronged 4C events with χ^2 less than 30, 21 events (42%) are such that the six tracks are divided 3 forward and 3 backward in the CM system. Of these, 12 events (22% of total events) have both effective masses for the 3 particle system ($p\pi^+\pi^-$) smaller than 3 GeV. This clearly indicates that the Experiment 2B Hybrid System is an exceedingly sensitive instrument for the detection of Double Diffraction events.

Figure 4.9 is the missing mass squared distribution for HOOKUP 4C events. The scatter plot of the momentum imbalance distributions for HOOKUP 4-pronged 4C events with a χ^2 cut of 30 is presented in Figure 4.10. For convenience in comparing this plot with those of the bare BC events (4.5a and 4.5b), the same scale is used. While the data points are scattered all over in the bare BC plots, most of the HOOKUP 4C events have the momentum imbalance within 200 MeV/c of zero. In general, the improvement from "bare bubble chamber measurement" to "hooked-up tracks" is obvious in any of the distributions presented in this section.

2. Comparison of bare BC 4C and HOOKUP 4C events

This part of the analysis is based upon the HOOKUP subsamples of 11 rolls of pp data at 300 GeV/c (ISU data); they comprise about 18% of the ISU bare BC 4-prongs and 23% of the ISU bare BC 6-prongs. The χ^2 distribution (defined by equa-

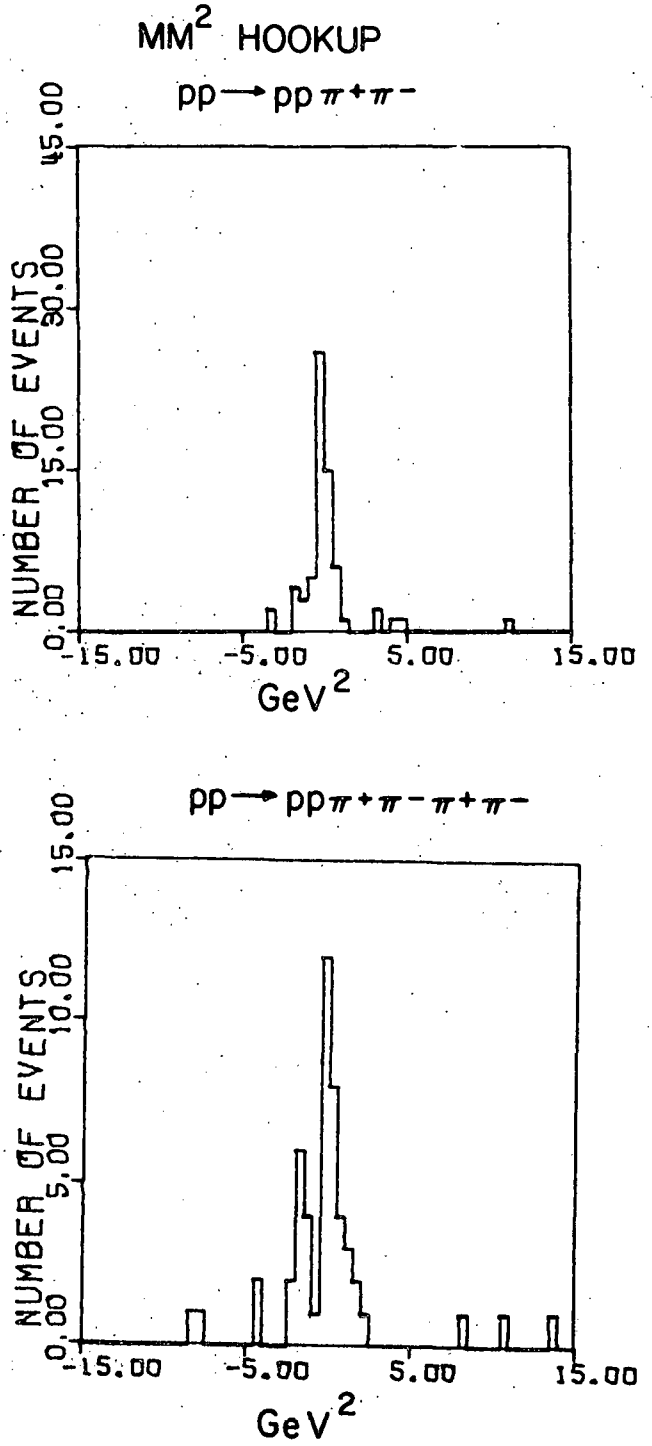

Figure 4.9. Missing-mass-squared (MM^2) distribution for $pp\,\pi^+\pi^-$ and $pp\,\pi^+\pi^-\pi^+\pi^-$ final states at 200 and 300 GeV/c; HOOKUP data only.

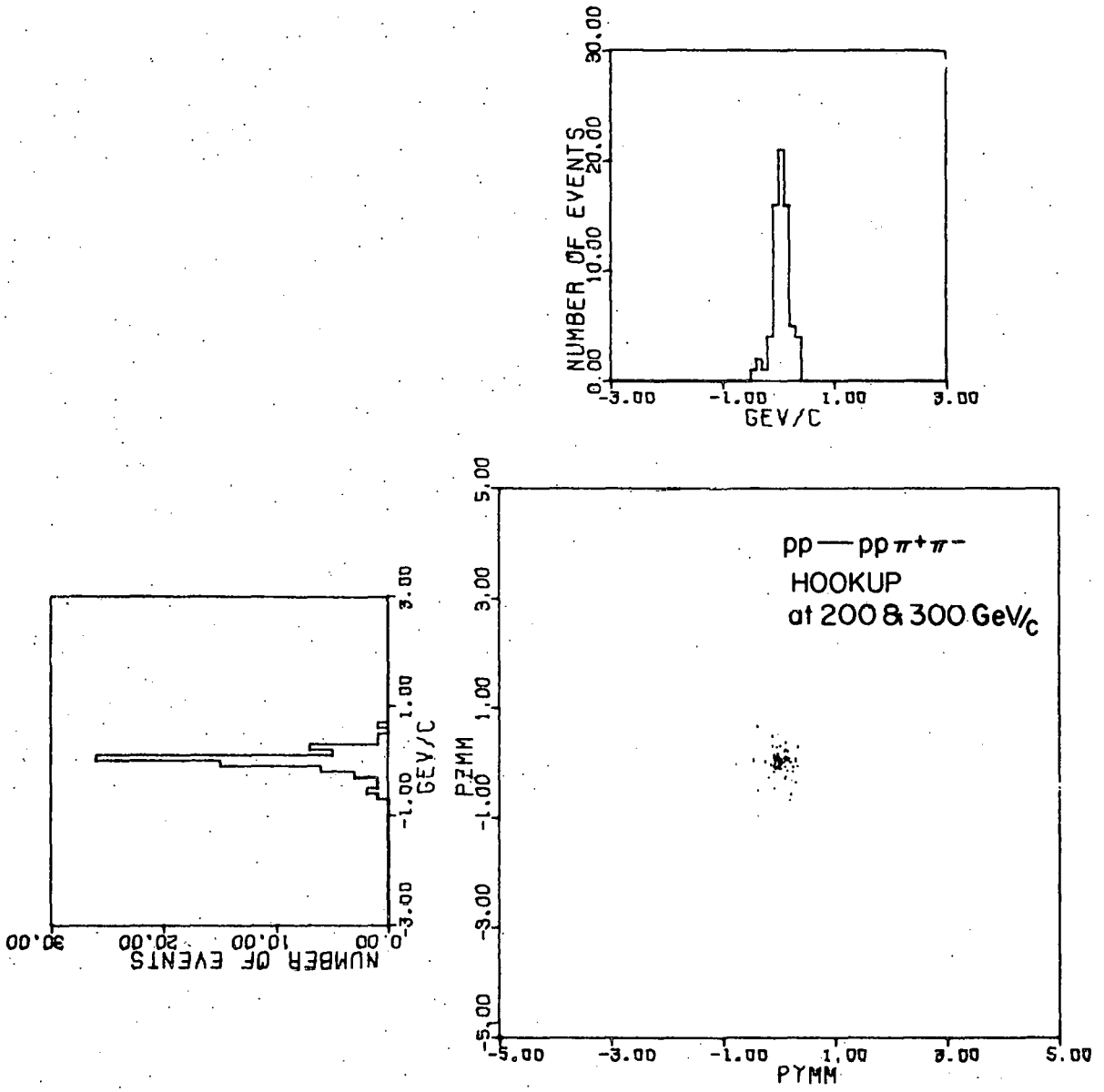

Figure 4.10. Scatter plot of the missing momenta in the plane perpendicular to the beam direction; HOOKUP data only.

tion 3-10 of chapter III) for HOOKUP tracks from this data set is shown in Figure 4.11. The arrows in the figure indicate two different cuts used in this analysis; namely HOOKUP track χ^2 cut of 25 and of 50. Every HOOKUP event has two fitting results from SQUAW: (1) SQUAW result without using SC information (SQ) and (2) result of SQUAW using SC information (HQ).

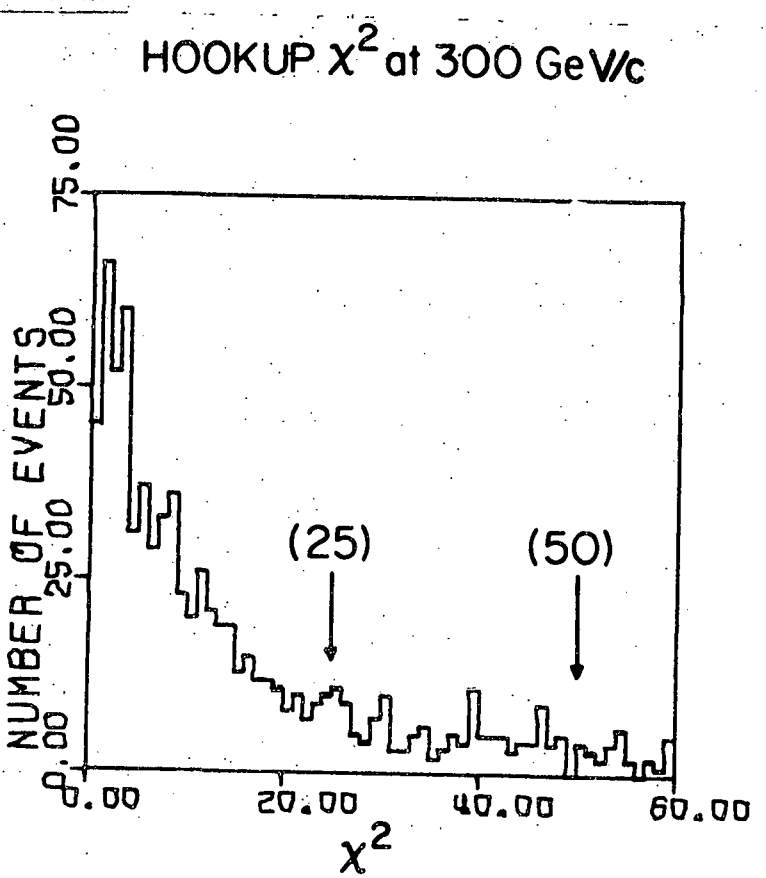

Figure 4.11. χ^2 of HOOKUP

Based on the assumption that HQ provides the best kinematic fit, the percentage of contamination from inelastic events and of the losses during the SQ fitting process can be

estimated using the fitting results of HQ and SQ for HOOKUP events. In the comparison between the HQ result and the SQ result, a strong condition is imposed on the data: that is, the fastest track in the TVGP record must be hooked up. If it is not hooked up, the pair of data, SQ and HQ is completely discarded. By making this restriction, together with the cut on total SC track number, the study of the effect of improved resolution on the kinematic fitting and the estimate of the background can be free from experimental bias. From the comparison between SQ and HQ, it is determined whether the kinematic fit was successful in:

(1) SQ only

(2) HQ only

(3) Both SQ and HQ.

The contamination from inelastic events in the bare BC 4C fits is estimated by

$$\frac{[\text{SQ only}]}{[\text{SQ only}] + [\text{Both SQ and HQ}]} \qquad (4\text{-}1)$$

The loss of real 4C events from the bare BC 4C fits is estimated by

$$\frac{[\text{HQ only}]}{[\text{SQ only}] + [\text{Both SQ and HQ}]} \qquad (4\text{-}2)$$

The comparison of SQ and HQ events is made for all events

whose SQUAW χ^2 are less than 100. No other cuts are applied to SQUAW samples. The results are summarized in the Table 4.7.

One can tentatively conclude from this result that the contamination of inelastic events is about 30% for the bare BC 4-pronged 4C events and is about 40% for the 6-pronged 4C events at 300 GeV/c. The losses are much smaller than the contamination. These are about 10% for 4-pronged 4C events and about 20% for 6-pronged 4C events at 300 GeV/c. It is remarkable that the contamination estimates are consistent with the trend of preliminary estimates made using the XMSQ cut (4-1), which is shown in Table 4.5. However, the estimate from the HOOKUP analysis is consistently lower than the estimates derived using the XMSQ cut (4-1). The estimates from the HOOKUP data analysis should be taken as lower limits of the background for the following two reasons:

(a) The χ^2 cut of 50 for HOOKUP tracks appears to be somewhat restrictive.

(b) A study of event vertex location indicates that the HOOKUP events correspond to relatively well-measured bare BC events.

Therefore the magnitude of real contamination is somewhere between the estimate using the XMSQ cut (4-1) and the estimate using the HOOKUP data. Thus the contamination is estimated to be between 30% and 40% for 300 GeV/c 4-pronged 4C events. It is about 50% for 6-pronged 4C events at 300 GeV/c.

Table 4.7. Background study.

n	HOOKUP χ^2 Cut	# of EVENTS	SQ ONLY	HQ ONLY	BOTH χ^2(HQ) Better	BOTH χ^2(SQ) Better	Estimate of Contamination	Estimate of Losses
4	25	135	10	4	15	20	0.22 ± 0.08	0.09 ± 0.05
6	25	181	14	6	11	11	0.39 ± 0.12	0.17 ± 0.07
4	50	158	15	4	18	22	0.27 ± 0.08	0.07 ± 0.04
6	50	203	17	8	14	13	0.39 ± 0.11	0.18 ± 0.07

It is also reasonable to assume that the magnitude of the background has an energy dependence similar to the contamination rate estimated using the XMSQ cut, which is shown in Table 4.5. Thus the background at 200 GeV/c is expected to be lower by 5 to 10% in each channel than the corresponding value at 300 GeV/c.

V. EXPERIMENTAL RESULTS

The results to be presented in this chapter are based on the data from Iowa State University, Michigan State University, Argonne National Laboratory and Fermi National Accelerator Laboratory. Analysis comparable to the present results are found in a review by J. Whitmore on recent results using the Fermilab 30-inch Hydrogen Bubble Chamber (15). The primary purpose of the present investigation is to study the behavior of exchanged particles, especially the pomeron in pp interactions between 200 and 300 GeV/c. According to Regge Pole Theory, the strong interactions are dominated by the exchange, between the incident hadrons, of groups of resonance states, which are usually called Regge Poles or Regge Trajectories. A unique concept in Regge Theory is pomeron exchange, which is really a vacuum exchange between 2 particles. If this idea is accepted then as the energy increases it is expected that:

a. The total cross sections become constant.

b. The diffraction peak in elastic scattering shrinks.

c. The polarization goes to zero.

The presently available experimental data are apparently consistent with these predictions. Thus it is of great interest to search for further experimental evidence of Regge Pole behavior of the pomeron at Fermilab energies; for example, pomeron factorization and multiple pomeron exchange processes.

A. Cross Sections

The differential cross section in a Regge Pole model has the following energy dependence:

$$\frac{d\sigma}{dt} = A(t)S^{2\alpha(t)-2} \tag{5-1}$$

where S is the square of the center of mass energy, $\alpha(t)$ is the complex angular momentum and t is the square of the invariant momentum transfer. The relation (5-1) was compared with the experimental energy dependence of total inelastic two-body cross sections by D. R. O. Morrison (16). He found the experimental energy dependence of the form:

$$\sigma_{tot} \propto P_{in}^{-n} \tag{5-2}$$

where P_{in} is the incident beam momentum. At high energy, S is directly proportional to P_{in} and the small t region gives most of the total cross section, so that Morrison concluded that the exponent n in (5-2) is approximately equal to:

$$n \simeq 2 - 2\alpha(0). \tag{5-3}$$

In this interpretation, the energy dependence of the cross section is controlled by which trajectories are exchanged. For pomeron exchange, $\alpha(0)$ is approximately one so that the exponent n in (5-2) is zero. Thus the processes induced by pomeron exchange are expected to have constant cross sections

for different energies. Reactions that proceed by meson exchange have a nonzero exponent. For the ρ trajectory, $\alpha(0)$ is about $\frac{1}{2}$, so that for these processes n is one. For π exchange, n is expected to be about two. Therefore, the contribution from meson exchange decreases as the energy increases. Consequently, the two body inelastic processes are expected to be dominated by pomeron exchange at very high energy. A more exact and general approach to the problem is briefly described next. If the trajectory $\alpha(t)$ and $\ell n\ A(t)$ in equation (5-1) are linear functions of t for the small t region, then

$$\ell n\ A(t) \simeq A_0 + A_1(t)$$

and

$$\alpha(t) \simeq \alpha_0 + \alpha_1(t). \tag{5-4}$$

Therefore equation (5-1) can be rewritten as

$$\frac{d\sigma}{dt} = [A(0)S^{2\alpha(0)-2}]e^{(A_1 + 2\alpha_1 \ell n\, S)t}\ . \tag{5-5}$$

Integrating (5-5) over the entire t region, one obtains:

$$\sigma_{tot} \propto S^{2\alpha(0)-2}/\ell n\, S\ . \tag{5-6}$$

This indicates that pure pomeron exchange does not give a constant cross section. However in the region of S where

only pomeron exchange is important, the decrease in the cross-section with increasing energy should be slow, i.e. $\sim (\ell n\, S)^{-1}$. If the multiparticle exclusive reactions to be studied in this dissertation are mostly diffractive processes induced by pomeron exchange, the energy dependence of the cross sections should be comparable with the features discussed above.

In the present experiment, there are two ways to obtain the cross sections for $pp\pi^+\pi^-$ final state and $pp\pi^+\pi^-\pi^+\pi^-$ final state:

Method 1. Use bare BC data only.

Method 2. Use bare BC data and HOOKUP data.

Both methods start from the 4C events with $\chi^2 < 30$ from bare BC. Method 1 uses primarily the XMSQ cut to calculate the cross sections. As discussed in chapter IV, the background estimate from the XMSQ cut of (4-1) would give an upper limit for inelastic contamination. Thus the use of method 1 would possibly provide lower cross sections than the real values. It is important to use the cleanest data samples available in the experiment when one studies such a debatable subject as Double Pomeron Exchange. Therefore, the final data samples for physics analysis were selected by using the XMSQ cut in method 1 in addition to the χ^2 cut of 30, even though the corresponding cross sections for those events are expected to be lower than the real values. The

precise cut on XMSQ used in method 1 varies slightly for different particle configuration in the CM frame; however, it is not drastically different from the cut (4-1). The cross sections determined by method 1 are given in Table 5.1a. The 4C events shown in the column '4C corrected' are obtained using the XMSQ cut. These events are used to discuss the physics of multiparticle exclusive reactions. For the $pp\pi^+\pi^-$ final state, the statistics of the data in the present experiment (541 events at 200-300 GeV/c) are higher than those of any previous report at very high energies (123 events in Reference 6 and 191 events in Reference 7). The cross sections presented in the last column do not include the corrections for the events lost during the kinematic fitting process. This exclusion of the estimated lost events in the cross section calculation by method 1 was done intentionally in order to compare the results with those of the ANL experiment (7), in which the authors concluded that there were no such losses of events. The ANL group in their 200 GeV/c pp experiment reported a cross section of 680 ± 140 μb for the $pp\pi^+\pi^-$ final state, which is in good agreement with 690 ± 50 μb from the present experiment at 200 GeV/c using method 1.

Now that it is confirmed that the technique of bare BC data analysis of the present experiment is consistent with the previous experiment by the ANL group (7), we shall

Table 5.1a. Cross sections estimated by method 1.[a]

Beam	Final State	Number of Events Used	4C χ^2 Cut[b]	4C Corrected[c]	$\sigma \pm \delta\sigma$[d] (mb)
200 GeV/c pp	pp	3841	2331	2953	6.60 ± 0.30
	$pp\pi^+\pi^-$	2652	427	305	0.690 ± 0.050
	$pp\pi^+\pi^-\pi^+\pi^-$	2591	213	123	0.313 ± 0.031
300 GeV/c pp	pp	2851	1947	2384	7.19 ± 0.22
	$pp\pi^+\pi^-$	2053	401	236	0.620 ± 0.043
	$pp\pi^+\pi^-\pi^+\pi^-$	2151	251	115	0.306 ± 0.030

[a]The topological cross sections determined by Experiment 2B are used (Table 2.1 and 2.2).

[b]χ^2 cut was 50 for elastics and 30 for other final state.

[c]Only a low t correction was made for elastic events. The averaged slope value of the elastic events for the t region between 0.06 and 0.30 $(GeV/c)^2$ is (10.0 ± 0.5) $(GeV/c)^{-2}$ at 200 and 300 GeV/c. The corrections for other final states are from XMSQ cut only and do not contain the correction for losses.

[d]The errors included are the statistical errors and the uncertainty associated with normalization to the topological cross sections. The corrections for lost events are not included in the cross sections and error estimates for $pp\pi^+\pi^-$ and $pp\pi^+\pi^-\pi^+\pi^-$ final states.

examine how accurate the bare BC analysis itself is. For this study, method 2 mentioned earlier is used; namely, one compares, for the same event, the bare BC result with the HOOKUP result. The contamination and the losses of events for 4C channels with $\chi^2 < 30$ are estimated from the results presented in Table 4.7 in chapter IV. Although the detailed study of the background was done in chapter IV using HOOKUP data at 300 GeV/c only, it is assumed that the background has the same energy dependence as indicated by the XMSQ distributions shown in Figure 4.6. The cross sections determined by method 2 are given in Table 5.1b. If one assumes that HOOKUP data provides the best result of kinematic fitting, it is evident in Table 5.1a and 5.1b that the bare BC analysis significantly underestimates the cross sections for the channels $pp\pi^+\pi^-$ and $pp\pi^+\pi^-\pi^+\pi^-$. It is also clear that the discrepancy between Table 5.1a and Table 5.1b arises from the difference in the background estimate between the two methods. The energy dependence of the cross sections determined by method 2 is shown in Figure 5.1 for $pp \rightarrow pp\pi^+\pi^-$ channel and in Figure 5.2 for $pp \rightarrow pp\pi^+\pi^-\pi^+\pi^-$ channel. It is striking that the cross sections for the $pp\pi^+\pi^-$ final state is seen to level off. It also appears that the cross section at 69 GeV/c (6) is low when compared to the present data. This may be attributed to either the statistics of data (123 events)

Table 5.1b. Cross Sections estimated by method 2.[a]

Beam	Final State	Number of Events Used	4C $\chi^2 < 30$	Contamination	Losses	4C Corrected	$\sigma \pm \delta\sigma$[b] (mb)
200 GeV/c	$pp\pi^+\pi^-$	2652	427	51 ± 17	0	376 ± 27	0.856 ± 0.077
p	$pp\pi^+\pi^-\pi^+\pi^-$	2591	213	51 ± 15	28 ± 11	190 ± 24	0.484 ± 0.069
300 GeV/c	$pp\pi^+\pi^-$	2053	401	108 ± 32	28 ± 16	321 ± 41	0.849 ± 0.111
p	$pp\pi^+\pi^-\pi^+\pi^-$	2151	251	98 ± 28	45 ± 18	198 ± 37	0.527 ± 0.100

[a]The topological cross sections determined by Experiment 2B are used (Table 2.1 and 2.2).

[b]The errors included are statistical errors, the uncertainty associated with normalization to the topological cross sections and the uncertainties in the estimates of contamination and losses.

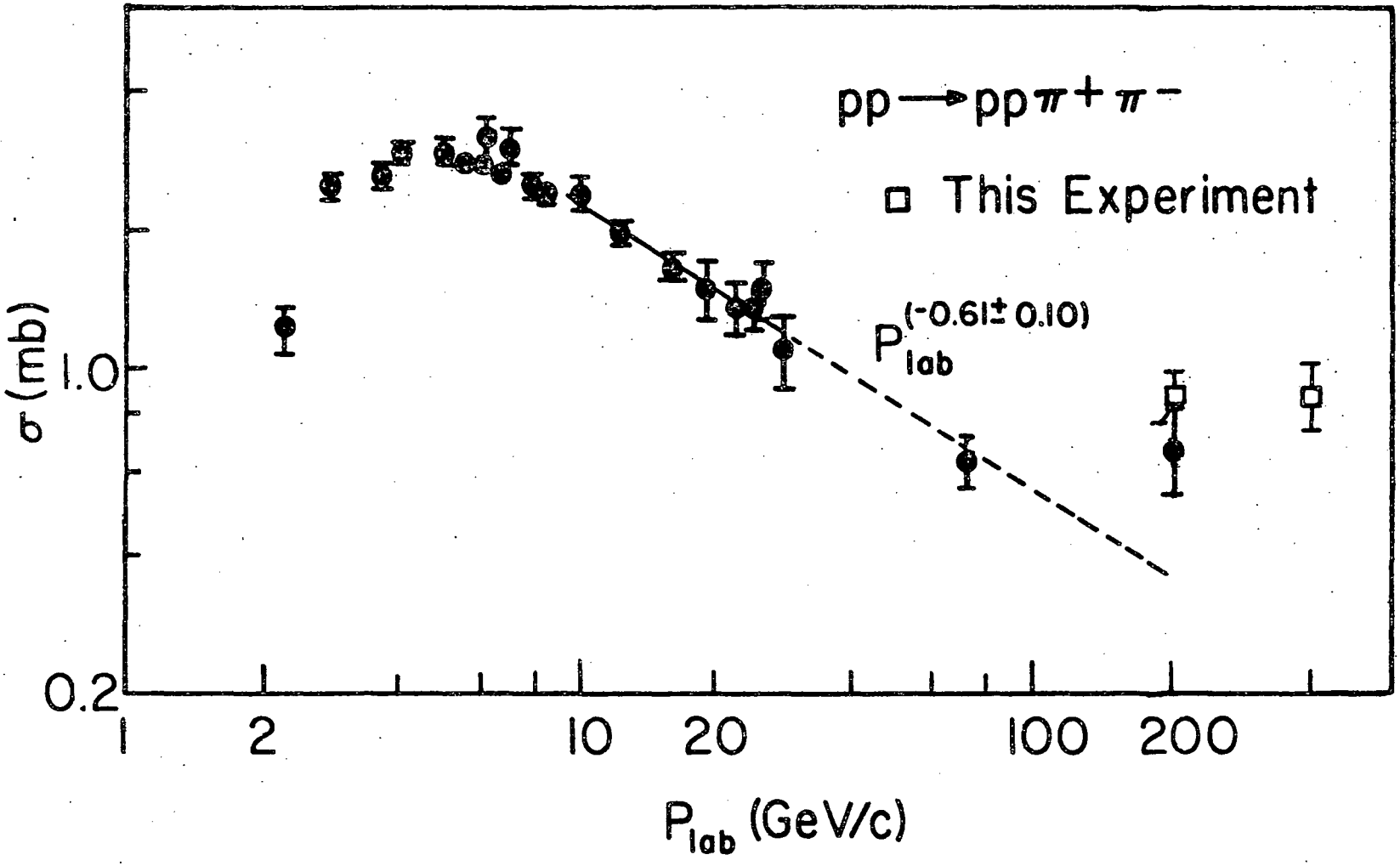

Figure 5.1. Summary of the production cross sections for the reaction pp → pp $\pi^+\pi^-$.

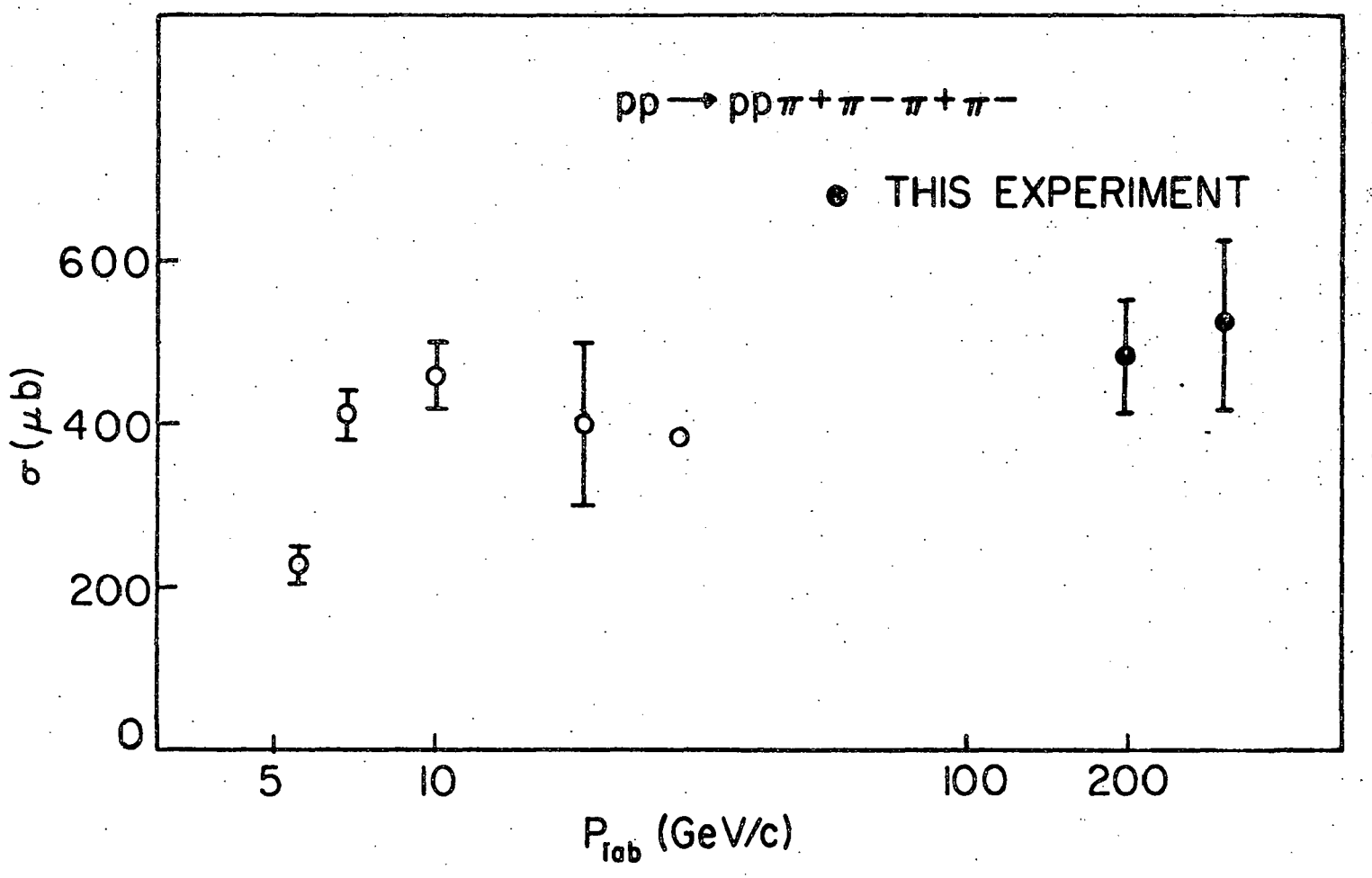

Figure 5.2. Summary of the production cross sections for the reaction pp → pp $\pi^+\pi^-\pi^+\pi^-$.

or to the method of analysis: no kinematic fits were tried in this bare BC work by the French-Russian collaboration. As shown in Figure 5.2, the cross section for the $pp\pi^+\pi^-\pi^+\pi^-$ final state also changes very little over a wide energy range. It should be noted that no error is assigned to the data point at 28.5 GeV/c and therefore this point should not be considered seriously. The results shown in Figures 5.1 and 5.2 strongly suggest pomeron dominance for these reactions at Fermilab energies. It is also possible to interpret the energy dependence of cross sections from a statistical model (17).

The above results from the present experiment raise a serious question concerning the usefullness of SQUAW kinematic fitting using bare BC data only for the absolute determination of cross sections at Fermilab energies. It was tacitly assumed in our bare BC analysis that the losses of real 4C events during the kinematic fitting processes could be ignored. There is conclusive evidence in the present experiment that the losses cannot be disregarded and that the contamination of inelastic events is overestimated if one studies the missing mass squared distributions only. The results of the present experiment indicate that the bare BC analysis using the kinematic SQUAW fitting is incapable of determining the production cross sections of exclusive reactions properly at the

Fermilab energies. Throughout the rest of this chapter, the bare BC analysis will be adopted to discuss the physics in the multiparticle exclusive reactions at 200 and 300 GeV/c, but the cross section is increased in each channel by the scale factor obtained from Tables 5.1a and 5.1b.

B. Single Diffractive Dissociation

The characteristic features of a low mass enhancement in the $p\pi^+\pi^-$ system from the $pp\pi^+\pi^-$ final state are presented in this section, which consists of four sub-sections: Mass Distributions, Δ^{++} Production, Helicity Conservation and Spin of N^*.

Mass Distributions

Figure 5.3a and 5.3b show the mass of the $p\pi^+\pi^-$ system in the $pp\pi^+\pi^-$ final state. Of two possible combinations for $p\pi^+\pi^-$ system, the smallest $M(p\cdot\pi^+\cdot\pi^-)$ represents one data point in the figure. The formation of low mass states in this system is evident both at 200 and 300 GeV/c. The present statistical level prevents further study of fine structure in this low mass region. The feature of single diffractive dissociation in the $pp\pi^+\pi^-$ final state is more sharply displayed in the scatter plots of $M(p_s\cdot\pi^+\cdot\pi^-)$ with respect to $M(p_f\cdot\pi^+\cdot\pi^-)$: Figure 5.4 (200 GeV/c) and Figure 5.5 (300 GeV/c) show that the majority of events are associated with either target or beam diffractive dissociation.

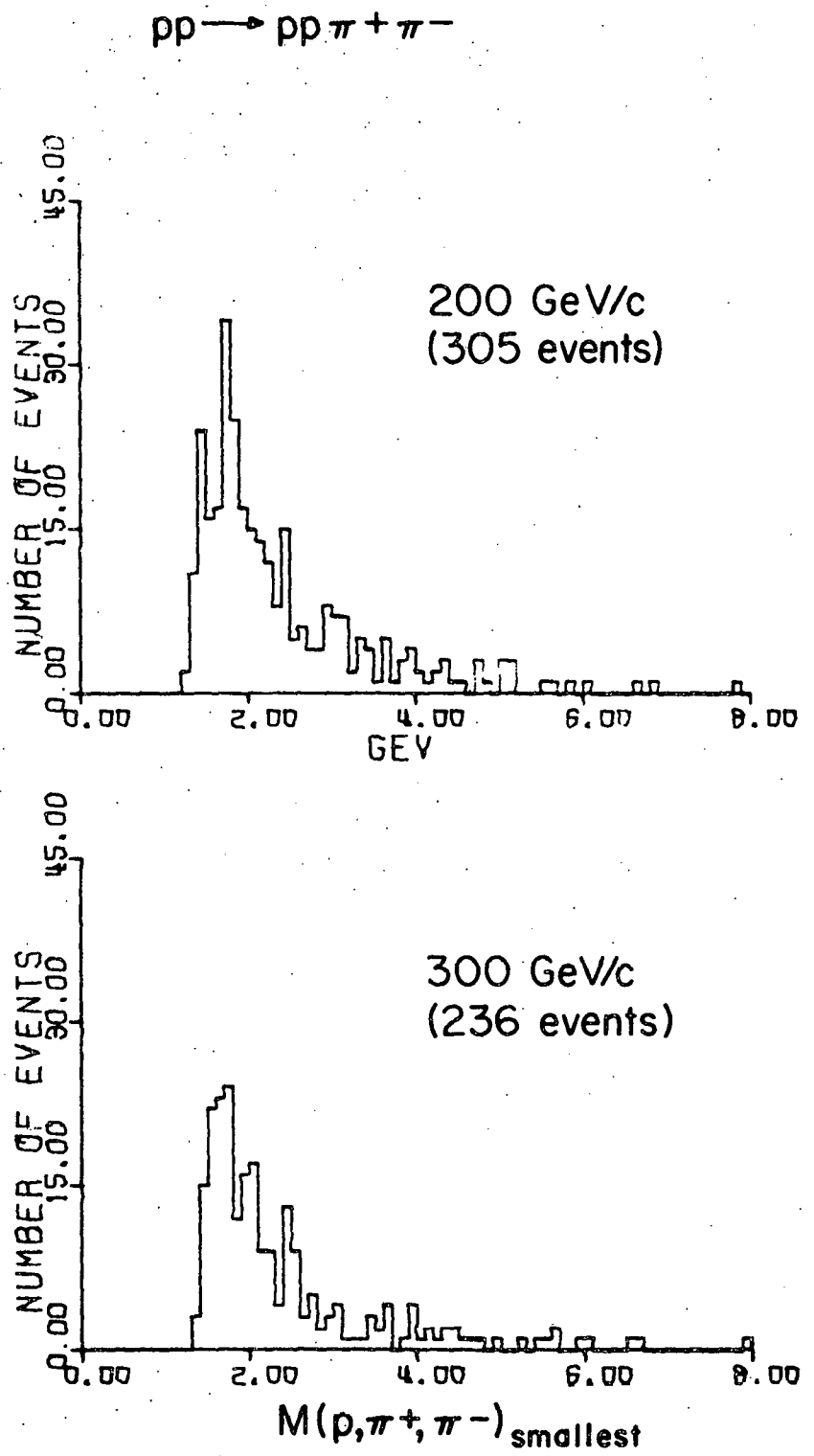

Figure 5.3. The effective-mass distribution of the $p\pi^+\pi^-$ system. The smallest combination is selected in each event.

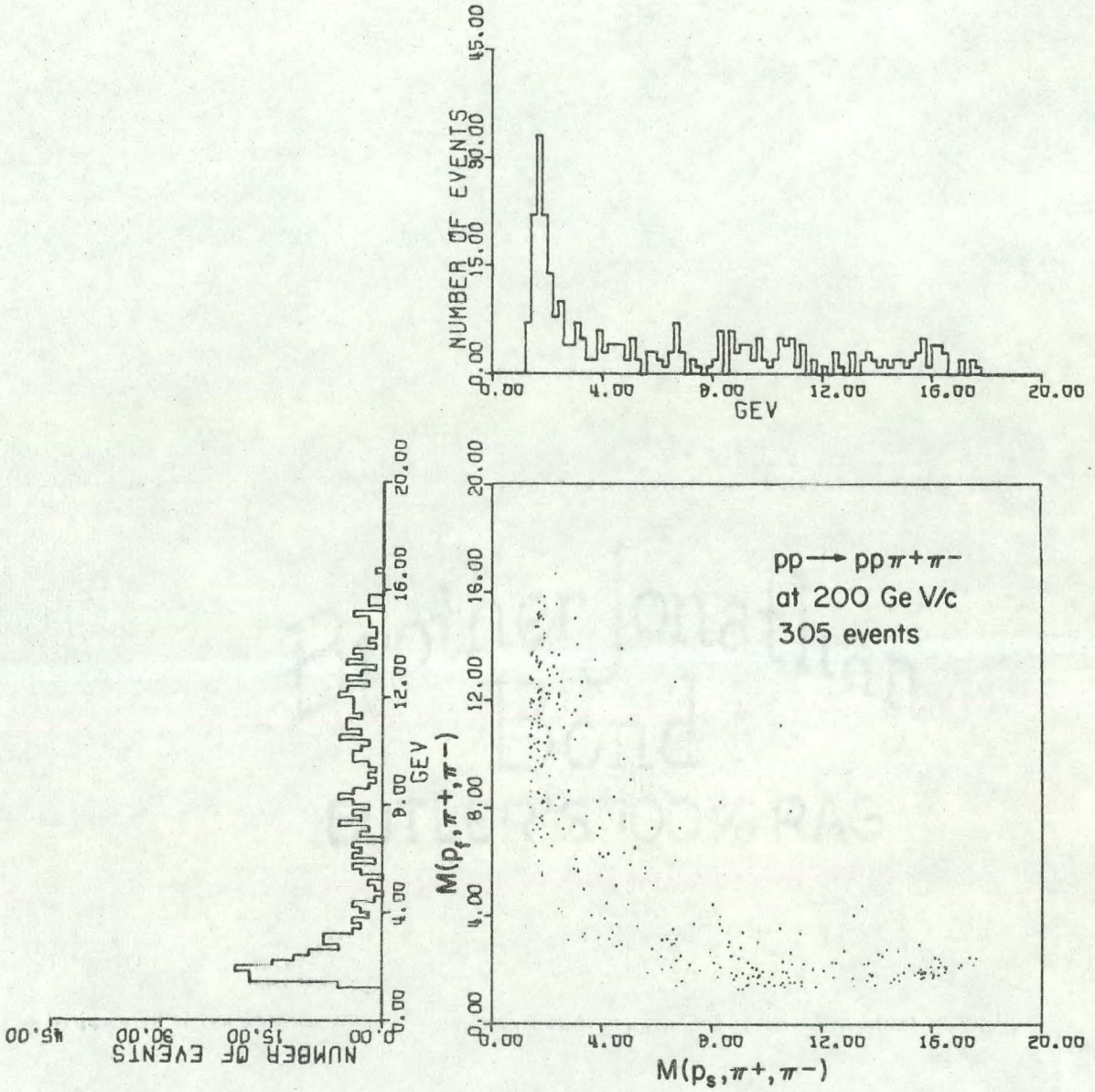

Figure 5.4. The scatter plot of the effective mass $M(p_s, \pi^+, \pi^-)$ with respect to $M(p_f, \pi^+, \pi^-)$.

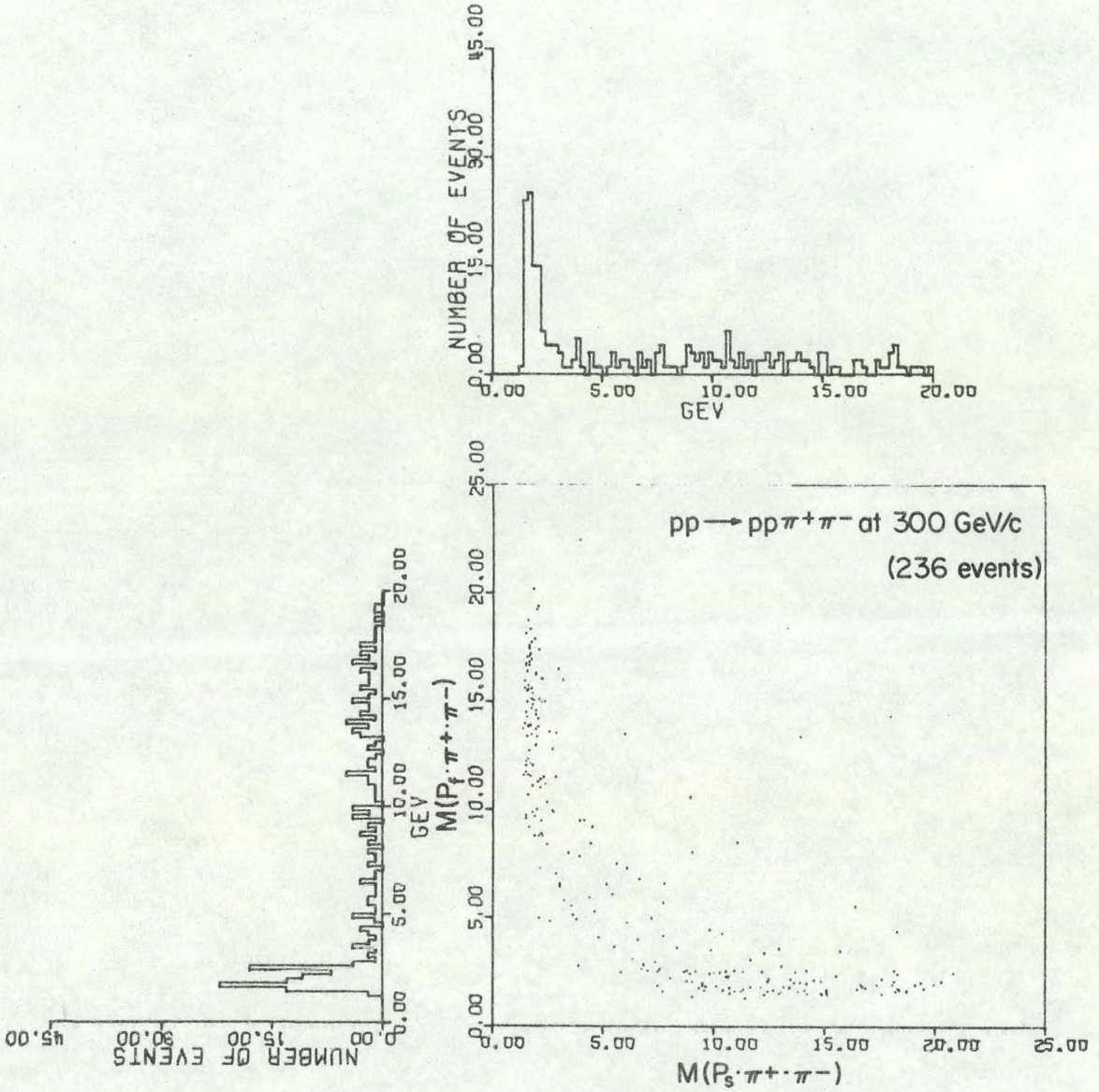

Figure 5.5. The scatter plot of the effective mass $M(p_s \cdot \pi^+ \cdot \pi^-)$ with respect to $M(p_f \cdot \pi^+ \cdot \pi^-)$.

Δ^{++} Production

In inclusive experiments at Fermilab energy, strong $\Delta^{++}(1236)$ production was observed (18). Subsequent investigations revealed that the inclusive Δ^{++} production cross section is independent of energy (19) and that Δ^{++} is a decay product of a diffractively excited state (20). Therefore, in the $pp\pi^+\pi^-$ final state of the present experiment, Δ^{++} production is expected in the following decay channel:

$$\begin{array}{l} pp \rightarrow N^* p \\ \qquad\quad \big\lfloor\!\rightarrow \Delta^{++}\pi^- \\ \qquad\qquad\quad \big\lfloor\!\rightarrow p\,\pi^+ \end{array} \qquad (5\text{-}7)$$

It is also possible to have Δ° production in this channel:

$$\begin{array}{l} pp \rightarrow N^* p \\ \qquad\quad \big\lfloor\!\rightarrow \Delta^\circ\pi^+ \\ \qquad\qquad\quad \big\lfloor\!\rightarrow p\,\pi^- \end{array} \qquad (5\text{-}8)$$

Assuming that the isospin of N^* is $\frac{1}{2}$, the production ratio between (5-7) and (5-8) is 9 to 1. However, both $p\pi^+$ and $p\pi^-$ combinations associated with N^* are kinematically constrained to have masses inside the Δ mass region, so that it is not meaningful to try to estimate the experimental production

rate for Δ^{++} and Δ° using just a mass cut. We shall discuss here only the general trend of the data. Shown in Figure 5.6 are: (1) $M(p\cdot\pi^{+}\cdot\pi^{-})_{smallest}$ at 200 and 300 GeV/c in Figure 5.6a, (2) the mass of $p\pi^{+}$ from N^{*} in Figure 5.6b and (3) the mass of $p\pi^{-}$ from N^{*} in Figure 5.6c. It is clear from the figures that Δ^{++} is a more dominant intermediate state than Δ°. The cross section for production of $\Delta^{++}(1236)$ over all the t region is presented in Table 5.2. The following cuts were imposed to obtain the cross sections:

1. N^{*} Mass < 3 GeV
2. $p\pi^{+}$ combination from N^{*} must have a mass in the range 1.12 GeV < $M(p\pi^{+})$ < 1.32 GeV.

The results strongly indicate constant Δ^{++} production between 200 and 300 GeV/c.

Table 5.2. Δ^{++} production in the final state $pp\pi^{+}\pi^{-}$.

	200 GeV/c	300 GeV/c
$pp \rightarrow pp\pi^{+}\pi^{-}$	305	236
Δ^{++} events	115	97
$\sigma_{\Delta^{++}}$(mb)	0.323 ± 0.046	0.349 ± 0.062

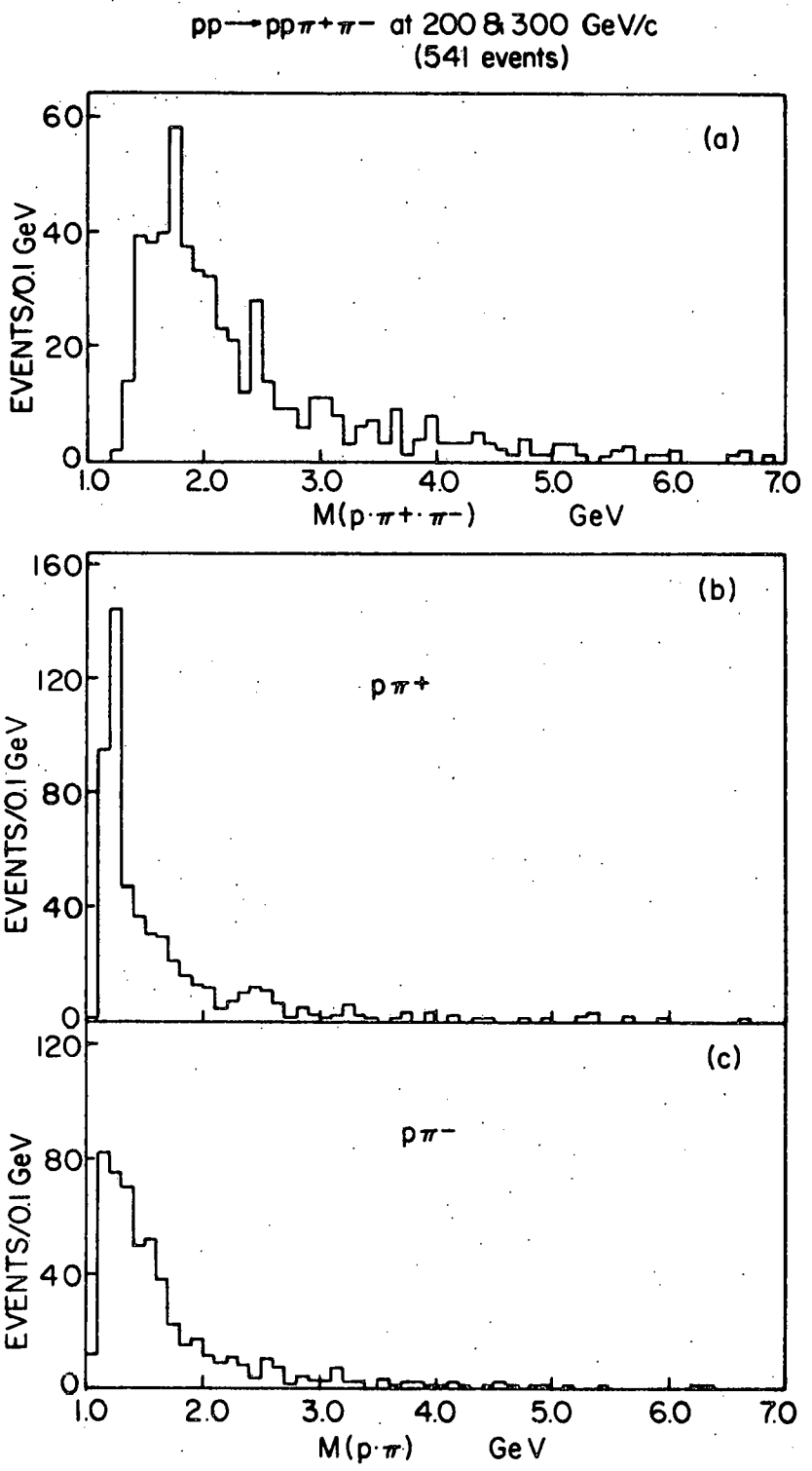

Figure 5.6. The distributions of (a) $M(p\cdot\pi^+\cdot\pi^-)_{\text{smallest}}$, (b) $M(p\cdot\pi^+)$, and (c) $M(p\cdot\pi^-)$.

Helicity Conservation

The nature of the low mass enhancement is not completely understood and therefore the interpretation of either helicity conservation or non-conservation for the low mass $p\pi^+\pi^-$ system is obscure (21). Despite this problem, the subject is briefly discussed below. Helicity conservation can be studied in two different frames: the Gottfried-Jackson Frame (N^* rest frame - T channel) and the Helicity Frame (S channel). Both frames are right-handed coordinate systems in which the Z axis is defined as shown in Figures 5.7 and 5.8 and Y axis is chosen along the normal to the production plane. Helicity conservation holds if the azimuthal angular distribution of the outgoing particles in a particular frame is isotropic. Figure 5.9 displays the azimuthal angular distributions for the proton, the Δ^{++} and the vector normal to the plane of the $(p\cdot\pi^+\cdot\pi^-)$ system in the T and S channels. (Note that the horizontal scale is different in the 2 sets of plots.) Isotropy is well satisfied in the T-channel: $\chi^2/DF = 1.88$ for proton, 0.82 for Δ^{++} and 0.55 for the normal to $(p\cdot\pi^+\cdot\pi^-)$ system. However, in the S channel, the proton distribution shows anisotropy ($\chi^2/DF = 2.74$). The other results are: $\chi^2/DF = 0.92$ for Δ^{++} and 1.69 for the normal to $(p\cdot\pi^+\cdot\pi^-)$ system in the S-channel. The data in both channels appear to be consistent with helicity conservation except for the proton distribution in S-channel. This result is in contrast to the previous

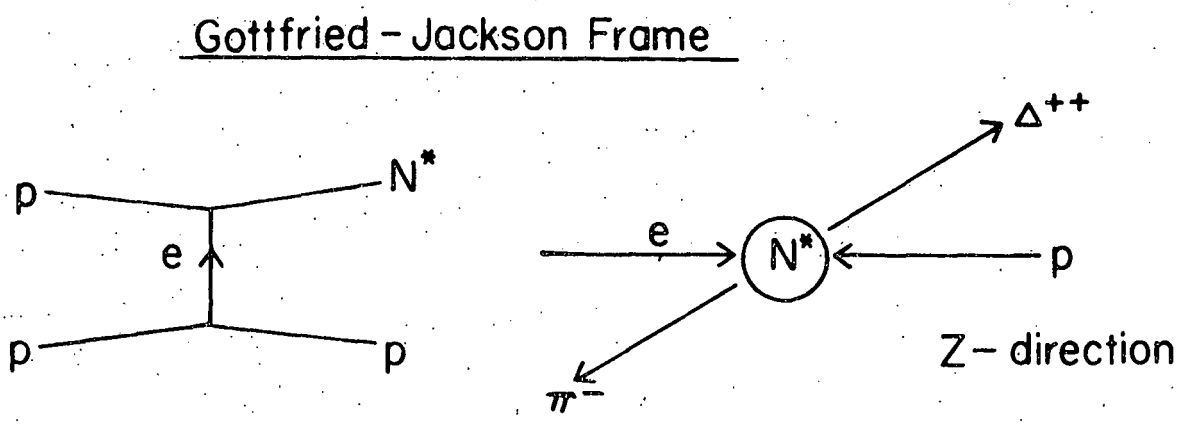

Figure 5.7. Gottfried-Jackson frame.

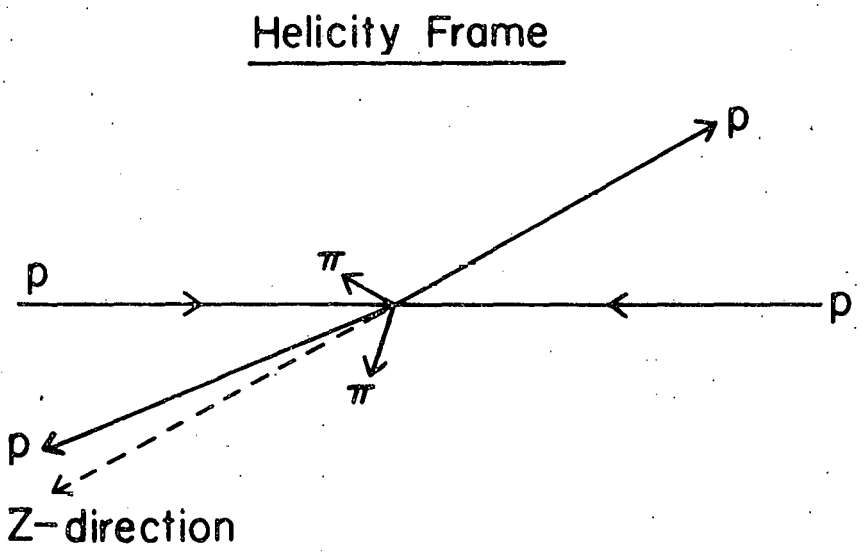

Figure 5.8. Helicity frame.

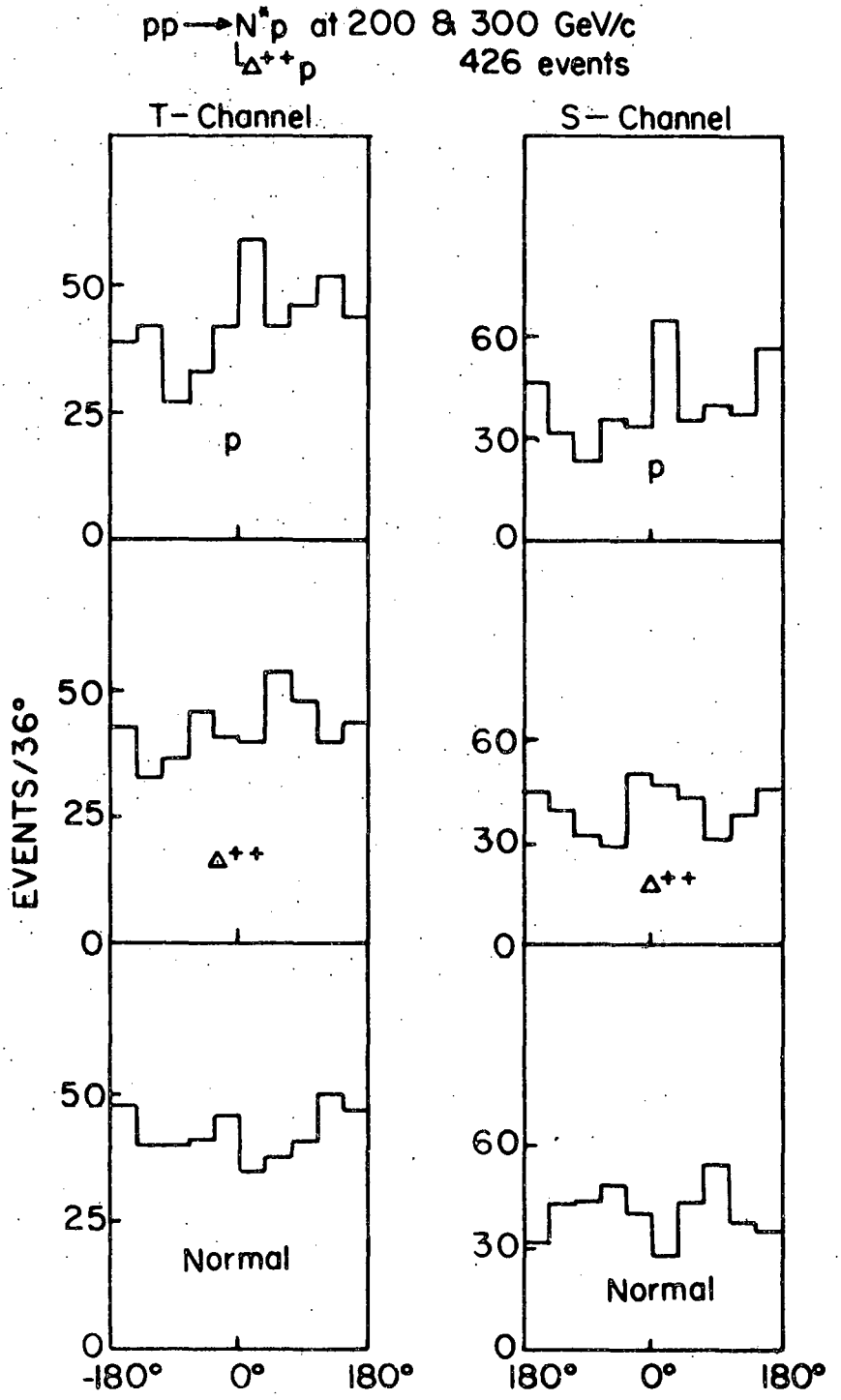

Figure 5.9. Azimuthal-decay angular distribution in the T-channel and S-channel coordinate systems.

measurement by the ANL group (7), where $\chi^2/DF = 3.21$ for the proton and 2.99 for Δ^{++} in the S-channel; $\chi^2/DF = 1.79$ for normal, 1.30 for proton and 0.91 for Δ^{++} in the T-channel. The conclusion of Reference 7 is that T-channel helicity is conserved.

Spin of N^*

It has been known that the Gribov-Morrison spin parity rule holds in inelastic diffractive scattering; namely

$$p_f = p_i(-1)^{J_f - J_i} \tag{5-9}$$

which simply states that higher spin states are allowed for N^*. A detailed study of the spin assignment for the $p\pi^+\pi^-$ enhancement in pp interactions was made by the Iowa State group at 22 GeV/c (22) and by J. G. Rushbrooke et al. (23) at 16 GeV/c. The conclusion of their work is that spin ½ is required for the 1450 MeV enhancement and spin-parity series $\frac{3}{2}^-$, $\frac{5}{2}^+$, $\frac{7}{2}^-$ for the 1700 MeV enhancement. The effect of spin is seen in the polar angular distribution of the normal to the decay plane in the N^* rest frame. Shown in Figure 5.10 are the data from the present experiment at 200 and 300 GeV/c with three different mass cuts. The distribution for the "1450" region is consistent with isotropy, which suggests spin ½. The other figures indicate the existence of higher spin states in the higher mass regions.

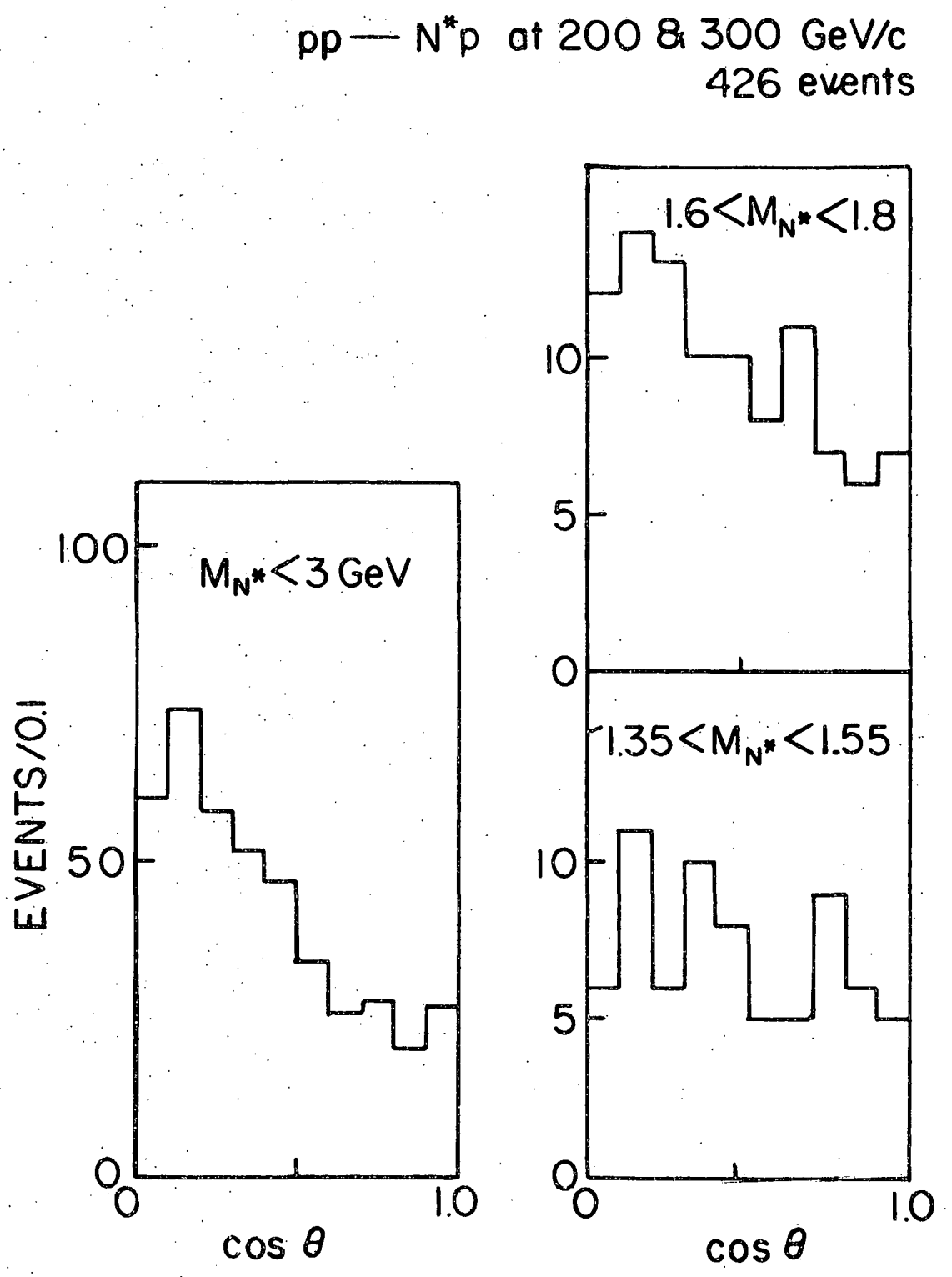

Figure 5.10. The folded polar angular distribution in the normal to the N^* decay plane.

C. Double Excitation

The Double Excitation in the semi-inclusive channels at Fermilab energy was studied by A. Firestone et al. (24) in a bare BC experiment on pp interactions at 300 GeV/c. At ISR energies, the inclusive Double Diffractive Dissociation was investigated by R. Webb et al. (25). Both works supported the hypothesis os pomeron factorization under different cuts. While A. Firestone et al. used the Mass Cut $M^2(p\cdot\pi^+\cdot\pi^-) < 40.0$ GeV^2, R Webb et al. suggested in the text (25) that in their experiment with a t cut: $0.15 < t < 0.53$ GeV/c^2, pomeron factorization holds only for the mass region $M(p\cdot\pi^+\cdot\pi^-) <$ 1.85 GeV. The present analysis attempts for the first time at Fermilab-ISR energies to study the Double Excitation in the exclusive channels with emphasis on the effects of any mass cuts on the tests for pomeron factorization. The hypothesis of pomeron factorization predicts:

$$\frac{\frac{d\sigma}{dt}(pp \to pN^*)}{\frac{d\sigma}{dt}(pp \to pp)} = \frac{\frac{d\sigma}{dt}(pp \to N^*N^*)}{\frac{d\sigma}{dt}(pp \to N^*p)} \qquad (5\text{-}10)$$

The diagrams for each reaction in equation 5-10 are shown in Figure 5.11. The differential cross sections for these reactions can be written in the form:

$$\frac{d\sigma}{dt} = A|\beta_1(t)\beta_2(t)|^2 \qquad (5\text{-}11)$$

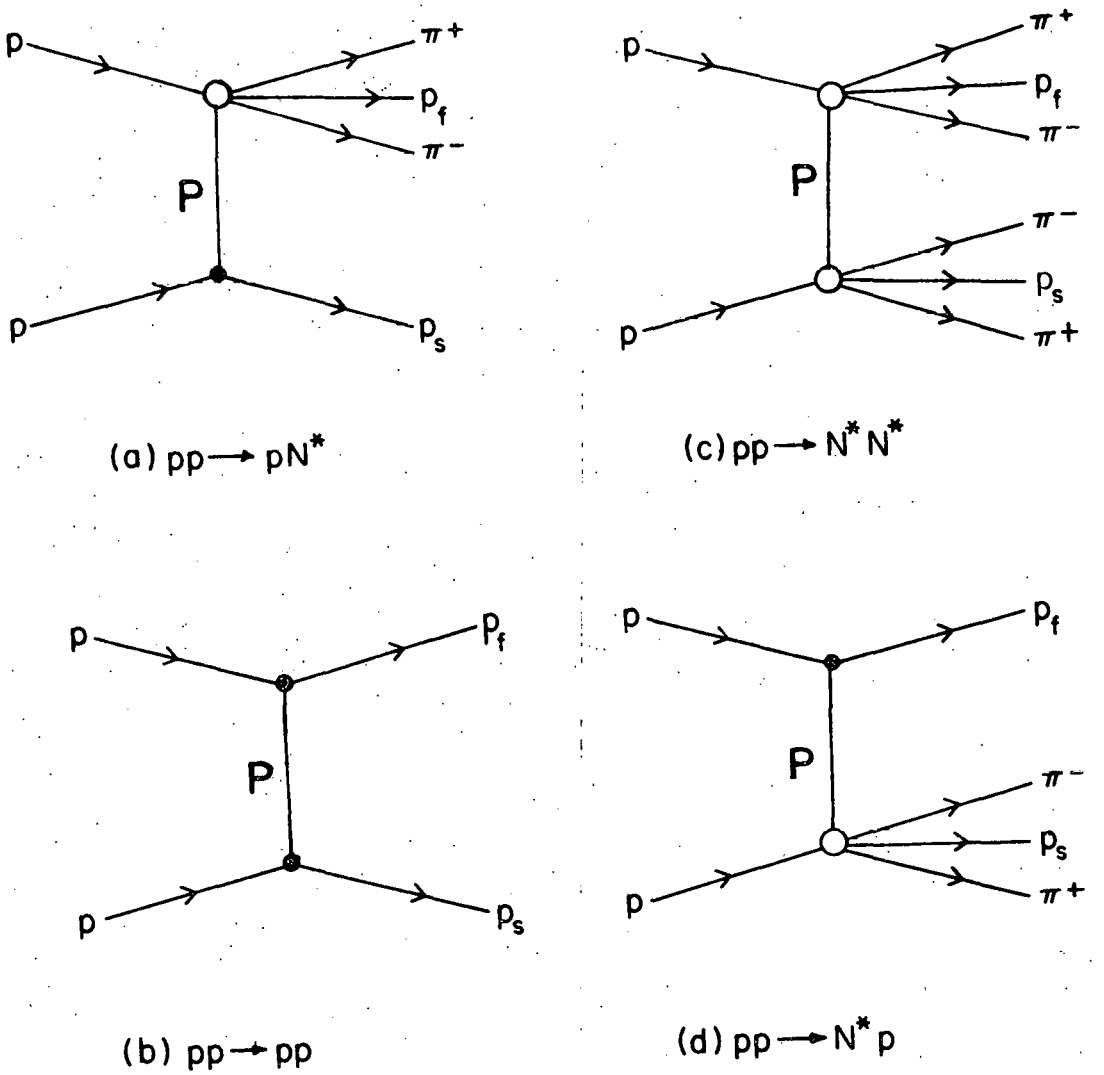

Figure 5.11. (a) and (d): Single diffractive dissociation, (b) Elastic scattering, and (c) Double excitation.

where A is a constant and $\beta(t)$ is a residue function at each vertex in the diagram. It is assumed that the residue function is approximately exponential for the small t region and then it is written as

$$\beta(t) = \beta e^{bt}. \tag{5-12}$$

Also the optical theorem gives

$$\sigma_{tot} = \beta_1(0)\beta_2(0). \tag{5-13}$$

Thus, from the above three equations, the factorization relation (5-10) leads to

$$\frac{\sigma_{SD}\, b_{SD}\, e^{b_{SD}t}}{\sigma_{E\ell}\, b_{E\ell}\, e^{b_{E\ell}t}} = \frac{\sigma_{DE}\, b_{DE}\, e^{b_{DE}t}}{\sigma_{SD}\, b_{SD}\, e^{b_{SD}t}} \tag{5-14}$$

where the abbreviation means:

SD: Single Diffraction

Eℓ: Elastic Scattering

DE: Double Excitation.

The equation (5-14) is satisfied at any t; thus, one obtains the following relations:

$$b_{SD} - b_{E\ell} = b_{DE} - b_{SD} \tag{5-15}$$

and

$$\sigma_{DE} = \frac{(\sigma_{SD})^2}{\sigma_{E\ell}} \cdot \frac{b_{SD}^2}{b_{E\ell}\, b_{DE}} \cdot \qquad (5\text{-}16)$$

Equation 5-16 is different from the formula used in Reference 24 by the factor involving the ratio of the slope parameters.

One way to separate the decay products of target associated N^* from those of beam associated N^* in the $pp\pi^+\pi^-\pi^+\pi^-$ final state is to compare the CM rapidity[10] between protons, positive pions and negative pions respectively. Then the combination $p\pi^+\pi^-$ with the smaller rapidities is assumed to be a target associated N^* and the combination $p\pi^+\pi^-$ with the larger rapidities to be a beam related N^*. The corresponding masses are referred to as $M(P\cdot\pi^+\cdot\pi^-)_{SLOW}$ and $M(p\cdot\pi^+\cdot\pi^-)_{FAST}$ respectively. Figure 5.12 shows the scatter plots of $M(p\cdot\pi^+\cdot\pi^-)_{SLOW}$ with respect to $M(p\cdot\pi^+\cdot\pi^-)_{FAST}$. The low mass enhancements that were observed in $pp\pi^+\pi^-$ final state again stand out on both axes. In the lower left corner of the scatter plot, there is a region where two mass combinations

---

[10] Rapidity is defined as

$$Y = \ell n \frac{E + p_{11}}{E - p_{11}} ,$$

where E is the energy and p_{11} is the longitudinal component of the momentum of the particle. The first order approximation of rapidity is the longitudinal velocity.

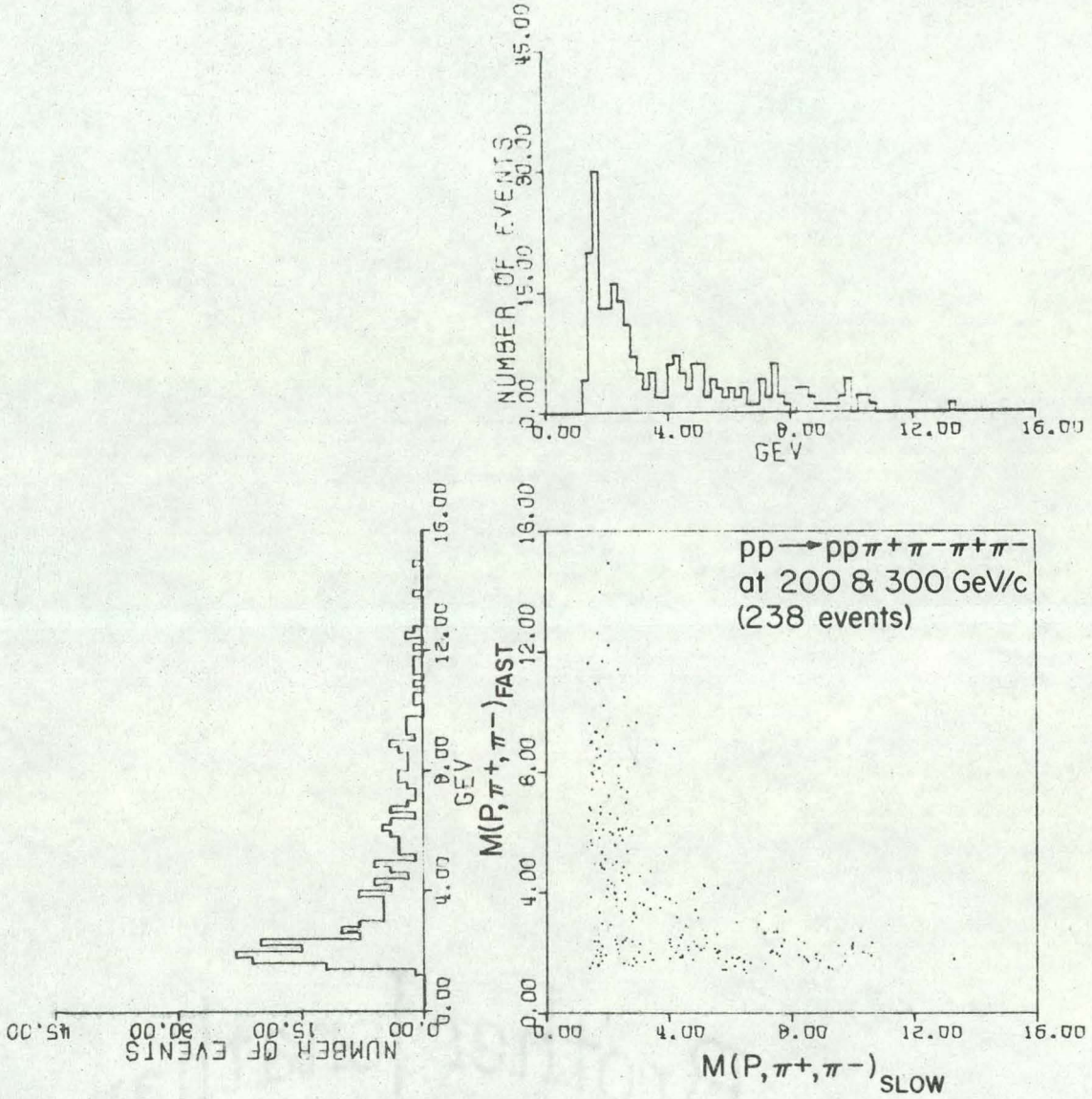

Figure 5.12. The scatter plot of the effective mass $M(p,\pi^+,\pi^-)_{SLOW}$ with respect to $M(p,\pi^+,\pi^-)_{FAST}$.

have low masses of similar magnitudes. The events in this area represent Double Excitation. In Figure 5.13 the CM rapidity distribution for two distinct particle combinations are presented for 200 and 300 GeV/c data. There are two data points $(Y_{(p\pi^+\pi^-)_{SLOW}}$ and $Y_{(p\pi^+\pi^-)_{FAST}}$ per event in the plot. It is evident that beam associated N^* goes forward, the target associated N^* heads backward and there is a rapidity gap between them in the CM frame. The data is symmetric and does not indicate any sign of a background problem.

A more exact way to study the Double Excitation is to look at the particle configuration and charge distributions in the CM frame. In the present analysis, it was decided that a Double Excitation event is required to have:

1. Three particles in the forward hemisphere and three particles in the backward hemisphere.
2. Two positive charges and one negative charge in each hemisphere (see Table 4.4C).

In addition to Single Diffraction cross section and Elastic Scattering cross section, the slope value of the t distributions is needed for the prediction of Double Excitation cross section using equation 5-16. The t distributions for Single Diffraction and Double Excitation events at 200 and 300 GeV/c are presented in Figure 5.14. It should be noted that the t for Single Diffraction is calculated between the

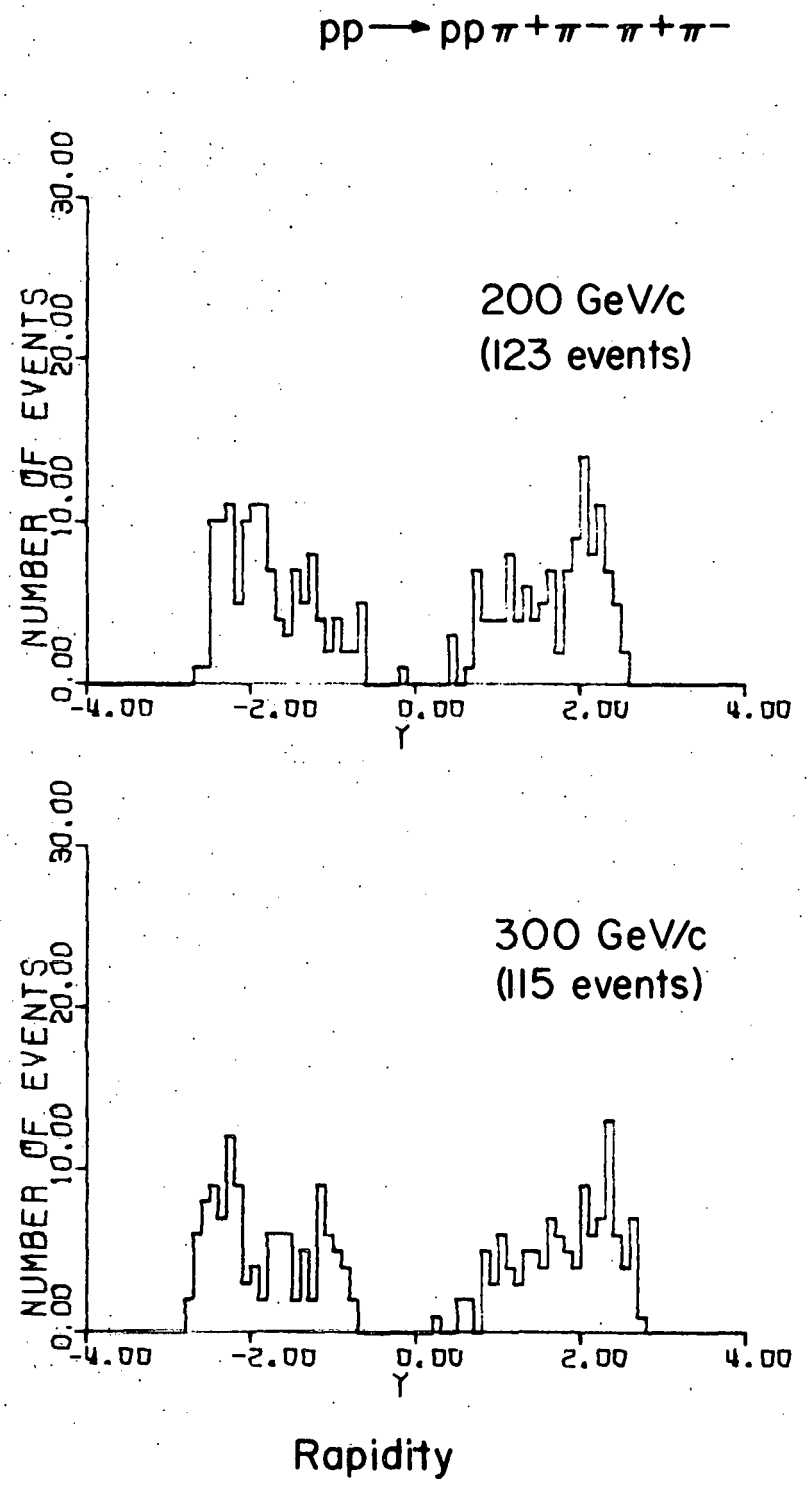

Figure 5.13. The CM rapidity distribution of two $p\pi^+\pi^-$ combinations per event.

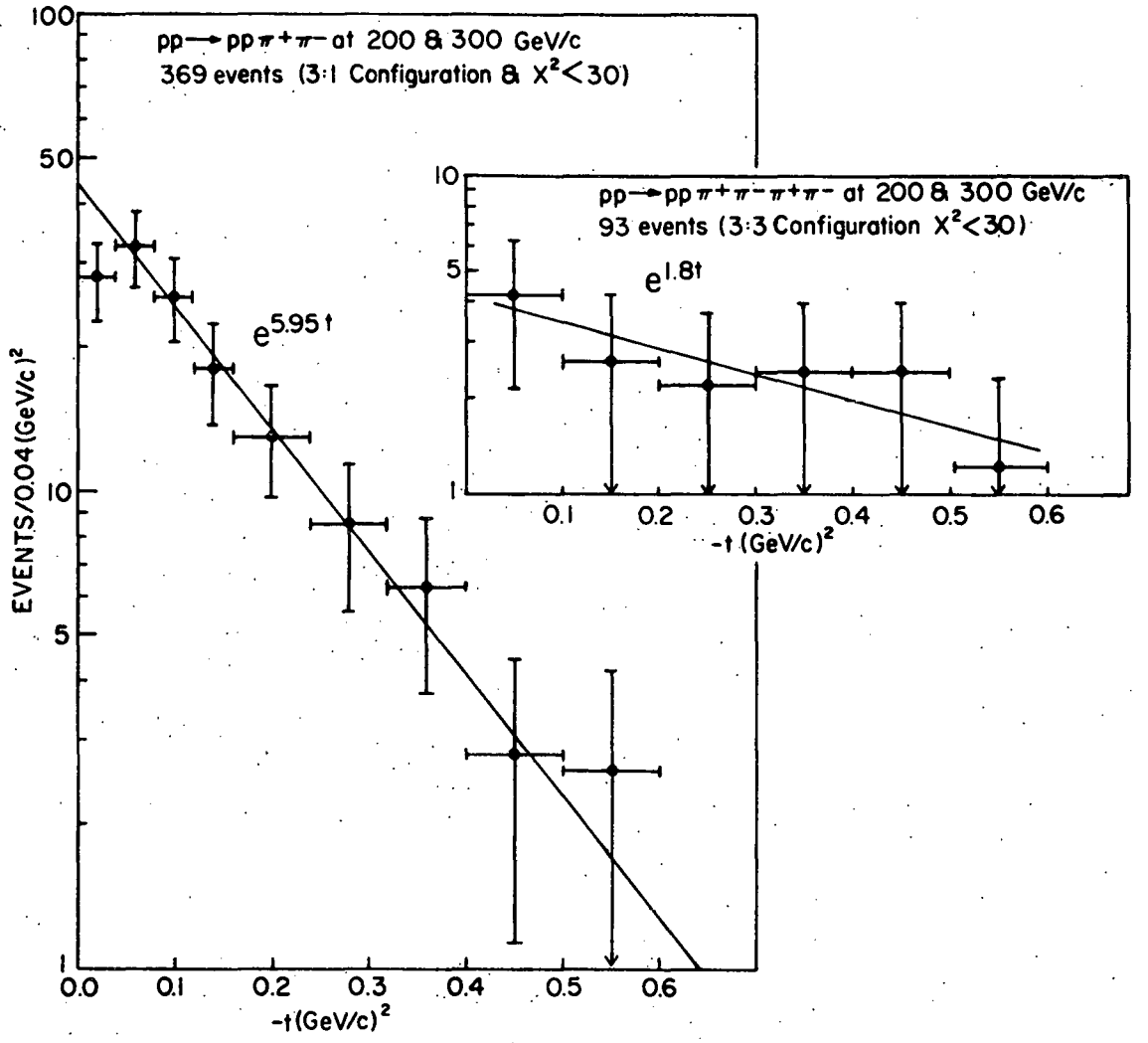

Figure 5.14. The four-momentum transfer squared distribution between the target and slow proton (slow $p\,\pi^+\pi^-$ system).

target and slow proton in the four pronged 4C events with $\chi^2 < 30$ and only for events with a one backward to three forward division of the particles. For Double Excitation events, t is between the target and the $(p\cdot\pi^+\cdot\pi^-)_{SLOW}$ system in the 6 pronged 4C events ($\chi^2 < 30$) with a three to three particle configuration (two positive charge to one negative charge in each group in the CM frame). Using the averaged slope for elastic events: $b = 10 \pm 0.5$ at 200 and 300 GeV/c, the relation (5-15) between slope parameters is well satisfied; namely,

$$b_{SD} - b_{E\ell} = -4.05$$

and

$$b_{DE} - b_{SD} = -4.15.$$

The estimated cross section for Diffractive Dissociation strongly depends upon the mass cut that is used to define the N^*. This is also true of the result of the test on pomeron factorization. Table 5.3 presents the cross sections using different mass cuts for the N^*, together with the predicted Double Excitation cross section using equation 5-16. The agreement between the measured σ_{DE} and the predicted σ_{DE} becomes quite good as the mass cut is reduced. There is no doubt that agreement with the prediction of pomeron factorization requires the mass cut $M(p\cdot\pi^+\cdot\pi^-) \leq 2.5$ GeV, which supports the observation of R. Webb et al. (25).

Table 5.3. Double Excitation.

Cut on $M(p\cdot\pi^+\cdot\pi^-)$ (GeV)	σ_{SD} (μb)	σ_{DE} (Predicted) (μb)	# of D.E. Events	σ_{DE} (Experimental) (μb)
6	415 ± 64	49 ± 11	133	280 ± 63
3	337 ± 44	33 ± 12	30	63 ± 20
2.5	298 ± 49	25 ± 10	18	38 ± 15
2.0	206 ± 37	12 ± 5	8	17 ± 9

D. Double Pomeron Exchange

The Exclusive Double Pomeron Exchange (DPE) at Fermilab energies was first studied by Derrick et al. (26) in the 200 GeV/c pp experiment using the bare 30-inch bubble chamber. This analysis was based upon 191 events in the $pp\pi^+\pi^-$ final state. Using a cut on the proton-pion effective mass ($M^2_{p\pi} \geq 4\ GeV^2$) for all combinations, 9 events were identified as DPE candidates. These were then used to obtain an upper limit of $44 \pm 15\ \mu b$ for the DPE process. After a further cut on the pion-pion mass ($M\pi^+\pi^- < 0.6\ GeV$), only 2 events (9 μb) were left, so these authors concluded that there is no experimental evidence for the DPE process. D. M. Chew (27) took a distinctly different approach to the problem using a variable called Z. The Z variable is defined in terms of the ratio between the square of the center of mass energy and the missing mass squared with respect to one of the protons. Thus two Z variables are defined for each $pp\pi^+\pi^-$ final state (APPENDIX B):

$$Z_A \equiv \ln \frac{S}{M^2_{XA}}$$

$$Z_B \equiv \ln \frac{S}{M^2_{XB}} \qquad (5\text{-}17)$$

According to the definition by D. M. Chew (27), the DPE events, illustrated in Figure 5.15, are those which have:

$$z_A \gtrsim 2.3 \text{ and } z_B \gtrsim 2.3 \qquad (5\text{-}18)$$

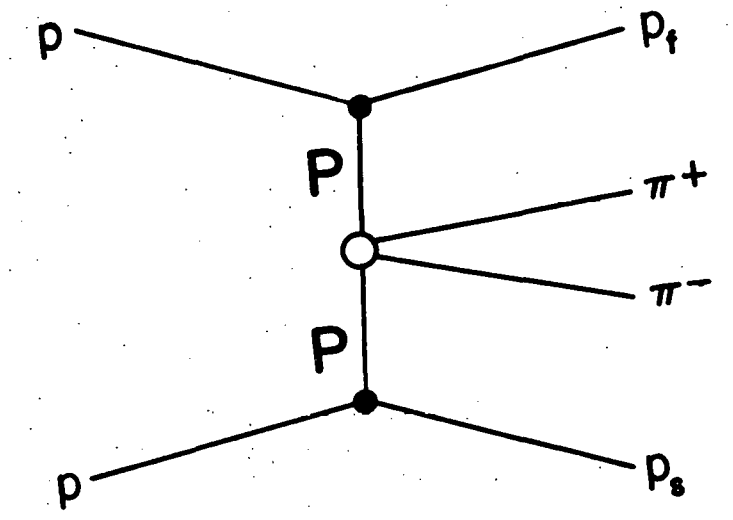

Figure 5.15. Double Pomeron Exchange

Using this cut, the ANL experiment had 17 DPE candidates, which corresponds to 60 ± 15 μb. However, D. M. Chew pointed out that the statistics of the data are insufficient to argue the presence or absence of the DPE process.

Since the present report has the most events in this $pp\pi^+\pi^-$ channel presently available at Fermilab energies, an attempt will be made to clarify the accumulated speculation about the DPE process. Before further discussion, it should be mentioned here that the very idea of multiple pomeron exchange is subject to a theoretical difficulty if the intercept of the trajectory is one (28).

Using the definition (5-18), the DPE cross sections in the present experiment have been estimated (Table 5.4).

Table 5.4. Estimated DPE cross sections.

p GeV/c	DPE Candidates	σ_{DPE} (Estimated) (μb)
200	34	95 ± 19
300	32	115 ± 26

The estimated DPE cross section at 200 GeV/c from the present data is higher than the previous measurement (17 DPE events, 60 ± 15 μb) by the ANL group. In Table 5.5, the configuration of the particles for the DPE candidates in the CM frame is presented. It should be noted that the distribution is symmetric in the CM frame and that 50% of the DPE candidates have a two-to-two division of particles in the CM frame. Shown in Figures 5.16, 5.17 and 5.18 are the triangle plots for events from the reaction $pp \rightarrow pp\pi^+\pi^-$ at 200 GeV/c, 300 GeV/c and the summed data from both energies. The DPE candidates are confined by the $Z_A = 2.3$ line, the $Z_B = 2.3$ line and the solid line which defines the boundary due to the available energy for the process. Of course, the two

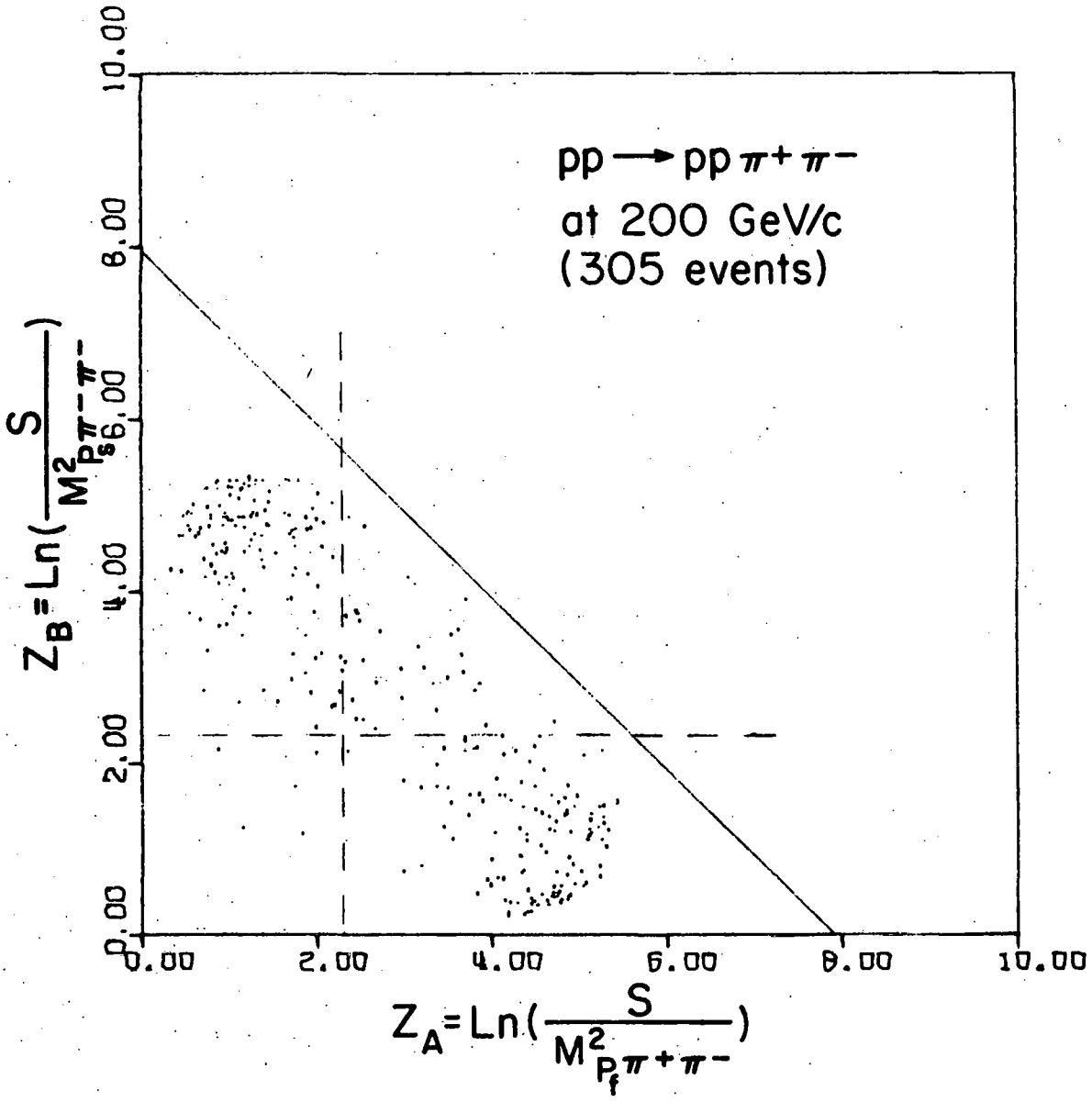

Figure 5.16. The triangle plot with events of the reaction pp → pp $\pi^+\pi^-$ at 200 GeV/c.

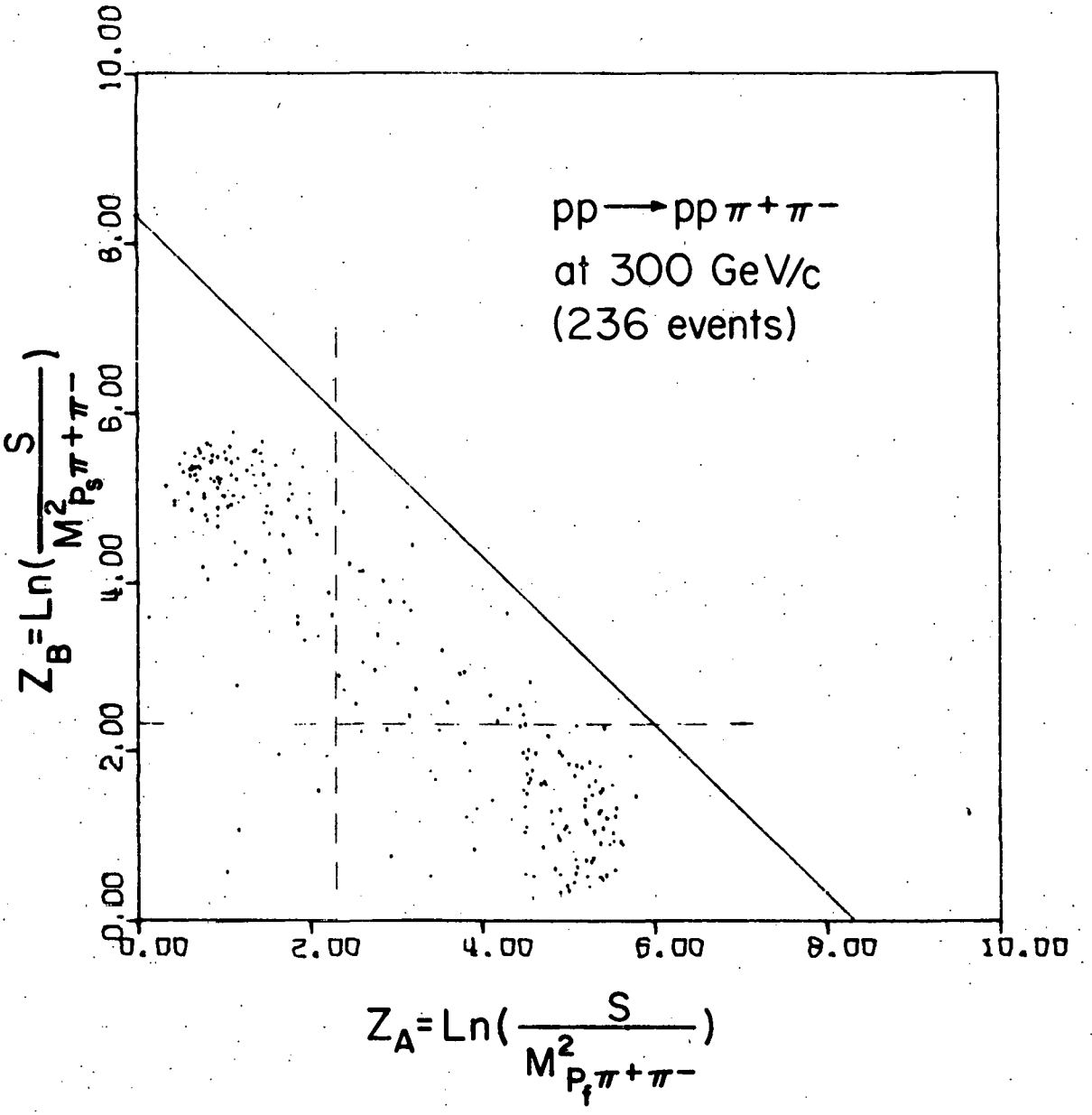

Figure 5.17. The triangle plot with events of the reaction $pp \rightarrow pp\pi^+\pi^-$ at 300 GeV/c.

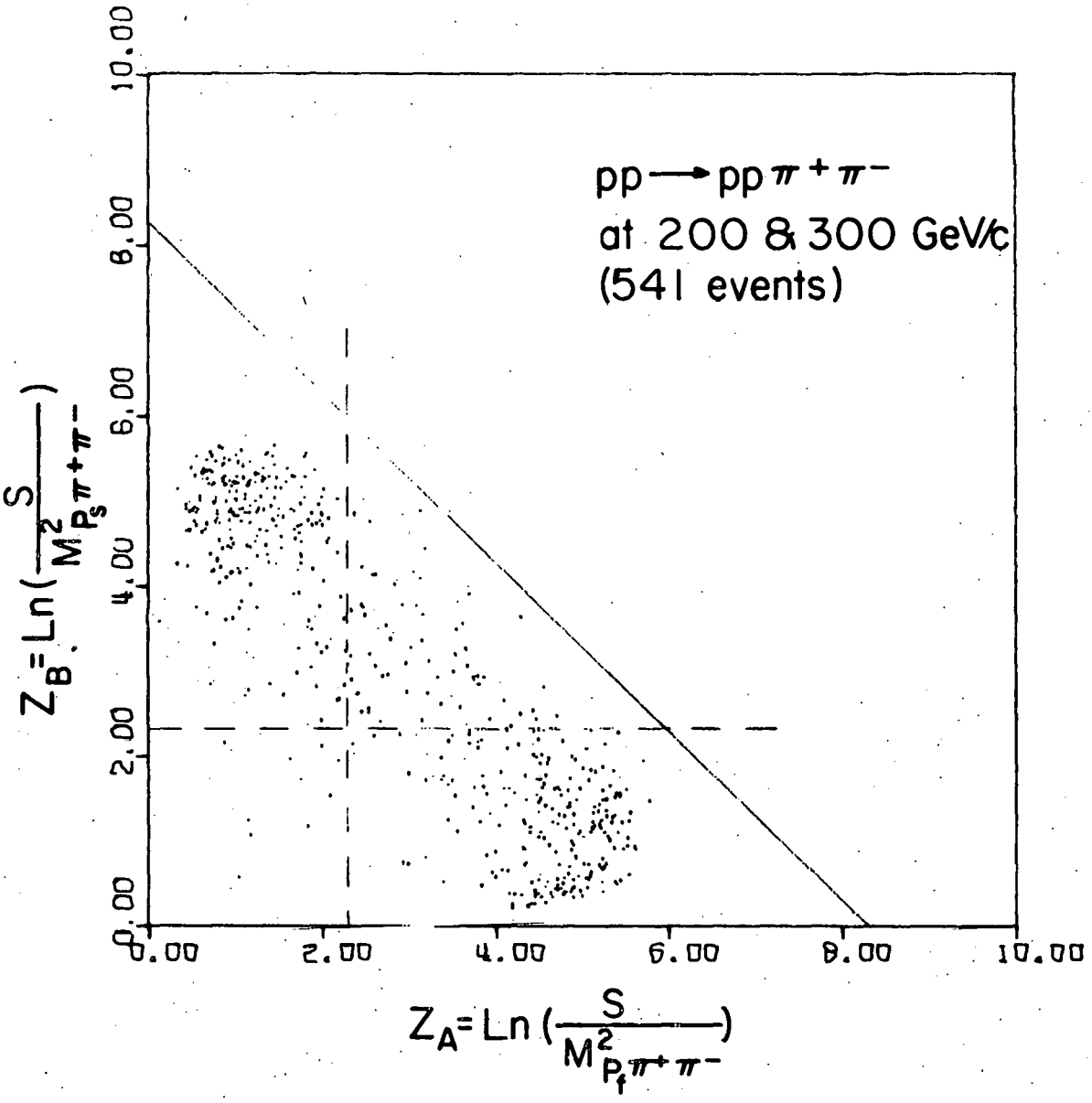

Figure 5.18. The triangle plot with events of the reaction $pp \rightarrow pp\,\pi^+\pi^-$ at 200 and 300 GeV/c.

Table 5.5. Configuration of particles of DPE candidates in CM frame.

p GeV/c	3F : 1B	2F : 2B	1F : 3B
200	9	17	8
300	10	10	6

highly populated areas correspond to target and beam diffractive dissociation, discussed earlier in this chapter. Alternately, it is also possible to present the data using the variables:

$$Z_X \equiv \ell n \frac{S}{S_o} - (Z_A + Z_B) \qquad (5\text{-}19)$$

and

$$Z \equiv \tfrac{1}{2} (Z_A - Z_B) \qquad (5\text{-}20)$$

where Z_A and Z_B were defined previously and $S_o \approx 0.14$ GeV^2. Figures 5.19 and 5.20 show these new triangle plots for events at 200 and 300 GeV/c. Again the DPE candidates are located inside the smaller triangle in each figure.

In order to examine the reliability of the definition of DPE (5-18) by D. M. Chew, we shall now investigate the contamination from diffractive events in our DPE samples

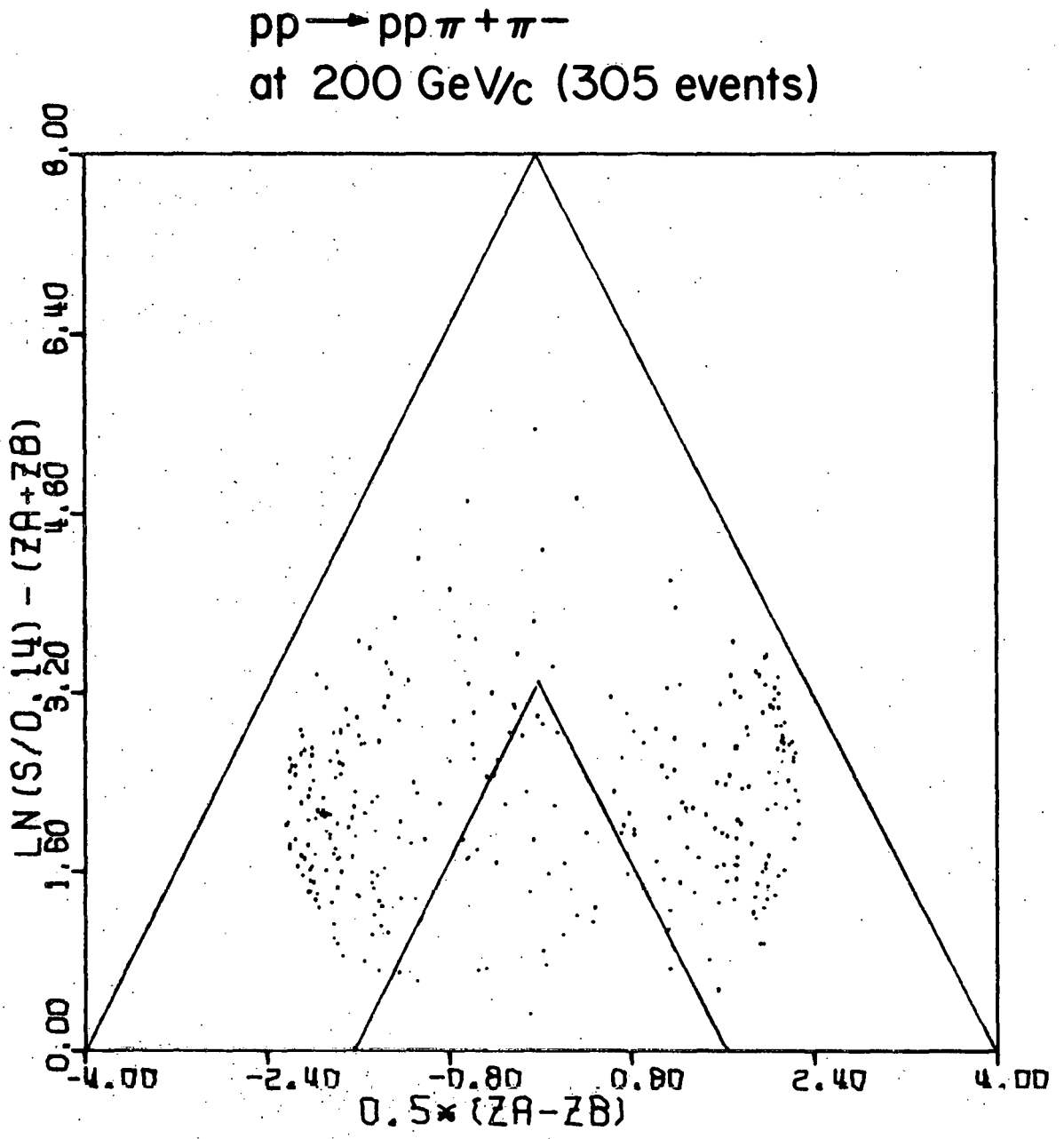

Figure 5.19. The triangle plot with events of the reaction $pp \rightarrow pp\pi^+\pi^-$ at 200 GeV/c.

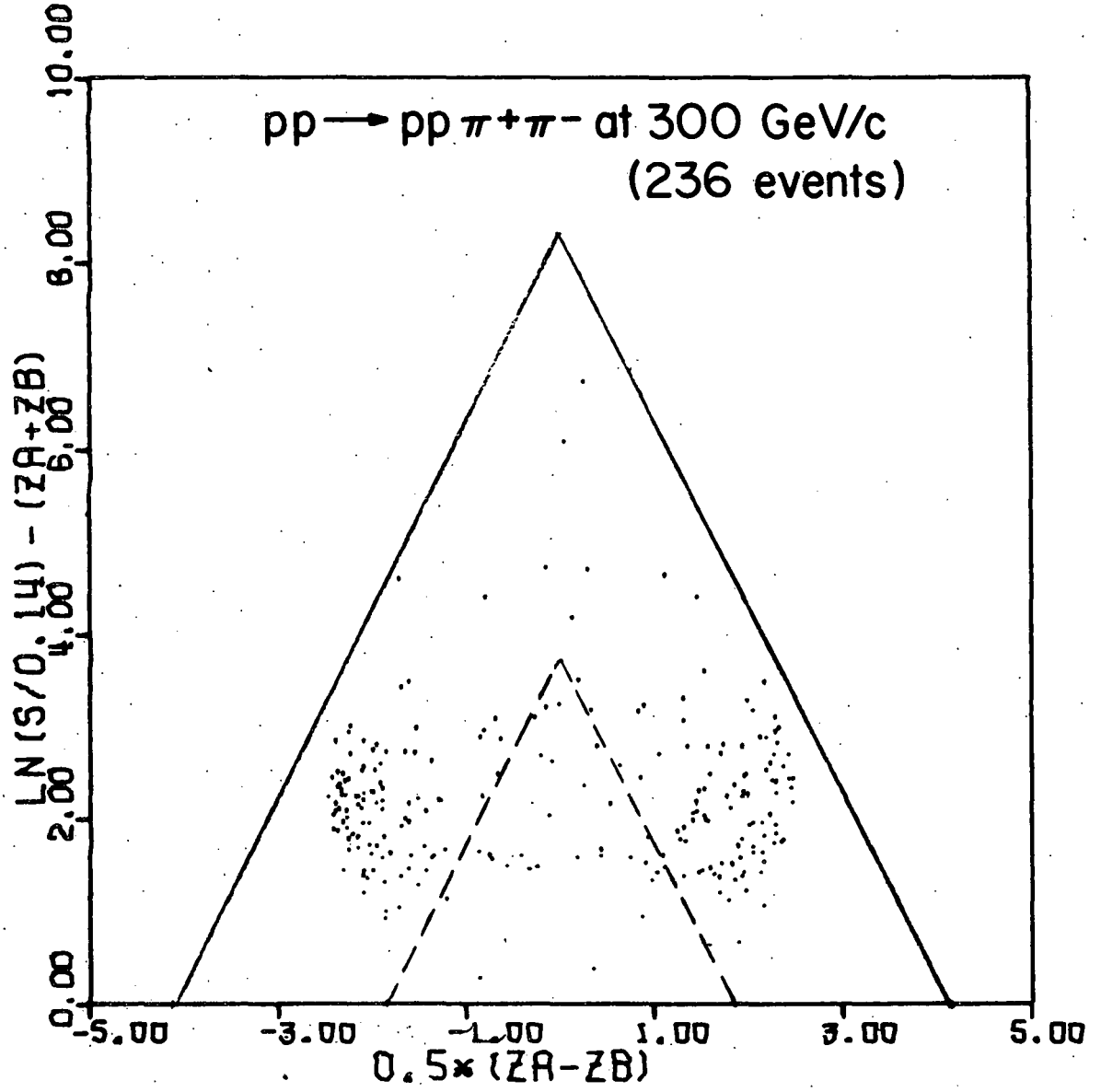

Figure 5.20. The triangle plot with events of the reaction $pp \rightarrow pp\pi^+\pi^-$ at 300 GeV/c.

presented in Tables 5.4 and 5.5. Shown in Figure 5.21 are the mass distributions of the proton-π^+ combinations. The DPE candidates defined by equation 5-18 are shaded in the figures. Although no strong signal for Δ^{++} production is seen in the DPE candidates, there are 31 events out of 66 DPE candidates that have $M(p\,\pi^+) < 2$ GeV. Figure 5.22 presents the distributions of: (a) Φ_{pp}; azimuthal angle between the two final state protons and (b) $M(p\cdot\pi^+\cdot\pi^-)_{smallest}$. The Φ_{pp} distribution for the DPE candidates is similar to those of the entire 4 pronged 4C events that are dominated by Single Diffractive Dissociation; namely there is an excess of events between 90° and 180°. Of 541 events in the $pp\,\pi^+\pi^-$ final state, 193 events are between 0° and 90° and 348 events are between 90° and 180°. As for DPE candidates, 25 events are in 0° - 90° and 41 events are in 90° - 180° regions. In the distribution of $M(p\cdot\pi^+\cdot\pi^-)_{smallest}$ 24 events (36%) out of 66 DPE candidates have $M(p\cdot\pi^+\cdot\pi^-)_{smallest} < 3$ GeV. These events could well be candidates for interpretation as Single Diffraction. The mass of the two pion system is shown in Figure 5.23 together with the rapidity of the $\pi^+\pi^-$ combination. There are 24 DPE candidates in the mass range $0.6 < M(\pi^+\pi^-) < 0.94$ GeV, in which seven events have the corresponding $M(p\cdot\pi^+\cdot\pi^-)_{smallest} < 3$ GeV. The cut $M(\pi^+\pi^-) < 0.6$ GeV used by the ANL group (26) was criticized in Reference 27 as "far below beginning of DPE region." This argument

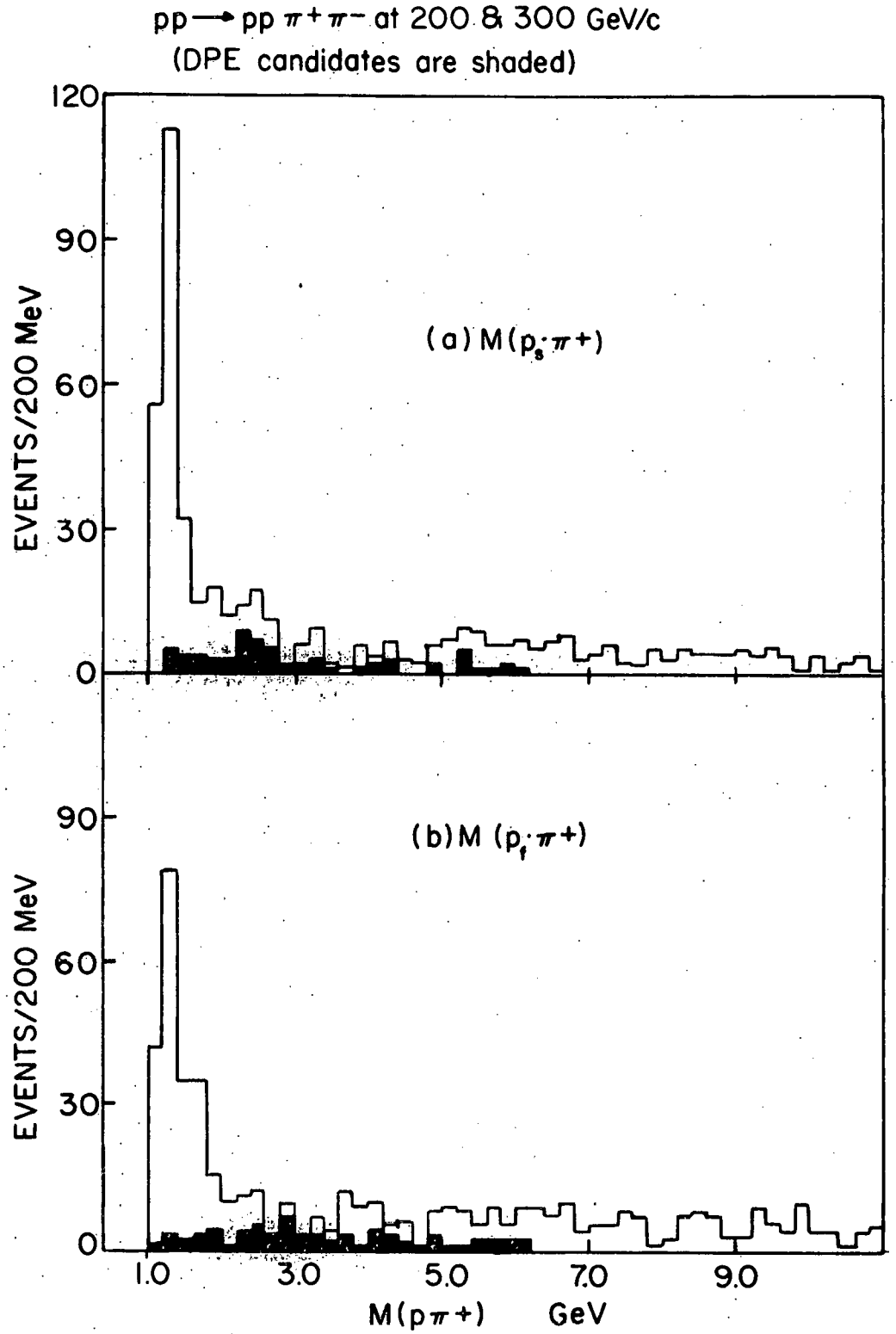

Figure 5.21. The effective-mass distribution of two $p\pi^+$ combinations.

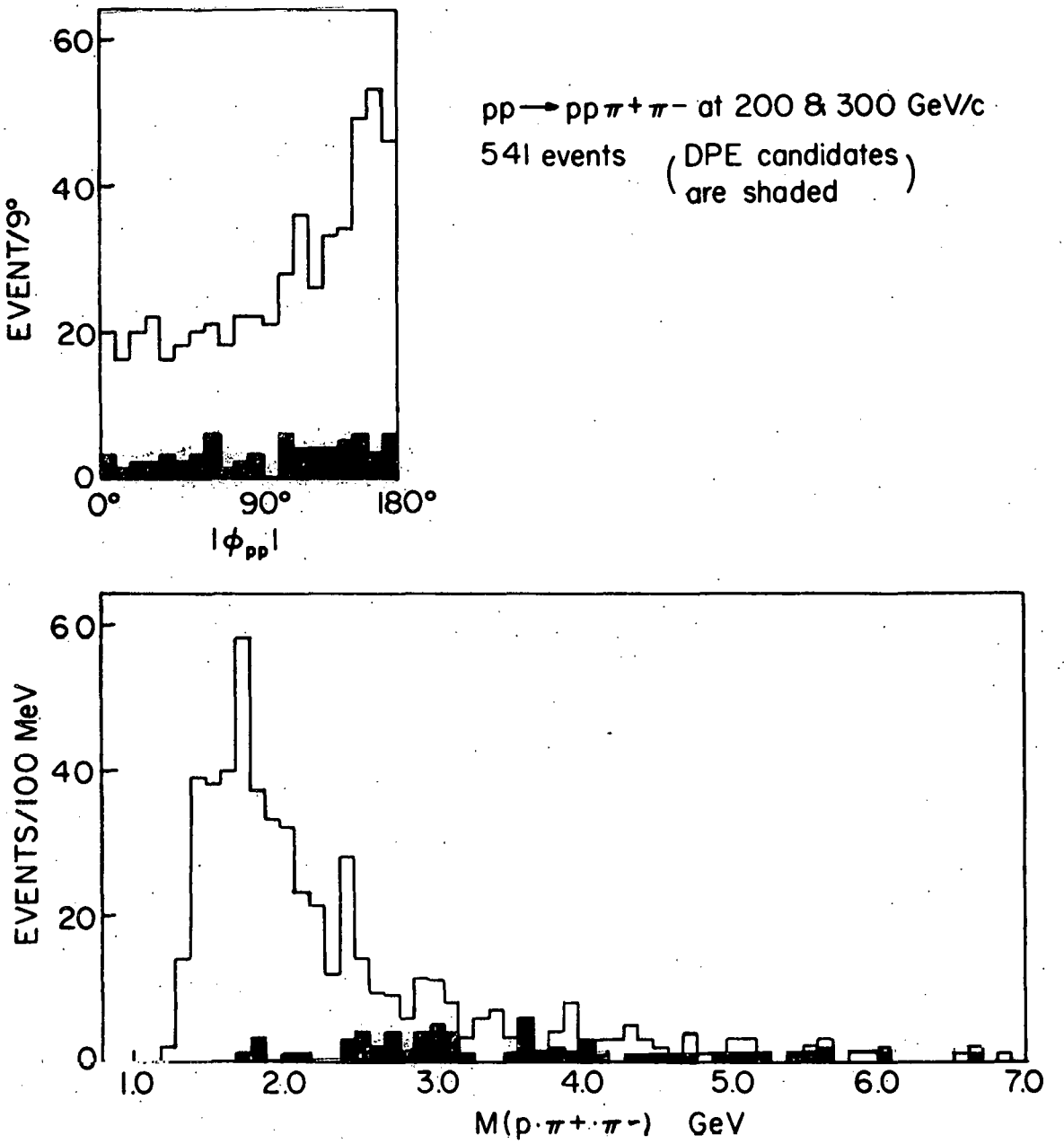

Figure 5.22. The distribution of (a) azimuthal angle between proton and proton, and (b) the $M(p \cdot \pi^+ \cdot \pi^-)_{\text{smallest}}$.

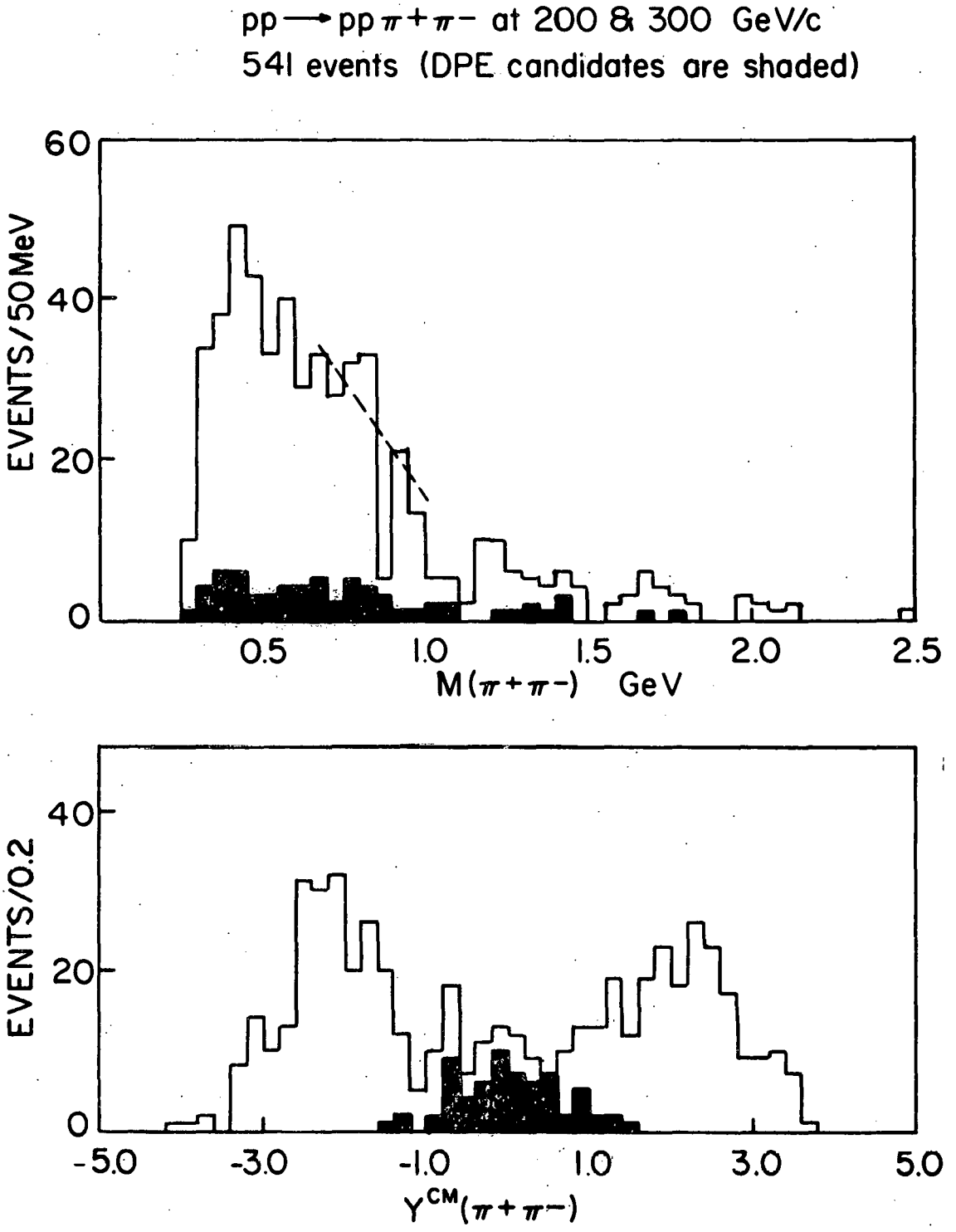

Figure 5.23. The distribution of (a) the effective mass of $\pi^+\pi^-$ combination, and (b) the rapidity of $\pi^+\pi^-$ combination.

in Reference 27 is somewhat oversimplified, since the newly proposed cut on the Z variable (5-18) does not eliminate the possible contamination from ρ° production at all. We shall, for the moment, assume that real DPE events are dominated by a low mass s wave $\pi\pi$ system; namely, events with $M(\pi^+\pi^-) < 0.6$ GeV. There are 27 DPE candidates with $M(\pi^+\cdot\pi^-) < 0.6$ GeV in the data sample of this experiment. In addition, 17 events out of 24 DPE candidates with $M(p\cdot\pi^+\cdot\pi^-) < 3$ GeV also have $M(\pi^+\cdot\pi^-) < 0.6$ GeV. Thus 63% of the good DPE candidates ($M(\pi^+\pi^-) < 0.6$ GeV) are associated with low mass enhancement of the $p\pi^+\pi^-$ system where the mass is smaller than 3 GeV. In the previous section, it was shown that pomeron factorization is satisfied if N^* mass is assumed to be less than 2.5 GeV. A cut at 3 GeV for the N^* mass also gave a reasonable result. If these facts are taken into account, one can conclude that a large fraction of the good DPE candidates ($M(\pi^+\pi^-) < 0.6$ GeV) are Single Diffraction events. Therefore, the cut (5-18) proposed by D. M. Chew has serious difficulty in selecting DPE events in that it does not provide clean separation of DPE events from diffractive events in the low $M(\pi^+\pi^-)$ region. There are 7 DPE candidates in HOOKUP 4 pronged 4C channel at 200 and 300 GeV/c. Of these, 6 events are also DPE candidates when SC information is not used. One HOOKUP DPE candidate does not have DPE fit when the SC information is ignored. Thus, the

uncertainty of kinematic fitting for DPE candidates is relatively small. This may be due to the fact that 50% of DPE candidates have two-to-two division of particles in the CM frame.

In this section, so far two points have been discussed:

a. The definition of DPE by D. M. Chew is questionable.

b. The DPE candidates from bare BC data are relatively clean.

Now one needs to discuss the heart of the problem; that is, the experimental feature of good DPE candidates. It was pointed out earlier that 63% of good DPE candidates ($M(\pi^+\cdot\pi^-) < 0.6$ GeV) may be single diffractive events. Then, how about the remaining 37% of DPE candidates with $M(\pi^+\cdot\pi^-) < 0.6$ GeV? Since Z variables are equivalent to rapidity gaps, up to displacements of the order of 1(27), it is not wise to reexamine the rapidity distributions of DPE candidates. Rapidity distributions and the relations between Z variables and rapidity are shown in APPENDIX B. By studying all other distributions for DPE candidates with $M(\pi^+\cdot\pi^-) < 0.6$ GeV and $M(p\cdot\pi^+\cdot\pi^-)_{smallest} > 3$ GeV, it is found that there is one interesting feature in the distribution of ϕ_{pp}. There are 8 events in $0° - 90°$, but only 2 events are in $90° - 180°$ range. This is a remarkable contrast to the ϕ_{pp} distribution of Single Diffractive events, which had a peak at 180° (Figure 5.22). The excess of DPE

events in $0 < \phi_{pp} < 90°$ region may be attributed to the small azimuthal angle between π^+ and π^- and the overall transverse momentum conservation in the $pp\pi^+\pi^-$ final state. In summary, the clean DPE signal is small in the present experiment. Based on the restrictions $M(\pi^+ \cdot \pi^-) < 0.6$ GeV and $M(p \cdot \pi^+ \cdot \pi^-)_{smallest} > 3$ GeV, one obtains 10 DPE events which correspond to 16 ± 7 μb.

E. Two Particle Exclusive Azimuthal Correlation

An extensive literature has built up in recent years on the examination of inclusive two particle correlations at high energies (5). However, most of the studies were restricted to the central region and to the specific particle multiplicity range: $< n > \lesssim n \lesssim 2 < n >$. In low multiplicity events, there are complications due to diffraction and the details of the two particle correlation are unexplored as yet at Fermilab energies. In this section, attention is paid to the two-particle correlations in the 4-pronged and 6-pronged events in pp interactions at 200 and 300 GeV/c. We shall confine ourselves to the study of two particle azimuthal correlations.

The azimuthal angle between the transverse components of the momenta of particles i and j can be defined as (Figure 5.24):

$$\phi_{ij} = \cos^{-1}\left[\frac{\vec{p}_{iT}\cdot\vec{p}_{jT}}{p_{iT}\ p_{jT}}\right] \qquad (5\text{-}21)$$

From transverse momentum conservation, one expects:

$$\langle \cos\phi_{ij} \rangle \propto -\frac{1}{n-1},$$

where n is the particle multiplicity. This means that the two particle azimuthal distributions have a peak at $\phi = 180°$. The peak becomes less pronounced as the multiplicity increases.

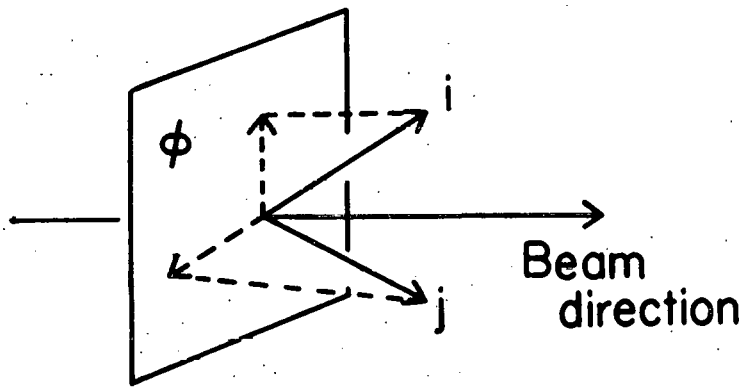

Figure 5.24. Azimuthal angle between particle i and particle j.

The distribution in azimuthal angle for events with n particles would be given by:

$$\frac{d\sigma_n}{d\phi} = \sum_{i>j} \frac{d\sigma_n}{d\phi_{ij}} \qquad (5\text{-}22)$$

An interesting quantity to measure is the Asymmetry Coefficient A_n:

$$A_n = \left[\int_{\pi/2}^{\pi} \frac{d\sigma_n}{d\phi}\, d\phi - \int_{o}^{\pi/2} \frac{d\sigma_n}{d\phi}\, d\phi \right] / \int_{o}^{\pi} \frac{d\sigma_n}{d\phi}\, d\phi \,. \qquad (5\text{-}23)$$

The proto-statistical model (29), which makes only two assumptions, namely that transverse momentum is conserved and that the distribution in transverse momentum is a Gaussian distribution would predict that:

$$A_n = \frac{1}{n-1} \qquad (5\text{-}24)$$

where n is the particle multiplicity. For n = 4 this yields $A_4 = 0.33$ and for n = 6, $A_6 = 0.20$, both of which would be independent of energy. Any deviation of the experimental results from the A_n predicted by the proto-statistical model would indicate the existence of correlations due to some additional dynamical effect.

A recent study by Pratap et al. (30) at 205 GeV/c concludes "that there are azimuthal correlations present which cannot be explained solely by energy and momentum conservation ...". This result of Reference 30 is based upon studies of the inclusive and semi-inclusive data. In order

to understand the effect, a comparison is made in the present experiment between the asymmetry coefficients in the exclusive channel and the same coefficients in the semi-inclusive channel. For this comparison, the identity of the proton is not always known in the unconstrained events with missing neutral particles, so the coefficients have been calculated using only the charges, that is A^{++}, A^{+-}, A^{--} or A^{cc} where the latter includes all charged pairs. The results reported here for the semi-inclusive channel use only the data from the Iowa State group, but the results at 200 GeV/c is consistent with the result at the same energy reported in Reference 30 except for A^{--} in the 6-pronged events. These results are presented in Table 5.6. The prediction (5-24) is in excellent agreement with the exclusive channel data. This strongly suggests that the two-particle exclusive azimuthal correlation is dominated by the kinematics. There are obvious differences between the coefficients for the exclusive channel and those for the semi-inclusive channel. An attempt to use the proto-statistical model to explain the coefficients for the semi-inclusive data requires an average number of neutral particles well in excess of the measured average number of neutral particles for each topology, again in agreement with the conclusions of Reference 30. However, the above result may possibly be explained without using additional dynamical

Table 5.6. Two particle azimuthal correlation.[a]

Energy	Topology or Final States	A^{cc}	A^{++}	A^{+-}	A^{--}
	$pp\pi^+\pi^-$	0.32 ± 0.02	0.31 ± 0.02	0.32 ± 0.02	-
200	All 4 prongs	0.15 ± 0.01	0.13 ± 0.01	0.16 ± 0.01	-
GeV/c	$pp\pi^+\pi^-\pi^+\pi^-$	0.20 ± 0.01	0.17 ± 0.02	0.25 ± 0.02	0.07 ± 0.03
	All 6 prongs	0.08 ± 0.01	-0.01 ± 0.01	0.17 ± 0.01	-0.22 ± 0.03
	$pp\pi^+\pi^-$	0.33 ± 0.02	0.33 ± 0.03	0.34 ± 0.02	-
300	All 4 prongs	0.14 ± 0.01	0.12 ± 0.01	0.16 ± 0.01	-
GeV/c	$pp\pi^+\pi^-\pi^+\pi^-$	0.15 ± 0.01	0.09 ± 0.01	0.21 ± 0.02	0.06 ± 0.02
	All 6 prongs	0.10 ± 0.01	0.02 ± 0.01	0.19 ± 0.01	-0.21 ± 0.02

[a]Coefficients for exclusive channels are determined from complete data set (Experiment 2B). Coefficients for semi-inclusive channels are from ISU set only. Errors indicated are statistical errors only.

argument, if one considers the distribution of neutral particles, especially of π^o's associated with a particular multiplicity. The averaged π^o's multiplicity in n pronged events is:

$$\langle \pi^o \rangle_n = \frac{1}{\sigma_n} \sum_{n'=0}^{N} n' \, \sigma_{n',n} \qquad (5\text{-}25)$$

where σ_n: π^o's production cross section in n-pronged events. $\sigma_{n',n}$: the partial cross section for n' neutral pion production in n-pronged events. Then the asymmetry coefficient for n-pronged events is given by:

$$A_n = \frac{1}{\sigma_n} \sum_{n'=0}^{N} \frac{\sigma_{n',n}}{(n+n')-1} \qquad (5\text{-}26)$$

Since $\sigma_{n',n}$ is not available, no attempt is made to examine this point of view. In order to display the energy dependence of the difference between the exclusive and semi-inclusive channels, Figure 5.25 shows A^{CC} for 4 and 6-pronged events, both exclusive and semi-inclusive from this experiment and the earlier 28.5 GeV/c data of Reference 30. An important point to note for the asymmetry in the $pp \to pp\pi^+\pi^-$ channel is the lack of energy dependence, particularly the lack of any sign of a decrease with increasing energy. The asymmetry coefficients for different particle combinations at 200 and 300 GeV/c are given in Table 5.7 for each exclusive reaction.

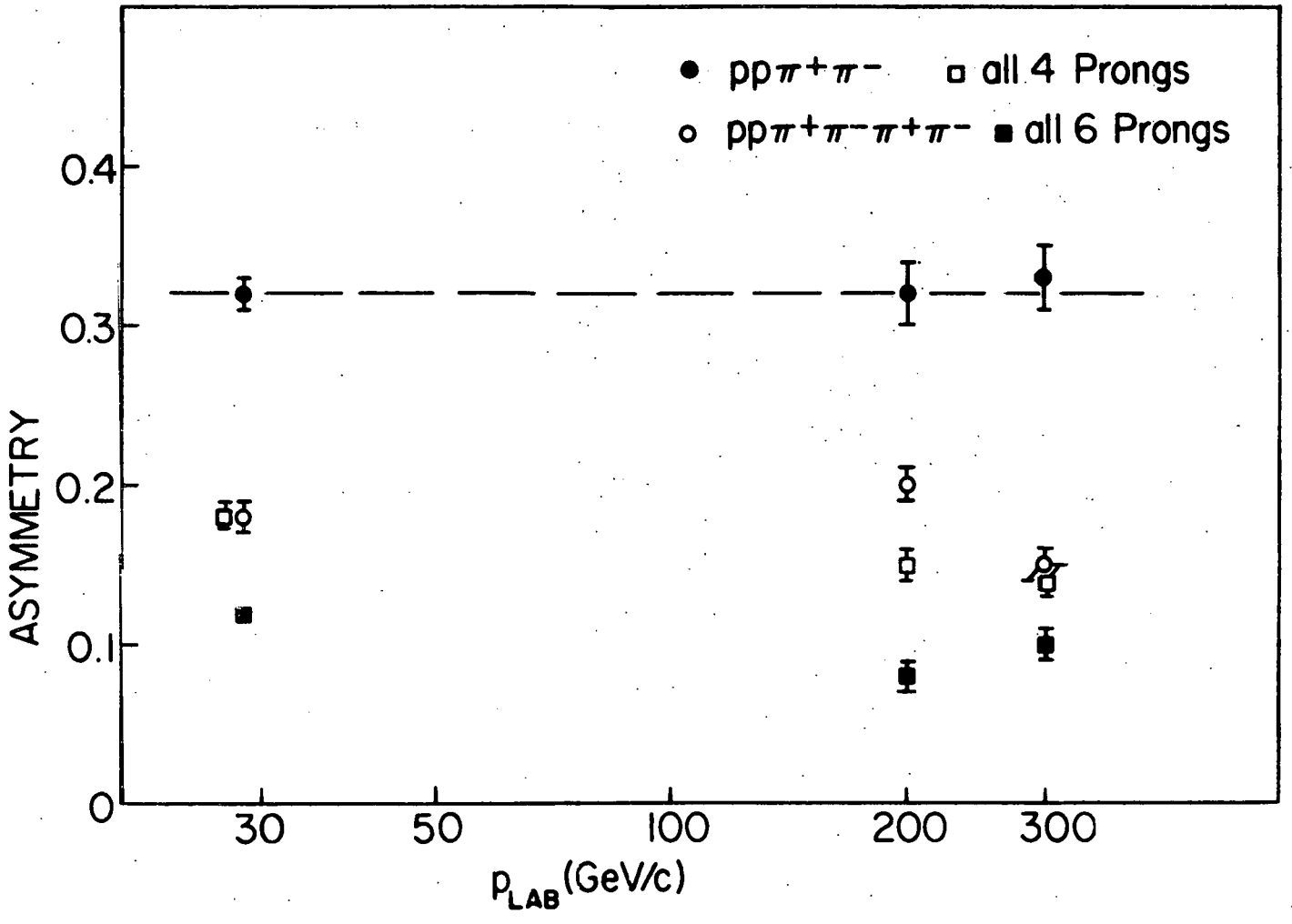

Figure 5.25. Azimuthal asymmetry for different reactions as a function of laboratory momentum.

Table 5.7. Asymmetry parameters for exclusive channels.[a]

Asymmetry Parameters	Final States	
	$pp\pi^+\pi^-$	$pp\pi^+\pi^-\pi^+\pi^-$
A^{cc}	0.33 ± 0.01	0.19 ± 0.01
A^{pp}	0.29 ± 0.03	0.26 ± 0.04
$A^{p\pi^+}$	0.34 ± 0.02	0.14 ± 0.01
$A^{p\pi^-}$	0.37 ± 0.02	0.28 ± 0.01
$A^{\pi^+\pi^-}$	0.26 ± 0.02	0.18 ± 0.02
$A^{\pi^+\pi^+}$	-	0.16 ± 0.03
$A^{\pi^-\pi^-}$	-	0.07 ± 0.02

[a]Errors indicated are statistical errors only.

The data are plotted in Figure 5.26 for $pp\pi^+\pi^-$ final state and in Figure 5.27 for $pp\pi^+\pi^-\pi^+\pi^-$ final state. The correlation among pions is weaker than the correlation between proton and pion or between proton and proton. This has been known as "mass effects" (29). This "mass effect" was also seen in a Monte Carlo calculation. Using a simple Matrix Element of the Diffractive Excitation Model and the experimentally determined t slopes in the density function, the program FOWL (31) reproduced the features of the $pp\pi^+\pi^-$ final state quite well including the mass distributions, transverse momentum distributions and asymmetry coefficients.

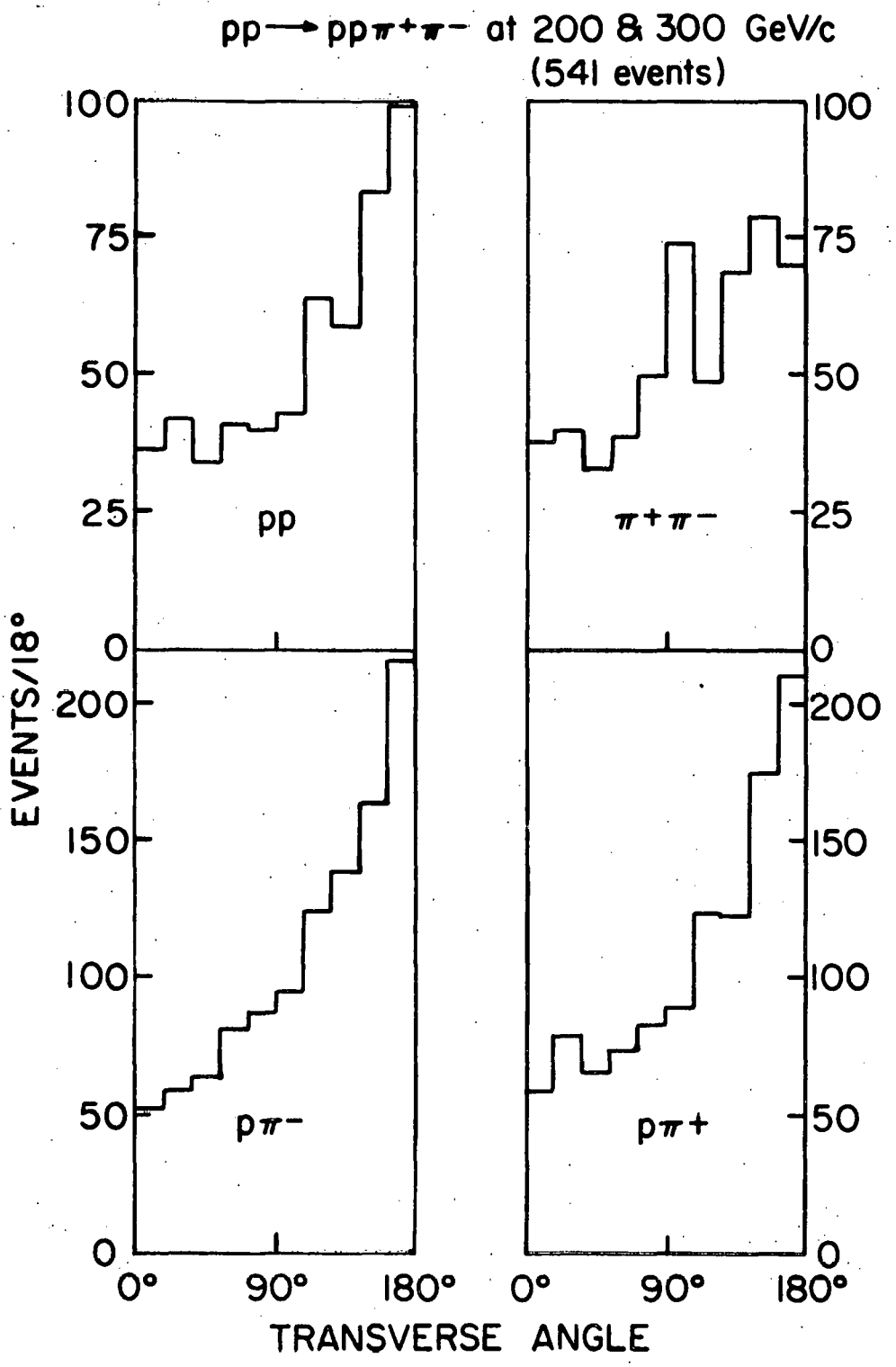

Figure 5.26. Exclusive azimuthal distributions for different particle combinations.

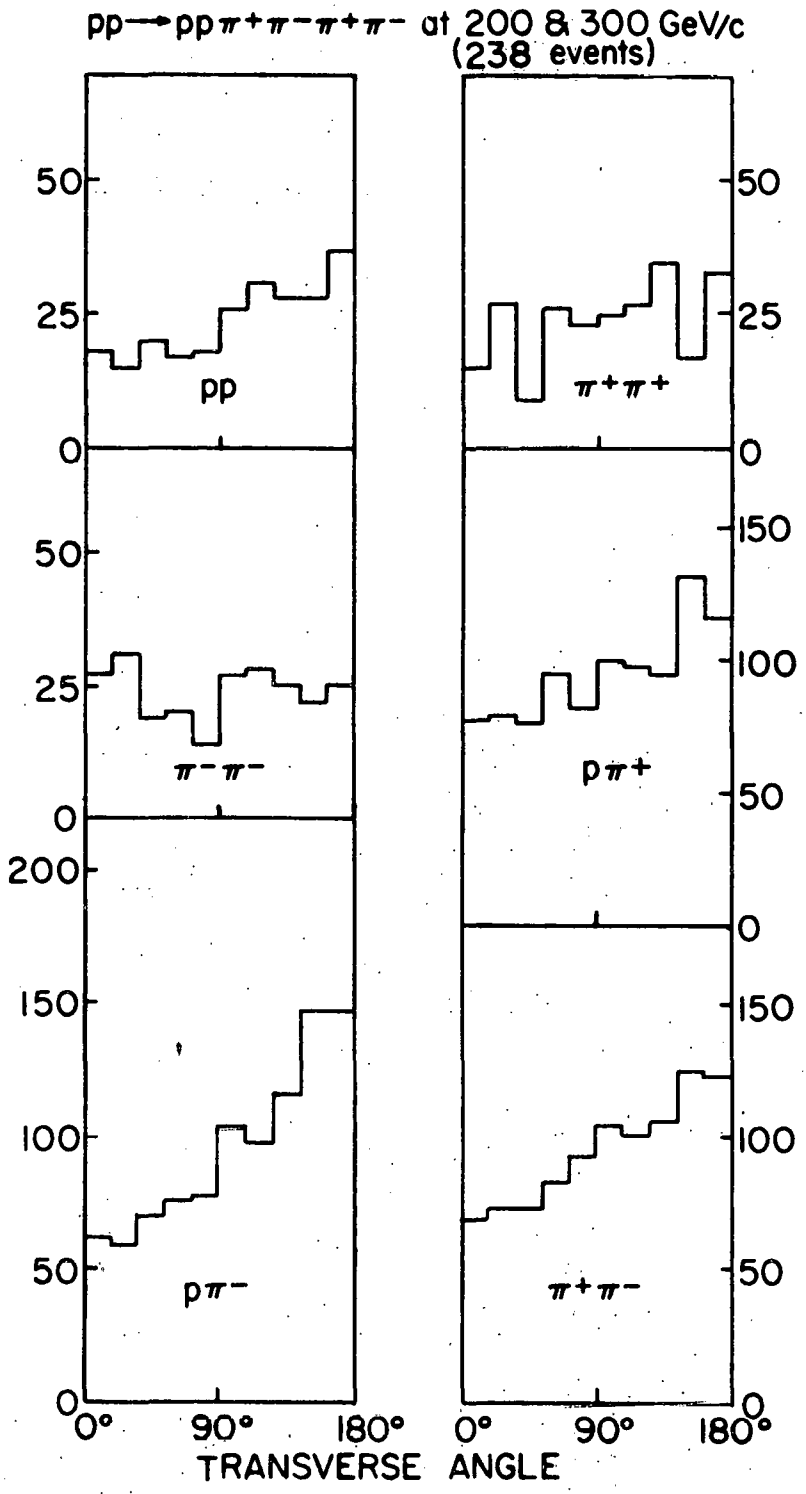

Figure 5.27. Exclusive azimuthal distributions for different particle combinations.

VI. SUMMARY AND CONCLUSION

The results of the present analysis are summarized as follows:

1. The cross sections for the $pp \to pp\pi^+\pi^-$ channel are 856 ± 77 μb at 200 GeV/c and 849 ± 111 μb at 300 GeV/c. For the $pp \to pp\pi^+\pi^-\pi^+\pi^-$ channel, the cross sections are 484 ± 69 μb at 200 GeV/c and 527 ± 100 μb at 300 GeV/c. These results are consistent with pomeron dominance for these reactions at Fermilab energies.

2. It is found that the majority of events in the final state $pp\pi^+\pi^-$ are associated with beam or target Diffractive Dissociation. The low mass system of $p\cdot\pi^+\cdot\pi^-$ predominantly decays via a Δ^{++} intermediate state. For this system, helicity conservation was studied. The results of this study were not conclusive, but it should be noted that they do not support the conclusions of the ANL group at 200 GeV/c. It is also found that the spin of the $p\pi^+\pi^-$ system is consistent with ½ for the "1450" MeV region but that higher spin states are required for higher mass regions.

3. Strong evidence of Double Excitation is seen in $pp\pi^+\pi^-\pi^+\pi^-$ final state at 200 and 300 GeV/c. Pomeron factorization is well satisfied in the mass region $M(p\cdot\pi^+\cdot\pi^-)_{\text{smallest}} < 2.5$ GeV.

4. Using the definition of Double Pomeron Exchange from the work of D. M. Chew and the largest number of events presently available in a pp experiment at Fermilab energies, 66 events in the $pp\pi^+\pi^-$ final state are identified as candidates for DPE events at 200 and 300 GeV/c. Of 24 DPE candidates with $M(\pi^+\pi^-) < 0.6$ GeV, 17 events have $M(p\cdot\pi^+\cdot\pi^-)_{smallest} < 3.0$ GeV. This indicates that the definition of DPE by D. M. Chew does not provide a clean separation of DPE events from Single Diffractive events. It was found that the distribution of azimuthal angle between protons is quite different between good DPE candidates and the Single Diffractive events.

5. The two particle exclusive azimuthal correlation measured in the present experiment agrees quite well with the prediction of the protostatistical model and is independent of energy between 200 and 300 GeV/c.

In conclusion, the success of various aspects of this experiment involving scanning, measuring, reconstruction and HOOKUP, background analysis of kinematic fitting and physics analysis strongly indicates that the BC-SC Hybrid System is an exceedingly useful device for studying the multiparticle exclusive reactions at Fermilab energies.

VII. BIBLIOGRAPHY

1. H. B. Crawley, W. J. Kernan and F. Ogino, "$\bar{p}p$ Elastic Scattering at 2.33 GeV/c," Phys. Rev. D8, 2781 (1973).

2. H. B. Crawley, N. W. Dean, E. S. Hafen, W. J. Kernan and F. Ogino, "Analysis of $\bar{p}p$ Elastic Scattering using two Coherent Exponentials," Phys. Rev. D9, 189 (1974).

3. F. Ogino, Study of Exclusive Channels in 200-300 GeV/c pp and 100 GeV/c π^-p Interactions. Presented at the American Physical Society meeting in Anaheim, January 29, 1975. American Physical Society Bull. 20, 13 (January 1975) (abstract).

4. W. Morris, B. Y. Oh, D. L. Parker, G. A. Smith, J. Whitmore, L. Voyvodic, R. Walker, R. Yaari, E. W. Anderson, H. B. Crawley, W. J. Kernan, F. Ogino, R. G. Glasser, D. G. Hill, G. McClellan, H. L. Price, B. Sechi-Zorn, G. A. Snow, F. Svrcek, W. D. Shephard, J. M. Bishop, N. N. Biswas, N. W. Cason, E. D. Fokitis and V. P. Kenney, "Study of the Energy and Charged Multiplicity Dependence of Inclusive π^- Production in π^-p Interactions up to Fermilab Energies," Phys. Lett. 56B, 395 (1975).

5. B. Y. OH, W. Morris, D. L. Parker, G. A. Smith, J. Whitmore, R. J. Miller, J. J. Phelan, P. F. Schultz, L. Voyvodic, R. Walker, R. Yaari, E. W. Anderson, H. B. Crawley, W. J. Kernan, F. Ogino, R. G. Glasser, D. G. Hill, G. McClellan, H. L. Price, B. Sechi-Zorn, G. A. Snow and F. Svrcek, "Two Particle Correlations in the Central Region of pp and π^-p Interactions at 100-300 GeV/c," Phys. Lett. 56B, 400 (1975).

6. French-USSR Collaboration, "Double Pomeron Exchange and Diffractive Dissociation in the reaction $pp \to pp\,\pi^+\pi^-$ at 69 GeV/c," preprint D Ph PE 75-04 M-17 (February 1975).

7. M. Derrick, B. Musgrave, P. Schreiner and H. Yuta, "The Reaction $pp \to pp\,\pi^+\pi^-$ at 205 GeV/c," Phys. Rev. 9, 1215 (1974).

8. G. A. Smith, "The NAL 30-inch Bubble Chamber-Wide Gap Spark Chamber Hybrid System," presented at the Berkeley meeting of the Division of Particles and Fields of the American Physical Society, August 1973. American Institute of Physics Conference Proceedings, No. 14, Particles and Fields Subseries No. 6, 500 (1973).

9. W. J. Higby and A. H. Klein, "Ames Laboratory On-line Control System for Bubble Chamber Film Measuring," United States Atomic Energy Commission Report IS-2228 (Iowa State University, Ames, Iowa)(1969); T. L. Schalk and W. J. Kernan, "Physics Use of the Ames Laboratory On-line Measuring System for Bubble Chamber Events," United States Atomic Energy Commission Report IS-2231 (Iowa State University, Ames Iowa) (1969).

10. F. T. Solmitz, A. D. Johnson and T. B. Day, "Three View Geometry Program," Alvarez Group Programming Note, p-117 (1965).

11. D. Negra and J. T. Carroll, "SLAC BC Note No. 16," (1972).

12. J. M. Bishop and W. D. Shephard, "Momentum Resolution in the E2B Hybrid System," ND HEP 75-76 (August 1975).

13. O. I. Dahl, T. B. Day, F. T. Solmitz and N. L. Gould, "SQUAW, Kinematic Fitting Program," Group A Programming Note No. p-126 (1968).

14. R. J. Sprafka, High Energy Physics Programming, Note No. p-11 (MSU) (1968).

15. J. Whitmore, "Experimental Results on Strong Interactions in the NAL Hydrogen Bubble Chamber," Phys. Rep. 10C, 273 (1974).

16. D. R. O. Morrison, "Interpretation of the variation of cross section with incident momentum for inelastic two body reactions," Phys. Lett. 22, 528 (1966).

17. D. Horn and F. Zachariasen, Hadron Physics at Very High Energy, (W. A. Benjamin Inc., New York, 1973), Chapter 17, p. 271.

18. F. T. Dao, D. Gordon, J. Lach, E. Malamad, T. Meyer, R. Poster, P. E. Schlein and W. E. Slater, "pp Interactions at 303 GeV/c; Inclusive Measurement of Δ^{++} (1236) Resonance Production," Phys. Rev. Lett. 30, 37 (1973).

19. J. P. DeBrion, C. Bromberg, T. Ferbel, T. Jensen, R. Schindler, P. Slattery, A. A. Seidl and J. C. Vander Velde, "Production of $\Delta(1236)$ in pp collisions at High Energy," Phys. Rev. Lett. 34, 910 (1975).

20. D. Brick, B. Haber, M. Hodous, R. Halsizer, V. Kistiakowsky, A. Levy, A. Nakkasyan, I. Pless, V. Simak, P. Trepagnier, J. Wolfson and R. Yamamoto, "Comparison of Inclusive Production of $\Delta^{++}(1236)$ at 15 and 303 GeV/c," Phys. Rev. Lett. 31, 488 (1973).

21. David W. G. S. Leith, "Diffractive Dissociation," Proceedings of the XVI International Conference on High Energy Physics (Chicago-Batavia), Vol. 3, p. 321 (1972).

22. J. I. Rhode, R. A. Leacock, W. J. Kernan, R. A. Jesperson and T. L. Schalk, "Spin Analysis of $p\pi^+\pi^-$ Enhancements in the $pp\pi^+\pi^-$ Final State Produced in pp Interactions at 22 GeV/c," Phys. Rev. 187, 1844 (1969).

23. J. G. Rushbrooke, J. R. Williams, N. C. Barford, M. J. Losty and K. Pongpoonsuksri, "Study of $p\pi^+\pi^-$ isobars produced in the $pp\pi^+\pi^-$ final state by pp interactions at 16 GeV/c," Phys. Rev. 4, 3273 (1971).

24. A. Firestone, V. Davidson, F. Nagy, C. Peck, A. Sheng, F. T. Dao, R. Hanft, J. Lach, E. Malamud, F. Nezrick, A. Dzierba, R. Poster and W. Slater, "Evidence for double diffraction in pp interactions at 300 GeV/c," Phys. Rev. 12, 15 (1975).

25. R. Webb, G. Trilling, V. Tegeldi, P. Strolin, A. Staude, B. Shen, P. Schlein, J. Rander, B. Naroska, F. Muller, T. Meyer, W. Marsh, W. Lockman, J. Layter, A. Kernan, H. Foeth, R. Ellis, A. Bohm, L. Baksay, "Double diffraction dissociation and test of Pomeron factorization at the CERN ISR," Phys. Lett. 55B, 336 (1975).

26. M. Derrick, B. Musgrave, P. Schreiner and H. Yuta, "Double-Pomeron-Exchange Contribution to the Reaction $pp \to pp\pi^+\pi^-$ at 205 GeV/c," Phys. Rev. Lett. 32, 80 (1974).

27. D. M. Chew, "Search for Experimental Evidence on Exclusive Double-Pomeron Exchange," Nuclear Physics B82, 422 (1974).

28. J. Finkelstein and J. Kajantie, "Multiple Pomeranchuk Exchange Violates Unitarity," Phys. Lett. 26B, 305 (1968).

29. M. C. Foster, D. Z. Freedman, S. Nussinov, J. Hanlon and R. S. Panvini, "Azimuthal Correlations of High-Energy Collision Products," Phys. Rev. D6, 3135 (1972).

30. M. Pratap, R. Engelmann, T. Kafka, Y. Cho, T. H. Fields, L. G. Hyman, R. Singer, L. Voyvodic, R. Walker and J. Whitmore, "Azimuthal Correlations in pp Interactions at 205 GeV/c," Phys. Rev. Lett. 33, 797 (1974).

31. F. James, CERN Computer Program Library, W505 (long write-up) (1970); and E. Byckling and K. Kajantie, Particle Kinematics, (John Wiley & Sons, New York, 1973).

VIII. ACKNOWLEDGEMENTS

As this dissertation concludes my formal education for over 21 years, I would like to take this opportunity to express my sincere gratitude to those people who contributed to it. Professor W. J. Kernan has provided the author with the excellent educational opportunities including early analysis of $\bar{p}p$ reaction and the participation of all phases of the experiment at the Fermilab. His generous guidance and considerable advice will certainly not be forgotten. I would like to thank Professor H. B. Crawley for his extensive assistance during the entire period of my graduate studies. I also thank both Professor Kernan and Professor Crawley for many helpful criticisms and suggestions during the writing of this dissertation.

There are many people in Ames Laboratory of ERDA who have also contributed to my graduate career. Mr. W. J. Higby, Mr. A. H. Klein and Mr. C. B. Fullhart deserve credit for their work on the on-line measuring system. Appreciation is expressed to Mrs. B. Pepper, Mrs. D. Edwards, Mrs. M. Frisk, Mrs. J. P. Lincoln and the scanning-measuring staff for their efforts and help with the film scanning and measuring.

I would like to thank all of my coauthors in Experiment 2B collaboration for their contribution in the various aspects of my dissertation research; in particular, my gratitude is extended to: Dr. E. W. Anderson and Dr. D. L. Parker at Iowa

State University; Dr. W. Morris, Dr. B. Y. Oh, Professor G. A. Smith and Dr. J. Whitmore at Michigan State University; Dr. L. Voyvodic and Dr. R. Walker of Fermi National Accelerator Laboratory; Dr. R. J. Miller, Dr. J. J. Phelan and Dr. P. F. Schultz of Argonne National Laboratory. Thanks go also to Professor A. Firestone of Iowa State University for invaluable discussions in regard to the Double Excitation. I have enjoyed useful discussions with Professors N. W. Dean, K. E. Lassila and Bing-lin Young. My appreciation is also extended to Professor W. L. Talbert for carefully reading this manuscript. I would like to express my deep gratitude to Professor Toshiyuki Toyoda for his constant encouragement during all stages of my undergraduate and graduate career. I gratefully acknowledge for the financial support during my graduate studies: to Iowa State University for support during 1971-1972, to the United States Atomic Energy Commission for support during 1972-1974, and to Professor D. J. Zaffarano and Iowa State Graduate College for Dissertation Research Fellowship during 1974-75.

I should like to thank Mrs. Bonnie Harriott for her efforts in typing and preparing this dissertation.

Finally, I thank my parents for their continual support and encouragement.

IX. APPENDIX A: HOOKUP OUTPUT FORMAT

The output format of the ISU version of HOOKUP is almost the same as that of TVGP or SQUAW. The 7th word of BLOCK1 contains the length of BLOCK5, which in turn contains all BC-SC matching records, regardless of whether they are good or bad. The 30th word of BLOCK2 tells whether the SC information was actually used for this event. BLOCK3 is the same as the input TVGP records. If we do have a good BC-SC matching record for a track, this replaces the corresponding track record in BLOCK4 of TVGP. When there are two mass interpretations (proton and positive pion in the present experiment) and the matching attempt for the second interpretation is successful, both interpretations are replaced by the HOOKUP record. If no SC data exists or the matching attempt fails, the raw TVGP records are used. The subroutine EDIT has options to do the following:

a. Substitute data corresponding to the averaged beam curvature and angles into the beam track data position.

b. Check the curvature and the associated error of HOOKUP tracks.

   If the ratio $\Delta p/p$ is greater than 0.5, the HOOKUP track is not substituted into the TVGP record.

X. APPENDIX B: Z VARIABLE AND RAPIDITY

The details of variable definitions are described in Reference 27. For the process $AB \to A\pi^+\pi^-B$, two Z variables can be defined:

$$Z_A \equiv \ell n \frac{S}{M^2_{A\pi^+\pi^-}} \simeq \ell n \frac{1}{1-X_A} \tag{10-1}$$

and

$$Z_B \equiv \ell n \frac{S}{M^2_{B\pi^+\pi^-}} \simeq \ell n \frac{1}{1-X_B} \tag{10-2}$$

where A and B are protons in the present experiment and X is the Feynman variable. The Double Pomeron Exchange (DPE) candidates are those which have:

$$e^{-Z_A} \lesssim 0.1 \quad \text{and} \quad e^{-Z_B} \lesssim 0.1$$

or

$$Z_A \gtrsim 2.3 \quad \text{and} \quad Z_B \gtrsim 2.3 \; . \tag{10-3}$$

The rapidity gaps between particles are related to Z variables as follows:

$$y_{AB} \simeq \ell n \frac{S}{<M_{\perp A}><M_{\perp B}>} \; ,$$

$$y_{A(\pi^+\cdot\pi^-)} \simeq Z_A + \ell n \frac{\langle M_{\perp\pi} \rangle}{\langle M_{\perp A} \rangle} ,$$

$$y_{B}(\pi^+\cdot\pi^-) \simeq Z_B + \ell n \frac{\langle M_{\perp\pi} \rangle}{\langle M_{\perp B} \rangle}$$

and

$$y_{\pi^+\pi^-} = y_{AB} - y_{A(\pi^+\cdot\pi^-)} - y_{B(\pi^+\cdot\pi^-)} .$$

where

$$M^2_{\perp} = M^2 + P_{\perp}^2 .$$

Figure 10.1 shows the rapidity distributions of π^+ and π^- in the final state $pp\,\pi^+\pi^-$ at 200 and 300 GeV/c, in which DPE candidates are shaded. Figure 10.2 is the rapidity distribution of protons. Figure 10.3 shows the scatter plot of $y(\pi^+)$ with respect to $y(\pi^-)$.

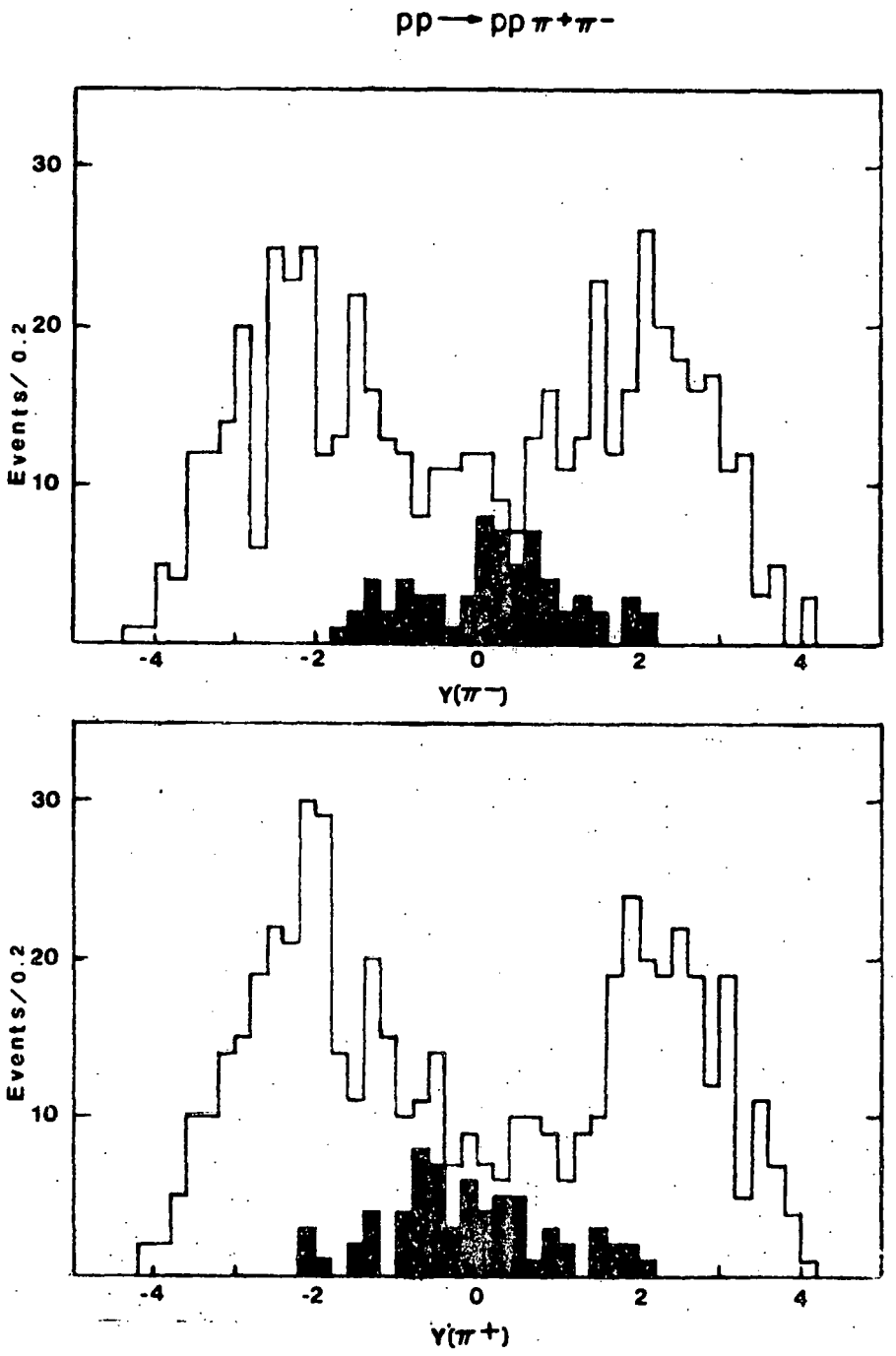

Figure 10.1. The rapidity distributions for the π^+ and π^- in the reaction $pp \rightarrow pp\,\pi^+\pi^-$ at 200 and 300 GeV/c. The DPE candidates are shaded.

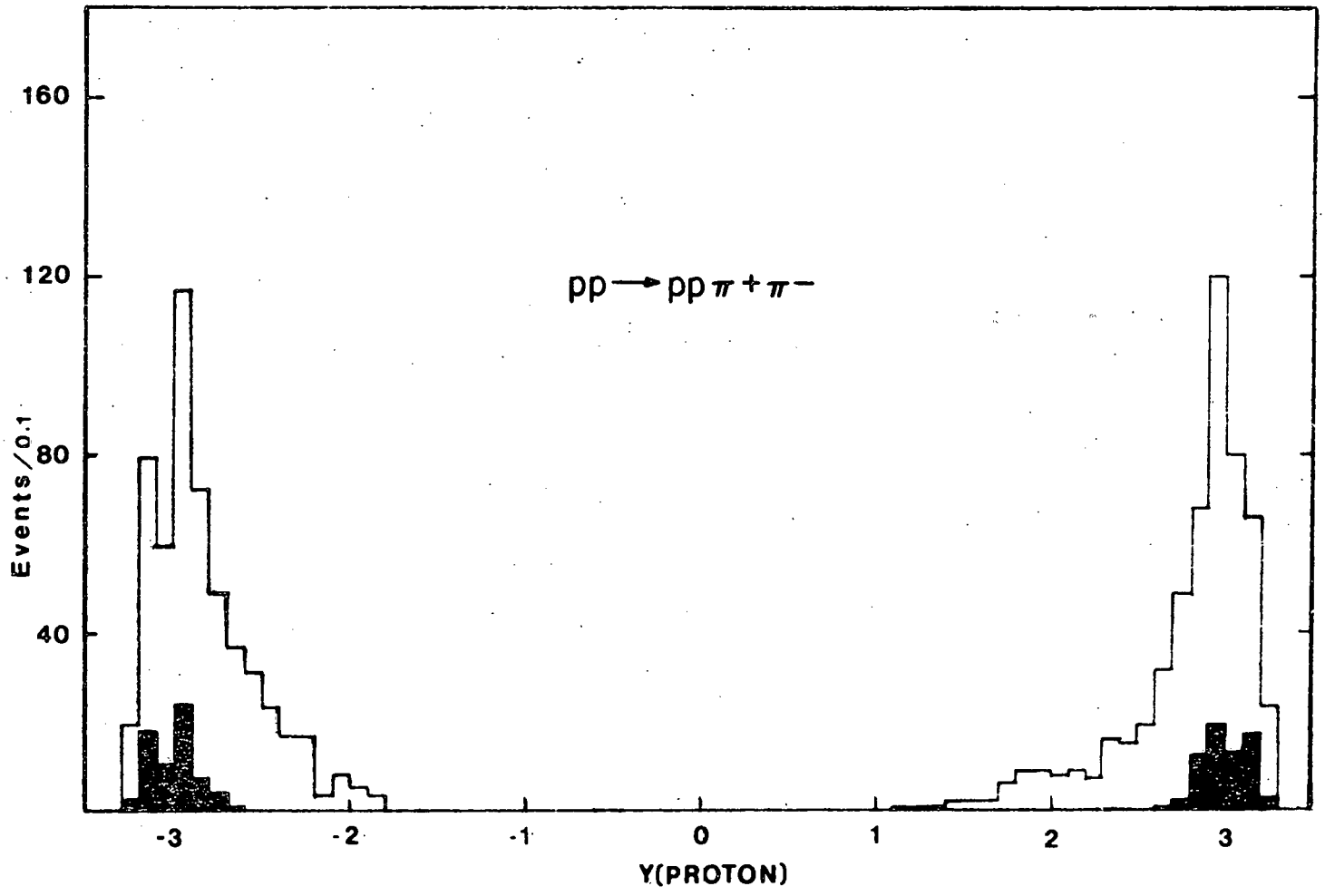

Figure 10.2. The rapidity distribution for the proton in the reaction $pp \to pp\pi^+\pi^-$ at 200 and 300 GeV/c. The DPE candidates are shaded.

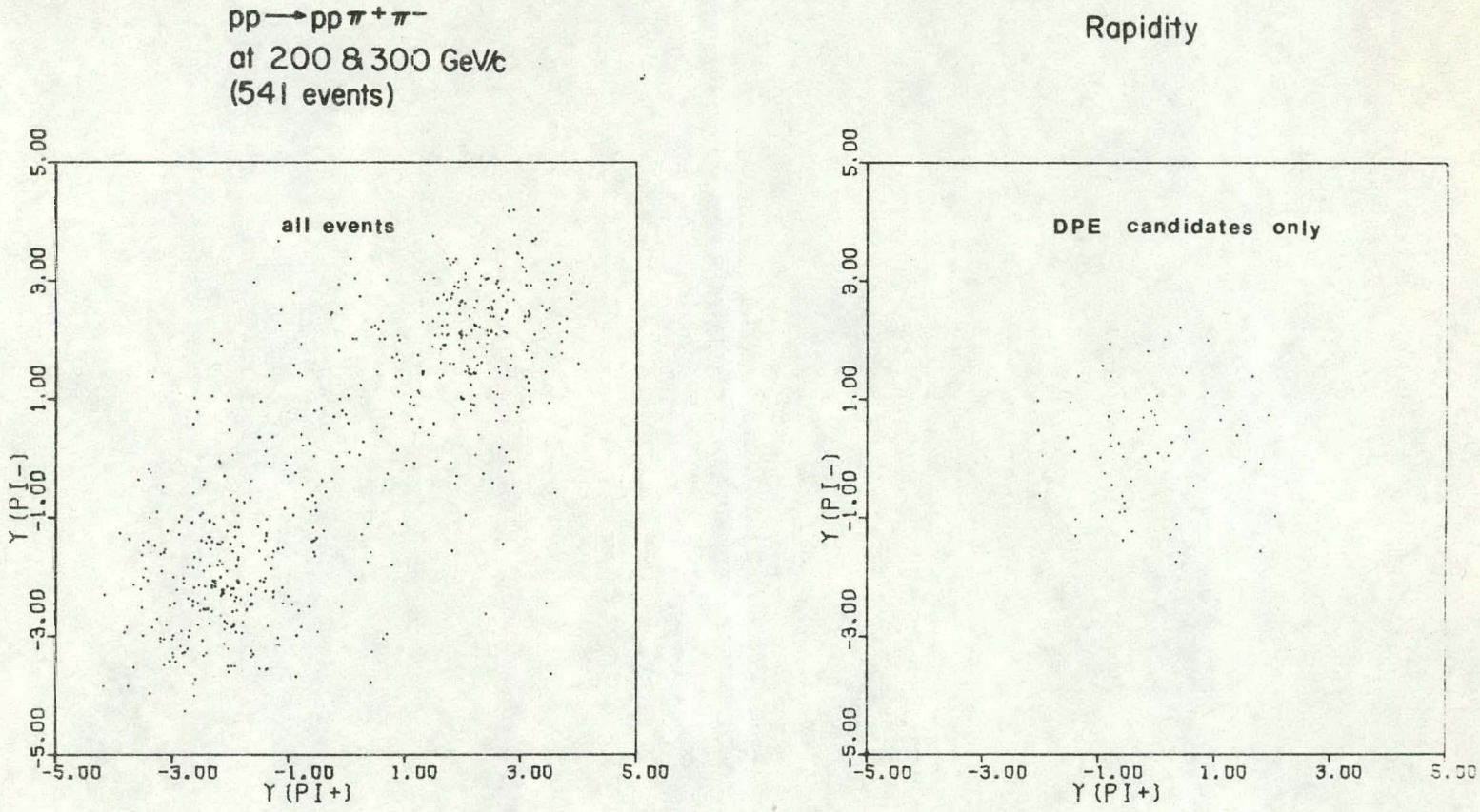

Figure 10.3. Scatter plot of the rapidity of π^+ with respect to the rapidity of π^- for the reaction $pp \rightarrow pp\,\pi^+\pi^-$ at 200 and 300 GeV/c.